

2022-12-01

Molecularly inspired organic macrocycles catalyzed water splitting reaction for sustainable fuel production

Yulu Ge
University of Texas at El Paso

Follow this and additional works at: https://scholarworks.utep.edu/open_etd

 Part of the [Chemistry Commons](#)

Recommended Citation

Ge, Yulu, "Molecularly inspired organic macrocycles catalyzed water splitting reaction for sustainable fuel production" (2022). *Open Access Theses & Dissertations*. 3678.
https://scholarworks.utep.edu/open_etd/3678

This is brought to you for free and open access by ScholarWorks@UTEP. It has been accepted for inclusion in Open Access Theses & Dissertations by an authorized administrator of ScholarWorks@UTEP. For more information, please contact lweber@utep.edu.

MOLECULARLY INSPIRED ORGANIC MACROCYCLES CATALYZED WATER
SPLITTING REACTION FOR SUSTAINABLE FUEL PRODUCTION

YULU GE

Doctoral Program in Chemistry

APPROVED:

Dino Villagrán, Ph.D., Chair

Skye Fortier, Ph.D.

Sreeprasad T Sreenivasan, Ph.D.

Srinivasa Rao Singamaneni, Ph.D.

Stephen L. Crites, Jr., Ph.D.
Dean of the Graduate School

Copyright ©

by

Yulu Ge

2022

Dedication

With all my love to: Lu Ling, Ge Ming and Anthony J. Denning.

MOLECULARLY INSPIRED ORGANIC MACROCYCLES CATALYZED WATER
SPLITTING REACTION FOR SUSTAINABLE FUEL PRODUCTION

by

YULU GE, M.S.

DISSERTATION

Presented to the Faculty of the Graduate School of

The University of Texas at El Paso

in Partial Fulfillment

of the Requirements

for the Degree of

DOCTOR OF PHILOSOPHY

THE DEPARTMENT OF CHEMISTRY AND BIOCHEMISTRY

THE UNIVERSITY OF TEXAS AT EL PASO

December 2022

Acknowledgements

I would like to give my sincere gratitude to my supervisor, Dr. Dino Villagrán, for all the knowledge I have learned from him throughout my PhD study at the University of Texas at El Paso. He helped me greatly to develop my skills in the research of different chemistry concepts, to improve my understanding of the fields of electrochemistry and catalysis, and to gain a deep appreciation for the perseverance required to perform such research. The joy and enthusiasm he has for his research will be contagious and motivational for my entire life. I would especially express my gratefulness to my committee members, Drs. Skye Fortier, Sreeprasad T Sreenivasan, and Srinivasa Rao Singamaneni, for their support and assistance throughout my entire PhD study. I appreciate their support, encouragement, and kind supervision in the completion of my projects. I would also like to thank all of my lab mates, Dr. Yanyu Wu, Dr. Karen Ventura, Dr. Nancy Rodriguez, Dr. Mariana Marcos, Sheng Yin, Neidy Ocuane, Jonathan Calvillo and Alexandra Castillo, for helping me through my six years here at the University of Texas at El Paso. I am very glad that I also had the opportunities to work with many outstanding undergraduate researchers in the Dr. Villagrán's lab, Isabel Barraza, Roy Arrieta, Juan Francisco, and Sandra Villalobos. Last, but not the least, I thank the Department of Chemistry and Biochemistry at the University of Texas at El Paso for offering me the opportunity to pursue my PhD degree, which is a big milestone in my career development. I will strive to use gained skills and knowledge in the best possible way and continue to work on their improvement.

Abstract

Hydrogen fuel generation through electrochemical water splitting is considered as an advanced energy conversion technology driven by sustainable energy. High activity and cost effective electrocatalysts that are able to drive down the energy cost needed for both two half reactions, namely, hydrogen evolution reaction (HER) and oxygen evolution reaction (OER) are required to fulfill the energy transfer process. Exploring new electrocatalysts with enhanced OER and HER activity and stability is crucial for renewable energy applications. Porphyrin and macrocycle derivatives are versatile and can electrochemically catalyze water splitting efficiently. In our work, we use porphyrin as platform for both HER and OER catalysis. As a homogeneous electrocatalyst, free base porphyrins are able to afford up to two electrons redox transfer. In addition, the four-nitrogen cavity inside the porphyrin provides two protonation sites, this makes it feasible for facilitating HER. Rational design: the substituent group with -Br, -F, F₂ and F₃ on the meso-position results in regulatable hydrogen production under different mechanisms. We also developed a heterogenized porphyrin framework with Kevlar structure, which results in efficient and sturdy bifunctional electrocatalysis that can operate in both neutral and pH dependent solutions are comparable with most of the metal-based materials. The catalytic activity can hold for 60 hours under all the electrolysis conditions. We found that when porphyrins are metalated with first-row transition metals, i.e., Co and Fe, with linkers that have different electron negativity, they show different performance towards OER. On the other hand, intercalated porphyrin into electrochemically inert layered structure material can prevent catalyst degradation and serve for water oxidation. Beside these, we were also working on high surface area Ni based MoS₂ that is synthesized with pre-treated amine and carbon for water splitting electrocatalysis. As for catalyzing HER, pre-treatment with carbon nanotubes during the synthesis can largely enhance the exposure of MoS₂ HER active basal plane; when using as OER catalyst, the DETA pre-treated NiMoS₂ has the best performance. All these works provide insight into the rational electrocatalyst design for eco-friendly fuel generation and more importantly, for the practical large-scale industrial production in an environmentally benign and cost-effective way.

Table of Contents

Dedication.....	iii
Acknowledgements.....	v
Abstract.....	vi
Table of Contents.....	vii
List of Tables.....	x
List of Figures.....	xi
Chapter 1.....	1
Introduction.....	1
Chapter 2.....	3
Regulatable Molecular porphyrins catalyzed hydrogen evolution reaction.....	3
2.1 Introduction.....	3
2.2 Materials and Methods.....	5
2.3 Syntheses.....	6
2.3.1 Synthesis of 5,10,15,20-tekis(4-bromophenyl) porphyrin (1).....	6
2.3.2 Synthesis of 5,10,15,20-tekis(4-fluorophenyl) porphyrin (2).....	6
2.3.3 Synthesis of 5,10,15,20-tekis(2,4,6-trifluorophenyl) porphyrin (3).....	7
2.3.4 Synthesis of 5,10,15,20-tekis(2,6-difluorophenyl) porphyrin (4).....	8
2.4 Results and discussion.....	9
2.4.1 Cyclic voltammetry.....	9
2.4.2 Bulk electrolysis.....	10
2.4.4 Spectroelectrochemistry analysis.....	12
2.4.5 Proposed mechanism.....	13
2.5 Conclusion.....	15
2.6 ¹ H NMR data.....	16
Chapter 3.....	20
Free-base porphyrin polymer for bifunctional electrochemical water splitting.....	20
3.1 Introduction.....	20

3.2 Materials and Methods.....	21
3.3 Syntheses.....	23
3.3.1 Synthesis of 5,10,15,20-tetrakis(4-aminophenyl) porphyrin (H ₂ TAPP)	23
3.3.2 Synthesis of Zinc(II) 5,10,15,20-tetrakis-(4-aminophenyl) porphyrin Zinc(II) (ZnTAPP).....	24
3.3.3 Synthesis of Porphvlar	24
3.3.4 Synthesis of Zn-Porphvlar	25
3.4 Characterizations.....	26
3.5 Results and discussion	29
3.6 Conclusions.....	36
Chapter 4.....	38
Metalloporphyrin organic polymers as effective and stable electrocatalysts for oxygen evolution reaction and oxygen reduction reaction	38
4.1 Introduction.....	38
4.2 Materials and Methods.....	40
4.3 Characterizations.....	41
4.4 Syntheses.....	44
4.4.1 Synthesis of porphyrin organic polymer [(Por)OP and F(Por)P]:	44
4.4.2 Synthesis of cobalt porphyrin organic polymer [(Co(Por)OP) and CoF(Por)OP] and iron porphyrin organic polymer [(Fe(Por)OP) and FeF(Por)OP]:.....	45
4.5 Results and discussion	46
4.6 Conclusions.....	48
Chapter 5.....	50
Amine and Carbon-pretreated nickele molybdenum disulfide as bifunctional electrocatalysts for hydrogen and oxygen gas evolution.....	50
5.1 Introduction.....	50
5.2 Materials and Methods.....	51
5.2.1 Materials	51
5.2.2 Physical measurements	52
5.2.3 Electrochemical methods.....	52
5.2.4 Preparation of NiMoS ₂ modified carbon paper electrode.....	52
5.3 Syntheses.....	53

5.3.1 Synthesis of NiMoS ₂ using alkyl-containing thiomolybdate precursors (1-3) ...	53
5.3.2 Synthesis of NiMoS ₂ using ammonium tetrathiomolybdate (ATM) precursors (4).....	53
5.3.3 Synthesis of carbon nanotubes.....	53
5.4 Characterizations.....	54
5.5 Results and discussion	58
5.6 Conclusions.....	68
Chapter 6 Conclusion and Future Work	69
References.....	71
Vita	82

List of Tables

TABLE 1. Parameters for Equivalent Circuits for the water splitting reaction for Porphvlar.	34
TABLE 2. Electrochemical impedance parameters obtained from fitting Nyquist plot data with the equivalent circuit for HER for NiMoS ₂	60
TABLE 3. Electrochemical impedance parameters obtained from fitting Nyquist plot data with the equivalent circuit for OER for NiMoS ₂	64

List of Figures

Scheme 1. Schematic description of energy diagram for water splitting.	2
Scheme 2. The as-synthesized porphyrin electrocatalysts.	5
Figure 1. Cyclic Voltammetry of H ₂ TBrPP, 1 (a) and H ₂ TFPP, 2 (b) in solutions containing 0.1 M TBAPF ₆ and in presence of acid.	9
Figure 2. Cyclic Voltammetry of H ₂ TF ₃ PP, 3 (a) and H ₂ TF ₂ PP, 4 (b) in solutions containing 0.1 M TBAPF ₆ and in presence of acid.	10
Figure 3. Charge passed plot versus time of as-synthesized porphyrin 1 (red) and 2 (blue) compared with the reported perfluorophenyl porphyrin (green) and the blank THF (grey) under bulk electrolysis condition in the presence of acid.	11
Figure 4. The UV-vis spectrum of 1 under one-electron reduction potential (a) and two-electron reduction potential (b) in the absence of acid.	12
Figure 5. The UV-vis spectrum of 3 under one-electron reduction potential (a) and two-electron reduction potential (b) in the absence of acid.	13
Scheme 3. Proposed mechanistic reaction pathway for 1 and 2 catalyzed hydrogen evolution reaction.	14
Scheme 4. Proposed mechanistic reaction pathway for 3 and 4 catalyzed hydrogen evolution reaction.	15
Figure 7. ¹ H NMR spectrum of 4-bromophenyl porphyrin(1).....	16
Figure 8. ¹ H NMR spectrum of 4-flouorophenyl porphyrin(2)	17
Figure 9. ¹ H NMR spectrum of 2,4,6-flouorophenyl porphyrin(3)	18
Figure 10. ¹ H NMR spectrum of 2,6-flouorophenyl porphyrin(4)	19
Scheme 5. Synthesis procedure of H ₂ TAPP.	23
Scheme 6. Synthesis procedure of ZnTAPP.	24
Scheme 7. Synthesis procedure of Porphvlar	25
Figure 11. Scanning electron microscopy (SEM) of Porphvlar in various scales and the <i>p</i> -XRD peaks.	25
Figure 12. Energy-dispersive X-ray spectroscopy (EDX) mapping of Porphvlar.	26
Figure 13. High resolution XPS spectra of Porphvlar sample (A-C); (D). Atomic ration of C, N, and O of the Porphvlar sample; (E) Full XPS survey.	27

Figure 14. Spectroscopic characterization of Porphvlar. (A) FT-IR spectra of Porphvlar and molecular porphyrin (H₂TAPP). (B) Comparison UV-vis spectra of Porphvlar and H₂TAPP. ... 28

Figure 15. Polarization curves of molecular porphyrin (H₂TAPP) (blue), Porphvlar (red) and blank carbon paper electrode under different conditions. (A) Oxidation in 1.0 M KOH aqueous solution; (B) Reduction in 0.5 M H₂SO₄ aqueous solution, (C) Oxidation in 1.0 M PBS buffer solution; (D) Reduction in 1.0 M PBS buffer solution. 29

Figure 16. Comparison linear sweep voltammetry of Zn-Porphvlar with the metal-free Porphvlar in different electrolytes under the corresponding oxidation and reductions. Scan rate: 5 mV/s. . 31

Figure 17. Electrochemical impedance spectroscopy of Porphvlar (red) and H₂TAPP (purple) operated at 250 mV overpotential..... 32

Figure 18. Electrochemical impedance spectroscopy (EIS) of hydrogen evolution reaction catalyzed by Porphvlar on carbon paper electrode: (A) Nyquist plot of HER in 0.5 M H₂SO₄ aqueous solution with simulation fit. (B) Bode plot of HER in 0.5 M H₂SO₄ aqueous solution. (C) The electrical equivalent circuit (EEC) used to simulate the impedance spectra fit in 0.5 M H₂SO₄ aqueous solution. (D) Nyquist plot of HER in 1.0 M PBS solution with simulation fit. (E) Bode plot of HER in 1.0 M PBS solution. (F) The electrical equivalent circuit (EEC) used to simulate the impedance spectra fit in 1.0 M PBS solution. 33

Figure 19. Electrochemical impedance spectroscopy (EIS) of oxygen evolution reaction catalyzed by Porphvlar on carbon paper electrode: (A) Nyquist plot of OER in 1.0 M KOH aqueous solution with simulation fit. (B) Bode plot of OER in 1.0 M KOH aqueous solution. (C) The electrical equivalent circuit (EEC) used to simulate the impedance spectra fit in 1.0 M KOH aqueous solution. (D) Nyquist plot of OER in 1.0 M PBS solution with simulation fit. (E) Bode plot of OER in 1.0 M PBS solution. (F) The electrical equivalent circuit (EEC) used to simulate the impedance spectra fit in 1.0 M PBS solution..... 34

Figure 20. Time dependence of the current density for as-synthesized Porphvlar at static potential; blue: HER in 0.5 M H₂SO₄; green: in 1.0 M PBS buffer; teal: OER in 1.0 M PBS buffer; red: OER in 1.0 M KOH. 36

Figure 21. FT-IR spectra of (Por)OP, F(Por)OP, Co(Por)OP, CoF(Por)OP, Fe(Por)OP and FeF(Por)OP..... 41

Figure 22. *p*-XRD of (Por)OP, F(Por)OP, Co(Por)OP, CoF(Por)OP, Fe(Por)OP and FeF(Por)OP. 42

Figure 23. SEM images of (a) (Por)OP, (b) Co(Por)OP, (c) Fe(Por)OP, (d) F(Por)OP, (e) CoF(Por)OP and (f) FeF(Por)OP.....	42
Figure 24. representative XPS survey (CoPorOP and FePorOP).	43
Figure 25. representative EDX spectrum of synthesized porphyrin organic polymers: CoPorOP and FePorOP	43
Figure 26. representative elemental mapping spectrum of synthesized porphyrin organic polymers (CoPorOP).....	44
Figure 27. representative UV-vis spectra of synthesized porphyrin organic polymers (CoPorOP and FePorOP).....	45
Scheme 8. Synthetic scheme of porphyrin organic polymers.(R = H or F).....	44
Scheme 9. Synthetic scheme of metalloporphyrin organic polymers. (R = H or F, M = Co or Fe)	45
Figure 28. Cyclic Voltammograms of (Por)OP, F(Por)OP, Co(Por)OP, CoF(Por)OP, Fe(Por)OP,FeF(Por)OP and carbon black with iR compensation in the presence of 0.1 M KOH electrolyte solutions saturated with oxygen gas.....	46
Figure 29. Electrochemical impedance spectroscopy and the corresponding equivalent electric circuits.....	47
Figure 30. Chronoamperometry of the synthesized porphyrin organic polymers with current maintained at 10 mA/cm ² for 14 hours.	48
Figure 31. <i>p</i> -XRD patterns of 1-4.	55
Figure 32. SEM images showing the morphologies of (a-b) sample 4 and (c-d) representative pre-treated NiMoS ₂ (sample 2) at two different scales.	55
Figure 33. Representative elemental mapping images (NiMoS ₂ -CNT).	56
Figure 34. EDX spectra of samples 1-4.	57
Figure 35. (a) HER Polarization curves in a cathodic potential window for the as-synthesized catalysts: (1) NiMoS ₂ -CNT (purple); (2) NiMoS ₂ -DETA (green); (3) NiMoS ₂ -EDA (blue); (4) NiMoS ₂ -Pristine (red) and Pt (black) and blank carbon paper doped with carbon black (grey) in 0.5 M H ₂ SO ₄ aqueous solution. Scan rate: 5 mV/s; (b) Tafel plots of 1-4 derived from the HER polarization curves. (c) Nyquist plots of 1-4 in acidic condition. (d) Chronoamperometric studies of the as-synthesized NiMoS ₂ (1-4) in 0.5 M H ₂ SO ₄ at $\eta = 0.250$ V.	58

Figure 36. (a) and (b): Bode plot of HER using 1 and 2 as electrocatalysts under 250 mV overpotential with 5 mV AC voltage applied; (c) the simulated equivalent electric circuit of the corresponding electrochemical processes.	59
Figure 37. (a) and (b): Bode plot of HER using 3 and 4 as electrocatalysts under 250 mV overpotential with 5 mV AC voltage applied; (c) the simulated equivalent electric circuit of the corresponding electrochemical processes.	60
Figure 38. (a) Polarization curves of 1-4 and carbon black as control electrode in 1.0 M KOH as electrolyte. Scan rate: 5 mV/s. (b) Tafel plots of the corresponding NiMoS ₂ electrocatalysts (1-4) derived from the OER polarization curves. (c) Nyquist plots of 1-4 at an overpotential of 250 mV in 1.0 M KOH aqueous solution. (d) Chronoamperometric studies of 1-4 in 1.0 M KOH at $\eta = 0.250$ V.....	61
Figure 40. (a) and (b): Bode plot of OER using 1 and 3 as electrocatalysts under 250 mV overpotential with 5 mV AC voltage applied; (c) the simulated equivalent electric circuit of the corresponding electrochemical processes.	63
Figure 39. (a) and (b): Bode plot of OER using 2 and 4 as electrocatalysts under 250 mV overpotential with 5 mV AC voltage applied; (c) the simulated equivalent electric circuit of the corresponding electrochemical processes.	63
Figure 41. Linear fit plots of scan rates as a function of double layer charging current for the NiMoS ₂ (1-4) report in this study. (a) Performed in 0.5 M H ₂ SO ₄ aqueous solution; (b) Performed in 1.0 M KOH aqueous solution. Scan rate: 0.02 v/s, 0.04 v/s, 0.06 v/s, 0.08 v/s, 0.1 v/s, 0.12 v/s, 0.14 v/s, 0.16 v/s.....	65
Figure 42. Cyclic voltammograms of NiMoS ₂ catalysts 1-4 at different scan rates in the 0.1 V potential window with no faradaic process in 0.5 M H ₂ SO ₄ solution.	66
Figure 43. Cyclic voltammograms of NiMoS ₂ catalysts 1-4 at different scan rates in the 0.1 V potential window with no faradaic process in 1.0 M KOH solution.	67

Chapter 1

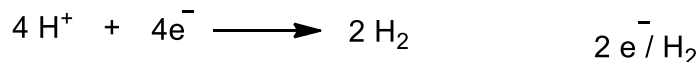
Introduction

With the rapid depletion of fossil fuels and the associated environmental issues due to their combustion, the development of alternative energy source is crucial and emergent.¹ Hydrogen is an ideal carbon-neutral energy carrier, it can be combusted to liberate energy without any harmful side products other than water at the point of use.² As the substitute energy carrier for fossil fuels, hydrogen could be an excellent candidate to store and convert solar energy *via* the chemical bond between two hydrogen atoms.^{3,4} In industry, more than 90% of hydrogen gas produced through conventional fossil path through steam reforming of syngas ($\text{CH}_4(\text{g}) + \text{H}_2\text{O}(\text{g}) \rightarrow \text{CO}(\text{g}) + 3\text{H}_2(\text{g})$).⁵ Nevertheless, this process usually consumes fossil fuels and releases CO and CO₂. Additionally, the non-renewable process precludes its application regarding the deep decarbonization of global energy system. In fact, water is a potential resource for being the most plentiful supply of hydrogen that can be used to produce hydrogen through electrocatalytic^{6,7} or photocatalytic^{8,9} water splitting. Despite the environmental benign, the green hydrogen produced through water electrolysis holds merit of generating more than 99.9% very high purity compare to other low-carbon hydrogen production pathways.¹⁰ In addition, with water electrolysis, excess electrical energy generated from solar and wind power, hydropower, biomass and geothermal energy can be chemically stored in hydrogen bonds, therefore balance the discrepancy between energy demand and production and potentially lowered the hydrogen production costs.¹¹

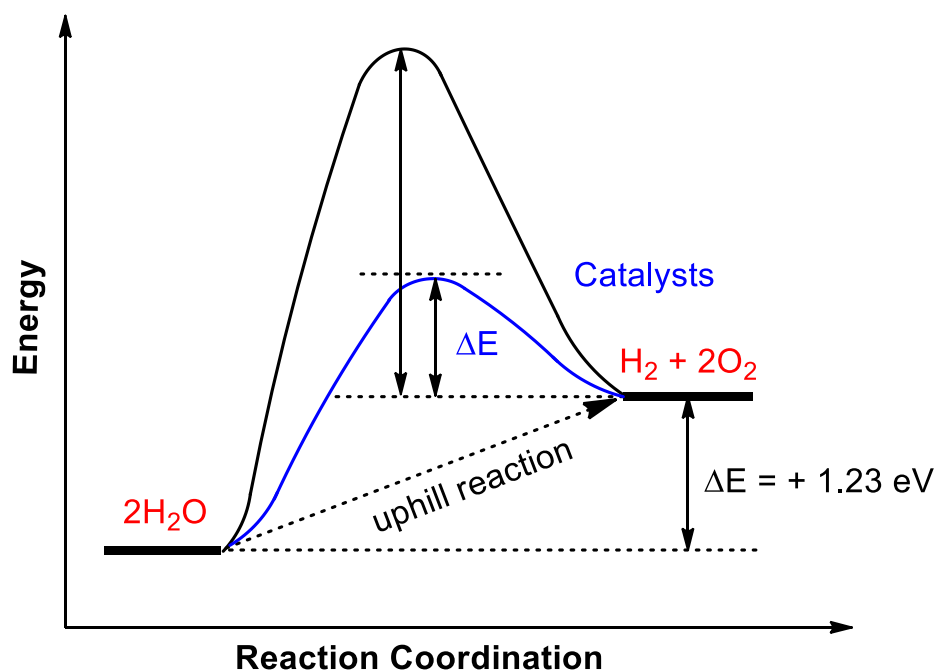
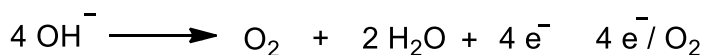
Electrochemical splitting of water consists of two half reactions, which are hydrogen evolution reaction (HER) and oxygen evolution reaction (OER) to form H₂ and O₂ respectively.¹² As illustrated in Figure 1, it proceeds through the reduction (oxidation) of protons (hydroxides) of water molecules accompanied by the subsequent evolution of gas just as its name implies. However, both reactions have proven to be challenging due to their high overpotential and sluggish kinetics with a positive free energy of +237 kJ/mol (1.23 V vs. RHE) at 25°C and 1 atm which origin from the multistep proton and electron transfer processes from both cathodic reduction and anodic oxidation.¹³ In this regard, efficient electrocatalysts can accelerate the rate of related



Acid solution : Hydrogen Evolution Reaction (HER)



Base solution : Oxygen Evolution Reaction (OER)



Scheme 1. Schematic description of energy diagram for water splitting.

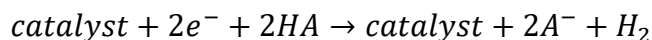
electrons transfer processes through an alternative mechanism involving different transition states to lower activation energy are required for each half-cell reaction (Scheme 1).^{13,14} To date, the most efficient catalysts for HER in acidic electrolytes is platinum metal^{15,16} while the benchmark catalysts for OER electrocatalysts are iridium and ruthenium oxides in alkaline environment¹⁷⁻¹⁹. However, the unstable intermediates²⁰⁻²² and the scarcity of precious metals severely limited their large-scale viability and widespread use. Therefore, the development of robust and available non-noble metal and metal free electrocatalysts in various electrolysis conditions for both HER and OER is highly desirable.

Chapter 2

Regulatable Molecular porphyrins catalyzed hydrogen evolution reaction

2.1 INTRODUCTION

Electrocatalysts can be generally categorized as either homogeneous or heterogeneous depending on whether or not they function in the same phase as the reactants. Homogeneous redox electrochemical reactions consists of the generation of the active form of a catalyst that able to exchange electrons with the substrates at a potential less negative (for reduction reaction) or less positive (for oxidation reaction) than the potential required for reducing or oxidizing the substrate directly at the electrode surface.²³ Compared with heterogeneous system, homogeneous catalysts diffuse freely in the solution that contains the substrate and the electrode material does not participate in the electrochemical reaction. In other words, the electrode only plays the role of a heterogeneous outersphere electron donor (or acceptor).²⁴ The direct reduction (or oxidation) of the substrate requires an overpotential to give rise to a significant current which provide us more insight to the catalytic process. In water splitting reaction, the homogeneous system can give more reaction mechanism details since electrocatalytic pathway turns into molecular level. The redox events in cyclic voltammograms can help to determine the transient intermediates that have electrochemical and chemical characteristics. At this point, the formation of a solar fuel such as H₂, involves multiple electron transfer (ET) and proton transfer (PT) steps.²⁵⁻²⁸ During the reaction, the electrochemical activity of catalysts always evaluated in organic solvent, such as THF, acetonitrile, DCM, etc., where an electrode supplies electrons and a Brønsted acid (HA) provides protons as shown in the following equation:



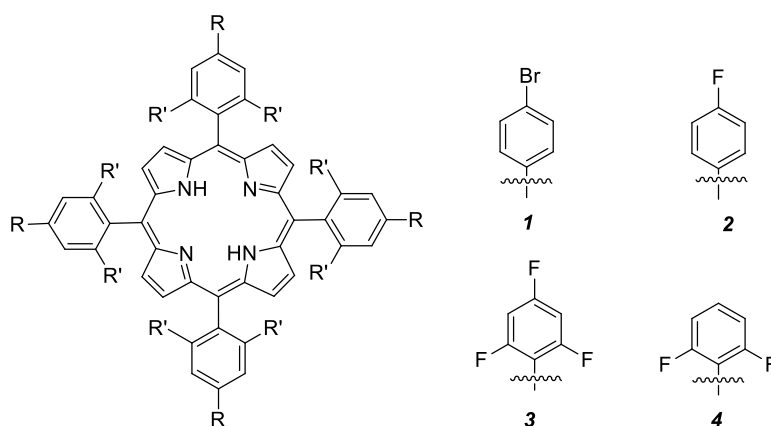
To avoid the build-up of charge, the two processes are often interdependent, giving rise to proton-coupled electron transfer (PCET) reactions.²⁹⁻³³ These steps can precede stepwise, one before the other, or in a concerted fashion where protons and electrons transfer simultaneously. Fully understanding the detailed PCET mechanisms and the formation of intermediates during hydrogen evolution reaction holds promise for rational design of energy-efficient catalysts.

Homogeneously hydrogen evolution reaction (HER) is a prototypical electrochemical reaction for catalyst design and mechanism exploration towards water splitting reaction. Most of electrocatalysts design are based on naturally occurring enzymes, for example, hemoglobin and

hydrogenases, which are able to catalyze both HER and OER with an activity comparable to platinum.^{34–36} In this context, organometallic molecules based on non-noble metals appear to be useful to precisely tailor and regulate for adapting the local environment of active sites.³⁷ Among numerous reported organometallic compounds that can catalyze HER, metalloporphyrins show great potential for facilitating the proton coupled electron transfer in water splitting reaction.^{38,39} Aside being a rigid and stable coordination sphere for the metal center, porphyrin can also affect the catalysts behavior through varying electron density on the metal active sites.^{40,41} Compared with metalloporphyrin, free-base porphyrins also exhibit rich multielectron redox chemistry due to the π -conjugated system.⁴² Inspired by the metalloporphyrin catalysts, the four nitrogens in the porphyrin core could act as pendant base and generate protonated species which mimic metal hydride intermediates. Furthermore, modulation the basicity of imide by different electron-withdrawing substituted groups on *meso* position can also result in stepwise or concerted PCET pathway.³⁹ A former graduate student in the Villagrán's lab, Dr. Yanyu Wu, found that free-base *meso*-tetra(pentafluorophenyl)porphyrin can also be used as HER electrocatalyst with a comparable electrocatalytic activity with the metallated macrocyclic complexes⁴³. They demonstrated the catalytic wave appeared at -1.31 V vs Fc/Fc⁺ when successive titrate with tosic acid into the free-base porphyrin THF solution. The product and efficiency were confirmed with gas chromatography after controlled-potential bulk electrolysis, result in hydrogen generation with 90% faradaic efficiency. Mechanistic studies of the corresponding PCET reaction pathways were carried out through UV-vis spectroelectrochemistry analysis and thermodynamic theoretical calculations in order to reveal the spectral signatures of the intermediates and the related free energy during evolution of hydrogen. The results suggest the most favorable mechanistic process is a sequence with one electron reduction followed by protonation to form [porphyrin-H] intermediate followed a proton coupled electron transfer to evolve dihydrogen and regenerate porphyrin catalyst.

Based on Yanyu's work, we synthesized four metal free porphyrins, namely 5,10,15,20-tekis(4-bromophenyl) porphyrin (**1**), 5,10,15,20-tekis(4-fluorophenyl) porphyrin (**2**), 5,10,15,20-tekis(1,3,5-trifluorophenyl) porphyrin (**3**), 5,10,15,20-tekis(2,4-difluorophenyl) porphyrin (**4**), as catalysts to generate hydrogen electrochemically (**Scheme 2**). The electron-withdrawing ability of *meso*-substituent group will lead to various basicity for the imine group in the porphyrin core, which result in different reaction mechanisms according to the sequence of protonation and

reduction processes in the PCET pathway. All the free-base porphyrins in this work are catalytic active towards hydrogen generation in THF with tosic acid as proton substrate. The product hydrogen gas was confirmed by gas chromatography after long-term bulk electrolysis. Among these, mono-*meso* substituted porphyrins (bromo- and fluoro-) are proposed to have a PPEE mechanism with overpotential of -1.54 V vs. Fc/Fc^+ and -1.56 V vs. Fc/Fc^+ whereas difluoro-phenyl porphyrin and trifluoro-phenyl porphyrin follow an EPPE pathway. Measurement of Faradaic efficiency was evaluated after controlled-potential bulk electrolysis, showed that a PPEE mechanism is more favored for the hydrogen evolution for the 100% faraday yield when (4-bromophenyl)porphyrin as electrocatalyst.



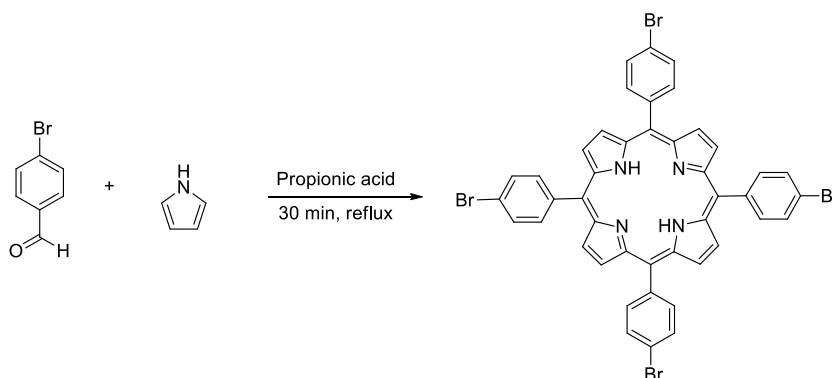
Scheme 2. The as-synthesized porphyrin electrocatalysts.

2.2 MATERIALS AND METHODS

All reagents used for synthesis were purchased from Sigma Aldrich. Pyrrole was freshly distilled prior to use. Solvents used for electrochemical studies were dried and degassed through a Pure Process Technology solvent purification system. Tetrabutylammonium hexafluorophosphate (TBAPF_6) and tosic acid were purchased from Acros Organics. Meso-tetra(pentafluorophenyl)porphyrin and meso-tetraphenylporphyrin were synthesized according to Lindsey's method. Deionized (DI) water from Milli-Q ultrapure water purification system (Millipore Co.)

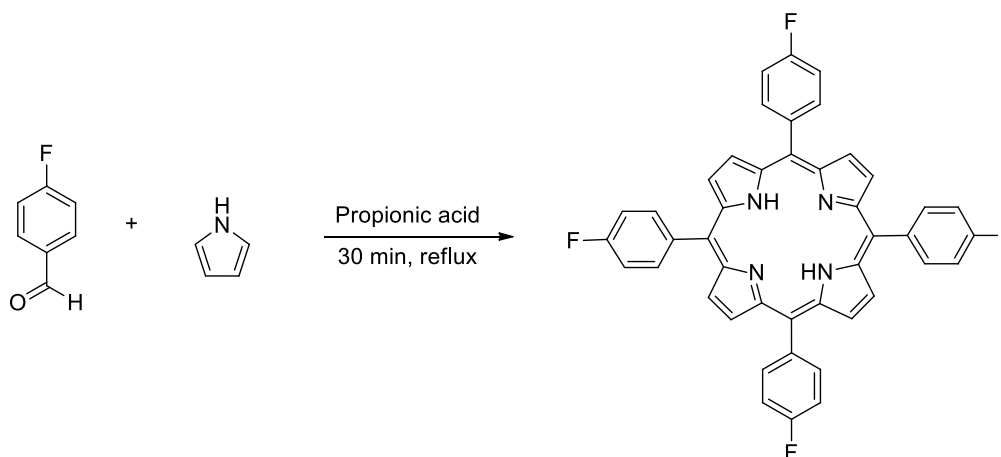
2.3 SYNTHESSES

2.3.1 Synthesis of 5,10,15,20-takis(4-bromophenyl) porphyrin (1)



In a 500 mL round bottom flask, propionic acid (125 mL) and 4-bromobenzaldehyde (1.85 g, 10 mmol) were mixed in the room temperature. After the reaction mixture was heated up to 125°C, pyrrole (0.7 mL, 10 mmol) was rapidly injected into the solution and the mixture was stirred at 125°C for 30 min. Cooled down the reaction and filtered the reaction mixture with DI water and MeOH and dried under vacuum overnight get the 4-bromopheny porphyrin. (0.19 g, yield: 21.5%) UV-vis (λ_{max} nm in THF at 298 K): 421.5, 516.1, 550.9, 594.1, 650.7 nm, ^1H NMR (600 MHz, CDCl_3 , 25 °C): δ 8.84 (d, 2H), 8.06 (d, 2H), 7.91(br, 2H, N-H).

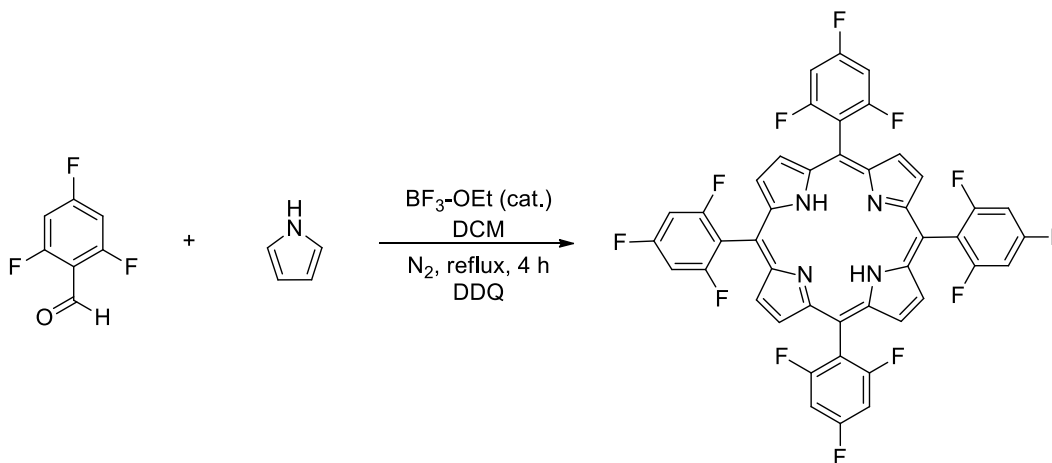
2.3.2 Synthesis of 5,10,15,20-takis(4-fluorophenyl) porphyrin (2)



In a 500 mL round bottom flask, propionic acid (125 mL) and 4-fluorobenzaldehyde (2.5 g, 20 mmol) were mixed in the room temperature. After the reaction mixture was heated up to 125°C, pyrrole (1.4 mL, 20 mmol) was rapidly injected into the solution and the mixture was stirred at 125°C for 30 min. Cooled down the reaction and filtered the reaction mixture with DI water and

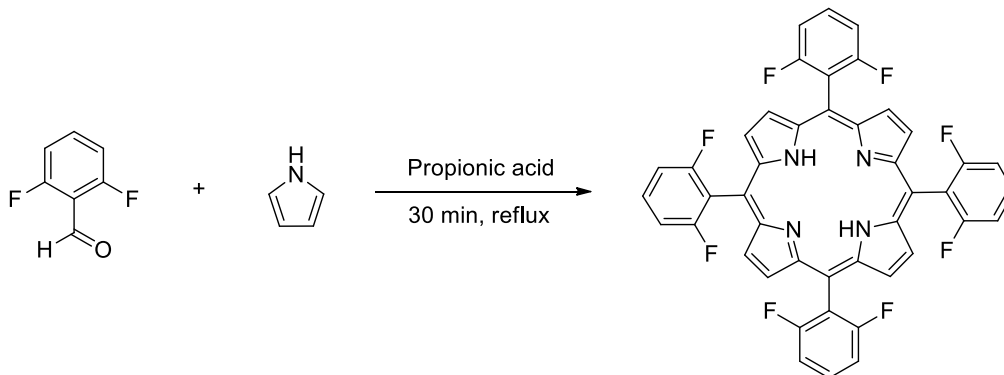
MeOH and dried under vacuum overnight get the 4-fluoropheny porphyrin. (1.82 g, yield: 13.37%) UV-vis (λ_{\max} nm in THF at 298 K): 417.5, 518.2, 553.3, 594, 652.1. ^1H NMR (600 MHz, CDCl_3 , 25°C): δ 8.84 (s, 8H, β -pyrrole), 7.46 (m, 8H, 2,6-(4-fluorophenyl)), 8.17 (d, 8H, 3,5-(4-fluorophenyl)).

2.3.3 Synthesis of 5,10,15,20-tekis(2,4,6-trifluorophenyl) porphyrin (3)



A mixture of tri-fluorobenzaldehyde (1.6g, 10 mmol) and pyrrole (0.7 mL, 10 mmol) were dissolved in DCM under N_2 atmosphere. 0.5 mL of $\text{BF}_3 \cdot \text{OEt}$ was added and the reaction was refluxed for 4 hours. After cooling down, DDQ (2.17g, 10 mmol) was added to the mixture and reacted for 30 min in order to oxidize the porphine intermediate. After the reaction is done, the reaction was dried under reduced pressure, the dark black product was dissolved in CHCl_3 . A dark red solution filtrate was obtained which was the crude porphyrin product after dried the solution. The crude product was washed with DCM several times and got the purified HTF₃PP (0.74 g, yield: 8.4%) UV-vis (λ_{\max} nm in THF at 298 K): 413.9, 508.9, 545.1, 588.7, 639.4. ^1H NMR (600 MHz, CDCl_3 , 25°C): δ 8.89 (s, 8H, β -pyrrole), 7.18 (d, 8H, 3,5-(2,4,6-trifluorophenyl))

2.3.4 Synthesis of 5,10,15,20-takis(2,6-difluorophenyl) porphyrin (4)



In a 500 mL round-bottom flask, propionic acid (125 mL) and 2,6-difluorobenzaldehyde (1.42g, 10 mmol) were mixed in room temperature. The solution was heated up to 125°C, pyrrole (0.7 mL, 10 mmol) was rapidly injected into the solution and stirred under 125°C for 30 min. After the reaction was cooled down, the flask was placed in the fridge overnight. Porphyrin crystals were formed in the solution which colored purple. The crude product was washed with MeOH and DI water and obtained pure porphyrin (0.36g, yield: 4.7%) UV-vis (λ_{\max} nm in THF at 298 K): 411.7, 508.9, 588.4, 565.9, 657.7. ¹H NMR (600 MHz, CDCl₃, 25°C): δ 8.87 (s, 8H, β -pyrrole), 7.38 (m, 8H, 4-(2,6-difluorophenyl)), 7.80 (d, 8H, 3,5-(2,6-difluorophenyl)).

2.4 RESULTS AND DISCUSSION

2.4.1 Cyclic voltammetry

Cyclic voltammetry experiments were performed in THF in order to assess the electrocatalytic activity of the four as-synthesized porphyrins (1-4). Porphyrin **1** and **2** exhibited similar CV shape upon titrating with tosic acid, which indicates a similar PCET mechanism (Figure 1). For the mono-substituted porphyrin, **1** shows two reversible one-electron reductions at $E_{1/2} = -1.308$ V and $E_{1/2} = -1.650$ V vs. Fc/Fc^+ in the absence of acid, which indicate the generation of porphyrin radical anion and the dianion species. Upon the addition of 0.6 mM tosic acid, the reaction solution changed from dark maroon to green, and the two reversible events remain but shifted to more negative potential, while a quasi-reversible peak arise at $E_{1/2} = -0.605$ V, means the chemical protonation process of mono-substituted porphyrin occur before the electron reduction⁴³. This protonation wave starts to grow along increasing the concentration of acid. At the same time, a catalytic wave appeared at -2.040 V. It is worthy to mention that the two one-electron reversible events decreased gradually until disappeared during electrolysis, while the protonation peak and catalytic peak become major events denotes the formation of intermediates in the meantime porphyrin catalyst deplete near the electrode. Catalyst **2** possesses a similar behavior as titrate with acid, implies resemble intermediates are generated in the reaction, as well as the mechanism.

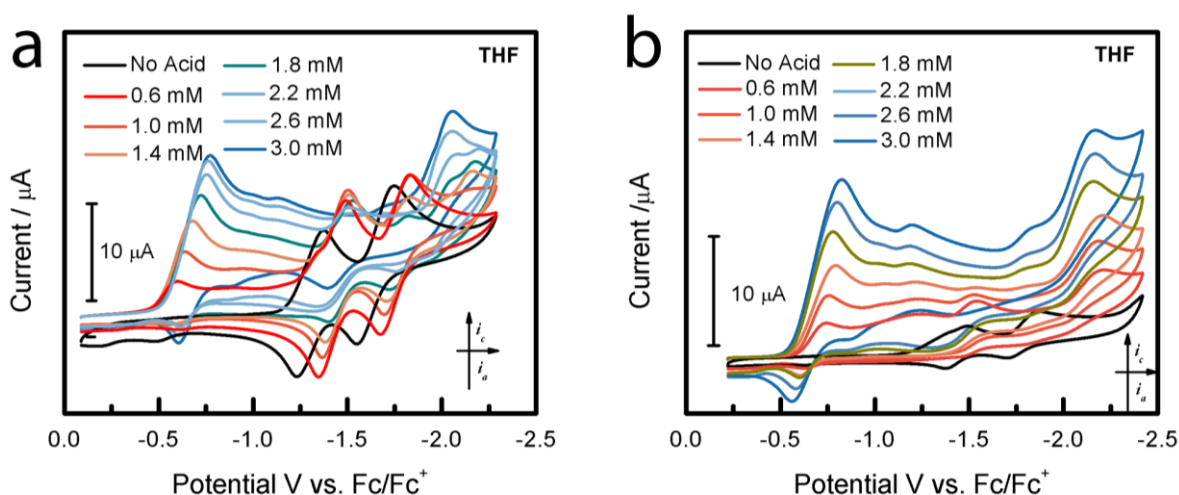


Figure 1. Cyclic Voltammetry of H_2TBrPP , **1** (a) and H_2TFPP , **2** (b) in solutions containing 0.1 M TBAPF_6 and in presence of acid. Scan rate: 100 mV/s.

Porphyrins **3** and **4** are designed to be more electrophilic on imine nitrogen since more electron-withdrawing groups on the *meso*-position compared with **1** and **2**. When **3** and **4** were used as electrocatalysts, the CV shape is different with neither mono- nor per-substituted catalysts (Figure 2). Similar with **1** and **2**, the two-electron reduction waves with different potentials are observed due to the redox property of free-base porphyrin **3** and **4**.

However, the protonation wave does not show in the cyclic voltammetry when successive addition of tosic acid (-0.605 V). Instead, a new peak generated after the first electron reduction potential at -1.022 V and -1.480 V, this suggests that the protonation of **3** and **4** is impossible

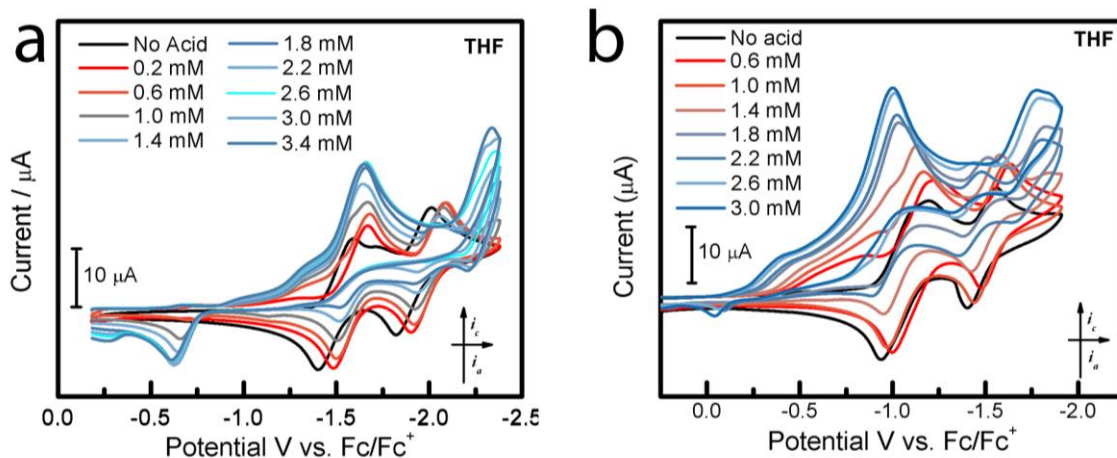


Figure 2. Cyclic Voltammetry of $\text{H}_2\text{TF}_3\text{PP}$, **3** (a) and $\text{H}_2\text{TF}_2\text{PP}$, **4** (b) in solutions containing 0.1 M TBAPF_6 and in presence of acid. Scan rate: 100 mV/s.

without the electrochemical processes. As the potential sweep to more negative region, the catalytic peak appears at -1.610 V vs. Fc/Fc^+ (-1.000 V vs. Fc/Fc^+ for porphyrin **4**) in the presence of acid. At this point, only two waves appeared in the CV, implies the electron transfer processes are separated.

2.4.2 Bulk electrolysis

In order to evaluate the efficiency of as-synthesized porphyrins (**1-2**) for hydrogen evolution, bulk electrolysis was carried out under controlled-potential with the present of acid for 3 hours. A special H-cell with a frit in between cathode and anode was used to collect the gas generated during the bulk electrolysis. All the tested porphyrin catalysts show stable current

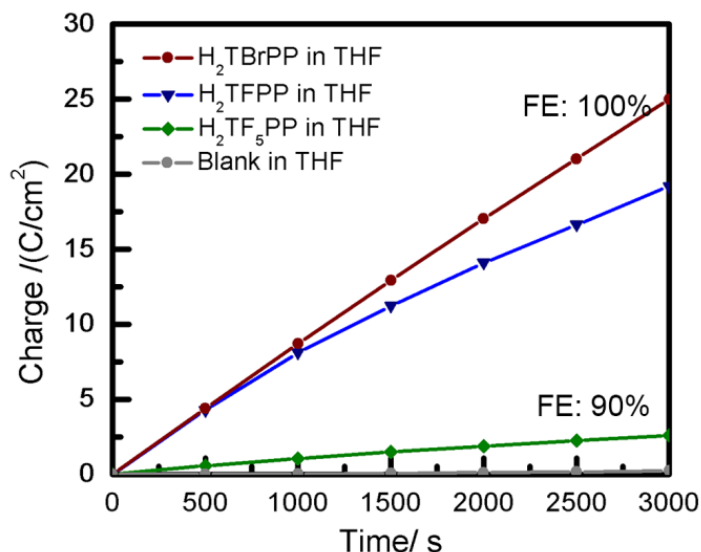


Figure 3. Charge passed plot versus time of as-synthesized porphyrin **1** (red) and **2** (blue) compared with the reported perfluorophenyl porphyrin (green) and the blank THF (grey) under bulk electrolysis condition in the presence of acid.

response over with time, indicated their excellent durability under electrolysis condition. Among these porphyrins, catalyst **1** possesses the most total charge passed through the electrolysis (Figure 3), furthermore, the linearity of the charge plot with respect to time suggests the high yield of gas production. Combine with gas chromatography, the faraday efficiency was calculated by the percentage of *moles* of hydrogen generated in experiment to the theoretical hydrogen yield, by following Faraday yield equation: Faraday yield = $n \times N \times F / Q$, where N is avogadro's number, n is the number of electrons evolved in the reaction, Q is total charge passed during the electrolysis and F is the Faraday constant. The mono-substituted porphyrins have better efficiency in which **1** shows 100 % faraday efficiency that better than the reported *meso*-pentafluorophenylporphyrin where only have 90 % faraday efficiency at a similar electrolysis condition.

2.4.4 Spectroelectrochemistry analysis

UV-vis spectroscopy combined with bulk electrolysis was performed for all the candidate porphyrin catalysts in order to reveal the mechanism for electrocatalytical hydrogen generation. By observing intermediates that have the adsorption at ultraviolet and visible region (190 nm to 750 nm) in different conditions, the detailed reaction pathway will be revealed. For a free-base porphyrin, a Soret band at around 420 nm along with four small Q-bands between 470 and 650 nm can be observed in the UV-vis spectroscopy in THF. For catalysts **1**, a new intense absorbance appears at 445 nm when titration of tosic acid, whereas the original Soret band decreased (Figure 4). This indicates that in THF, porphyrin **1** can be protonated by tosic acid, which in agreement with HA/H⁺ peak at -0.605 V in the cyclic voltammogram. When subject this protonation solution to the controlled-potential bulk electrolysis at the first one-electron reduction potential (-1.308 V vs. Fc/Fc⁺), a decrease of the 445 nm Soret band and Q-IV band (652 nm) suggests the consumption of the protonated species under the electrolysis condition. When performing bulk electrolysis at the potential above the second electron reduction wave (-1.65 V vs. Fc/Fc⁺) without the presence of acid, the recorded spectrum remains unchanged. Upon addition of tosic acid, no obvious new peak appears. However, the shoulder at around 300 nm grows dramatically along with the increase of Soret peak (420 nm) and an isosbestic point at 450 nm, this denotes the electron transfer process is the last step to reform the porphyrin catalyst. Similarly, porphyrin **2** possesses

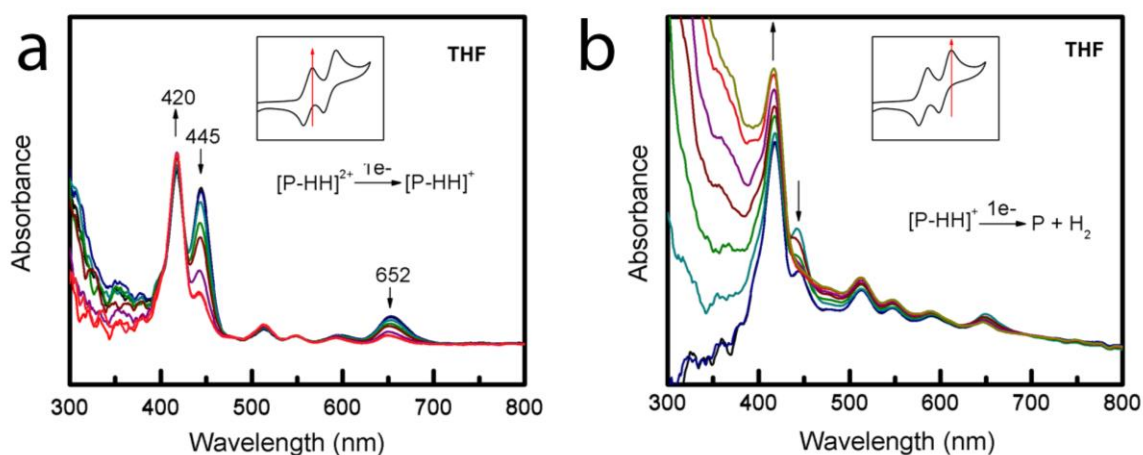


Figure 4. The UV-vis spectrum of **1** under one-electron reduction potential (a) and two-electron reduction potential (b) in the absence of acid.

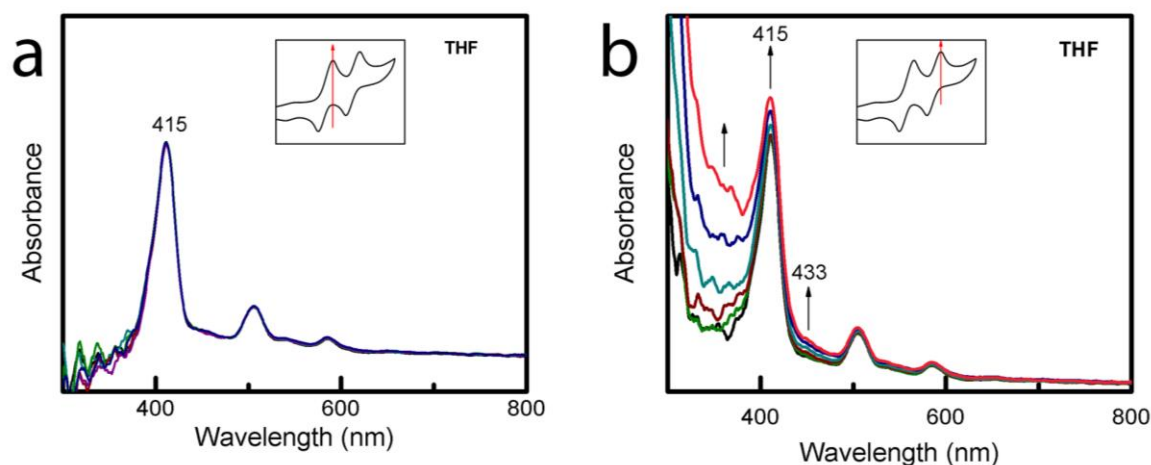


Figure 5. The UV-vis spectrum of **3** under one-electron reduction potential (a) and two-electron reduction potential (b) in the absence of acid.

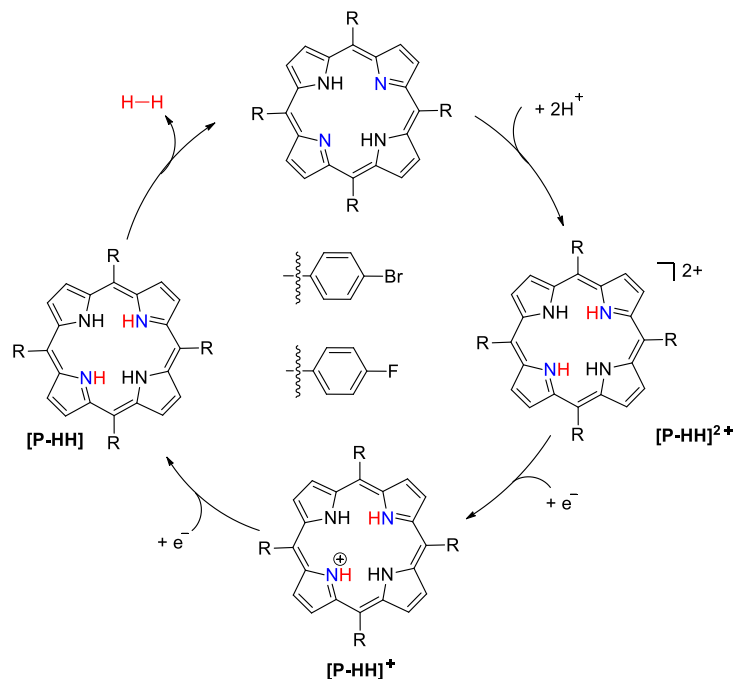
the same UV-vis spectrum behavior with slightly different wavelength, which consistent with the electrochemistry measurements.

However, for the catalysts **3** and **4**, the UV-vis spectrum remains the same when adding the acid, which indicates in THF, tosic acid is not strong enough to protonated **3** and **4**. This is also in accordance with the cyclic voltammetry for the absence of protonated event. As subject the catalysts under the controlled-potential electrolysis at one-electron reduction potential (-0.850 V vs. Fc/Fc^+ for porphyrin **3**, -1.120 V vs. Fc/Fc^+ for porphyrin **4**) with existence of acid, no new peaks appeared in the UV-vis. A similar spectrum was observed along with the growth of Soret band (415 nm) when the second reduction potential applied. This phenomenon shows the intermediates generated during the electrolysis cannot be detected in the UV-visible region. However, an increasing of shoulder peak around 300 nm appeared. This phenomenon is similar as the catalyst **1** when two-electron reduction potential was applied to the system, suggesting the electron transfer process happened at the last step of catalytical cycle and facilitated the regeneration of porphyrin catalyst (Figure 5).

2.4.5 Proposed mechanism

Based on the experimental results demonstrated above, mechanisms for the HER catalyzed by two types of metal-free porphyrins are proposed. For porphyrin **1** and **2**, since the electron-withdrawing ability (-Br and -F) on the *meso*-phenyl group is relative weak, the imine-nitrogen is able to be protonated in the presence of Brønst acid. This is proved by the proton reduction peak

appeared in the cyclic voltammogram and the UV-vis spectrum. Due the fact that the two nitrogens

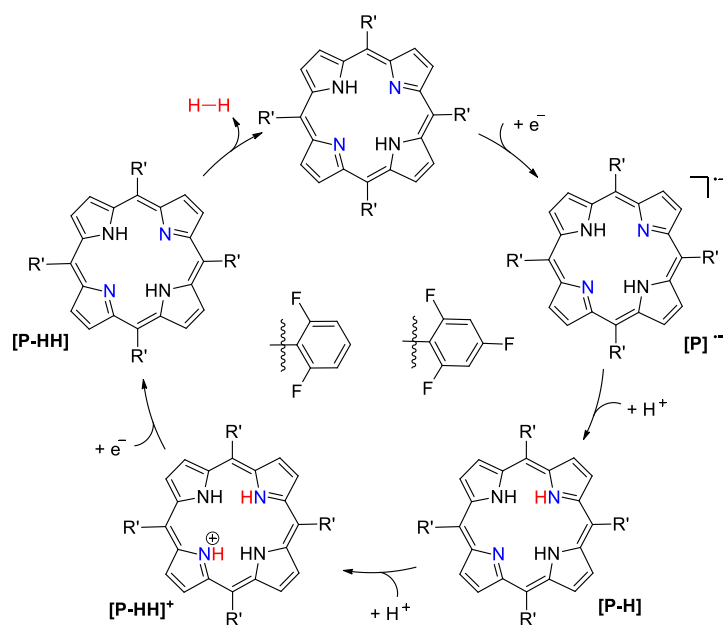


Scheme 3. Proposed mechanistic reaction pathway for **1** and **2** catalyzed hydrogen evolution reaction.

in the symmetric porphyrin core are identical, the protonation of the two nitrogens must process at the same time. As a result, the first intermediate should be $[I-HH]^{2+}$ with protonation-protonation steps in the reaction pathway (Scheme 3). Upon applying the potentials on electron-reduction and two-electron reduction, the porphyrin catalysts are able to regenerate and complete the catalytical cycle. Since two electrons and two protons are involved in the reaction, therefore, a P-P-E-E (Protonation-Protonation-Electron-Electron) catalytic pathway can be assigned for mono-substituted type of porphyrin catalysts.

In the case of porphyrin **3** and **4**, the electron-withdrawing groups (di-fluoro and tris-fluoro) are able to pull the electrons from the conjugated system, result in a slightly charge polarization on the nitrogen. At this point, the addition of acid can not protonate the imines due to the electron deficient feather unless additional electron is subject to the system. Therefore, we propose the first step to be an electron transfer. Due to the fact that no intermediates (new peaks) can be observed in the UV-vis region under the one and two-electron reduction potential, we are not able to assign the sequence of next several steps. However, the similar UV-vis responds with the second electron reduction of mono-substituted type porphyrin gives us a clue the last step would be electron transfer. Therefore, the proposed mechanism of catalysts porphyrin **3** and **4** should be E-P-P-E

(Electron-Protonation-Protonation-Electron) pathway (Scheme 4). This sequence is also in good agreement with the P-E-P-E reaction pathway of reported *meso*-pentafluorophenylporphyrin, in which the addition of one electron to the porphyrin system is not enough to balance the polarity and form double protonated species due to the strong electron pulling effective of *meso*-phenyl groups. As a result, another electron is need for the second protonation to form the essential intermediate for hydrogen generation.



Scheme 4. Proposed mechanistic reaction pathway for **3** and **4** catalyzed hydrogen evolution reaction.

2.5 CONCLUSION

In conclusion, we have studied the electrocatalytic generation of hydrogen using five metal-free porphyrins (**1-4**). The catalytic activities were studied through cyclic voltammetry and controlled-potential electrolysis. All the as-synthesized porphyrin catalysts can serve as efficient electrocatalyst for hydrogen generation in THF solution when tosic acid is used as proton source. Combined with UV-vis spectroscopy with bulk electrolysis, **1** and **2** are proposed undergo a same P-P-E-E- catalytic mechanism whereas **3** and **4** are favored for an E-P-P-E mechanistic reaction pathway. Among these catalysts, porphyrin **1** exhibits the highest faraday efficiency (100%), which is better than the reported *meso*-pentafluorophenylporphyrin. Future work including determination of the overpotential for each electrocatalysts by means of gas chromatography under different potential controlled electrolysis, stability test and the faraday efficiency measurement can

give us more details about how the substituent groups affect the efficiency and mechanism pathways during the hydrogen generation.

2.6 ^1H NMR DATA

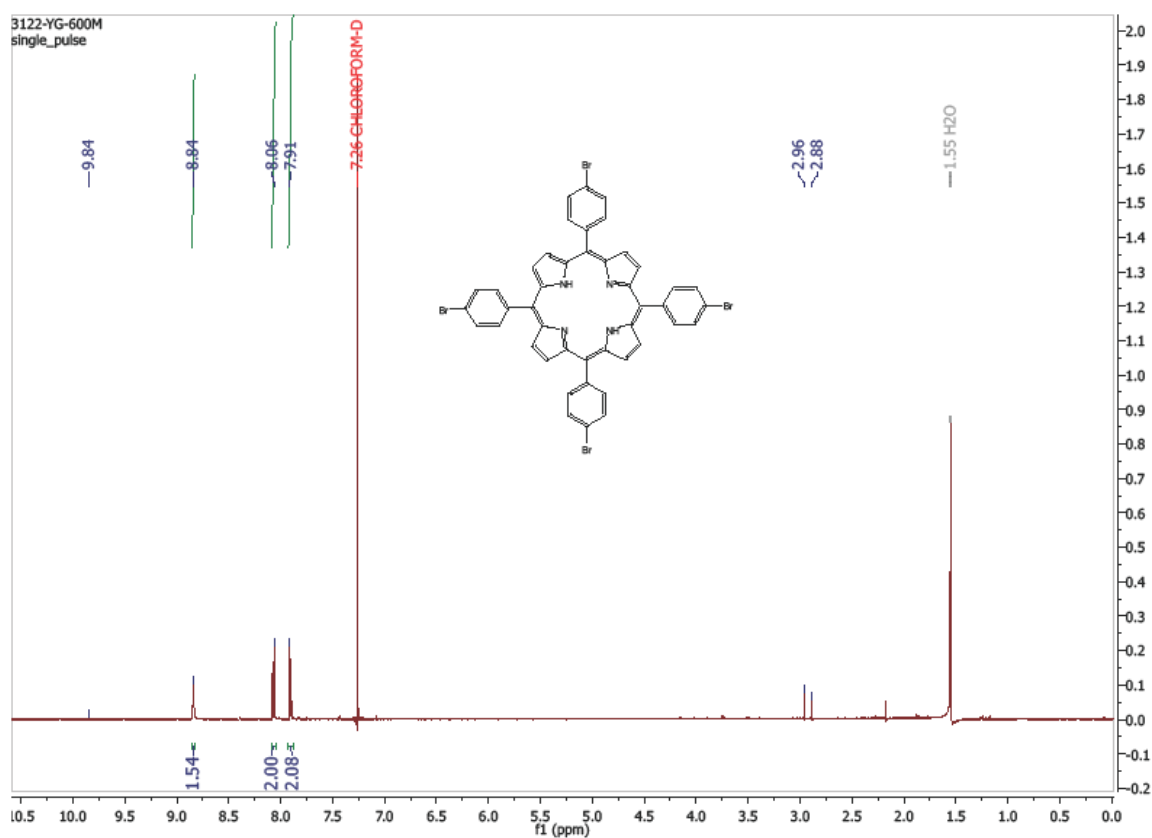


Figure 7. ^1H NMR spectrum of 4-bromophenyl porphyrin(1)

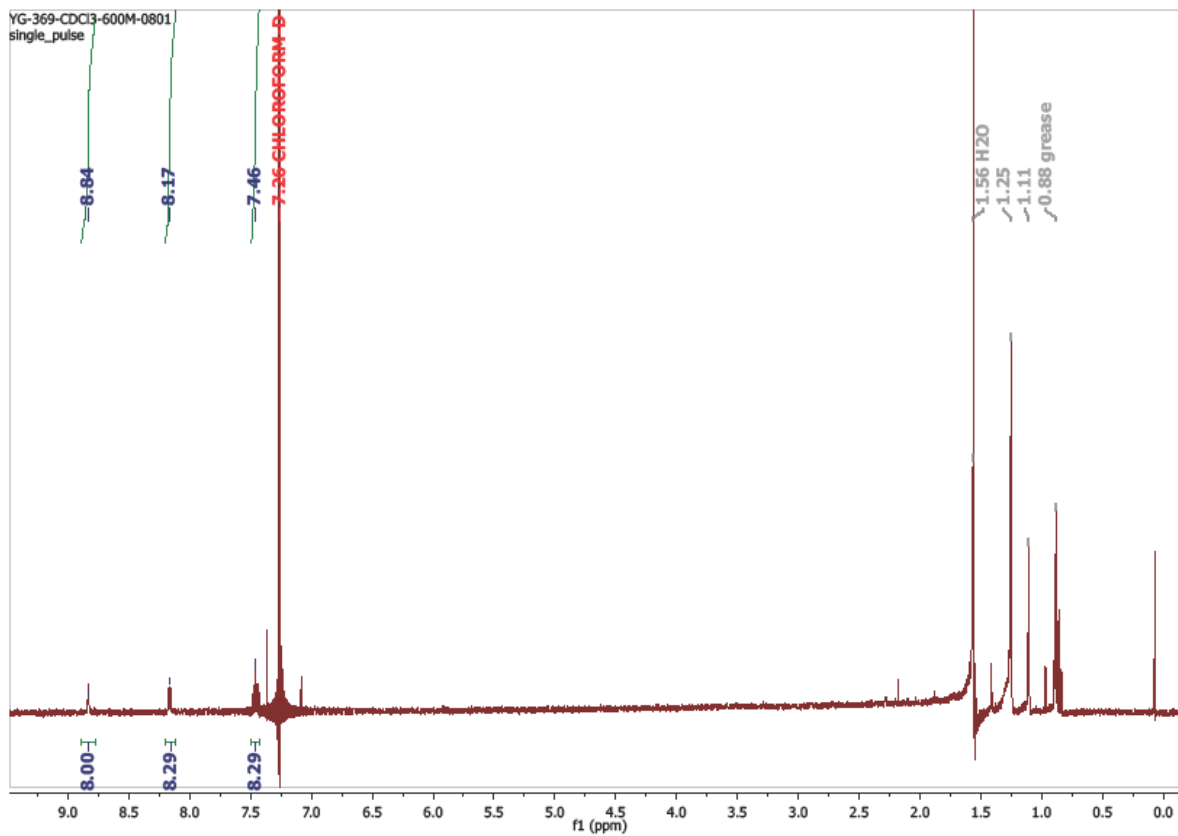


Figure 8. ^1H NMR spectrum of 4-fluorophenyl porphyrin(2)

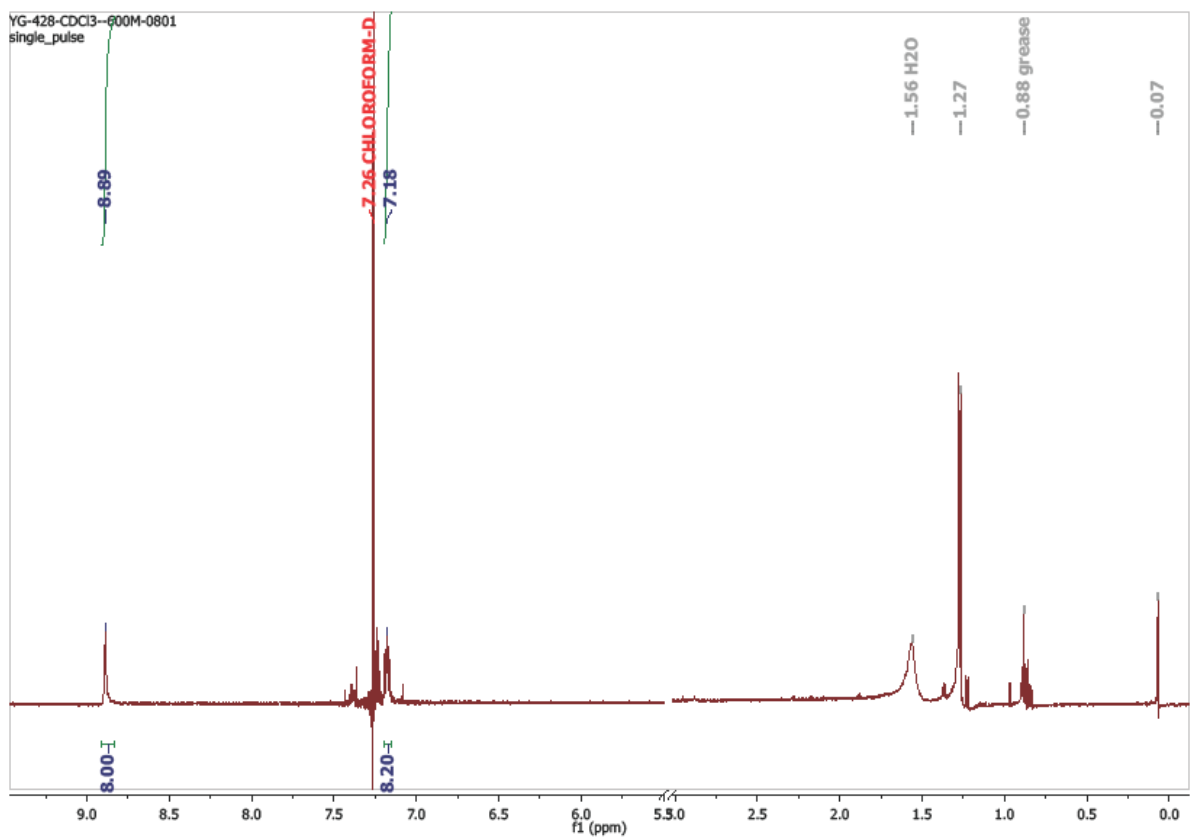


Figure 9. ^1H NMR spectrum of 2,4,6-trifluorophenyl porphyrin(3)

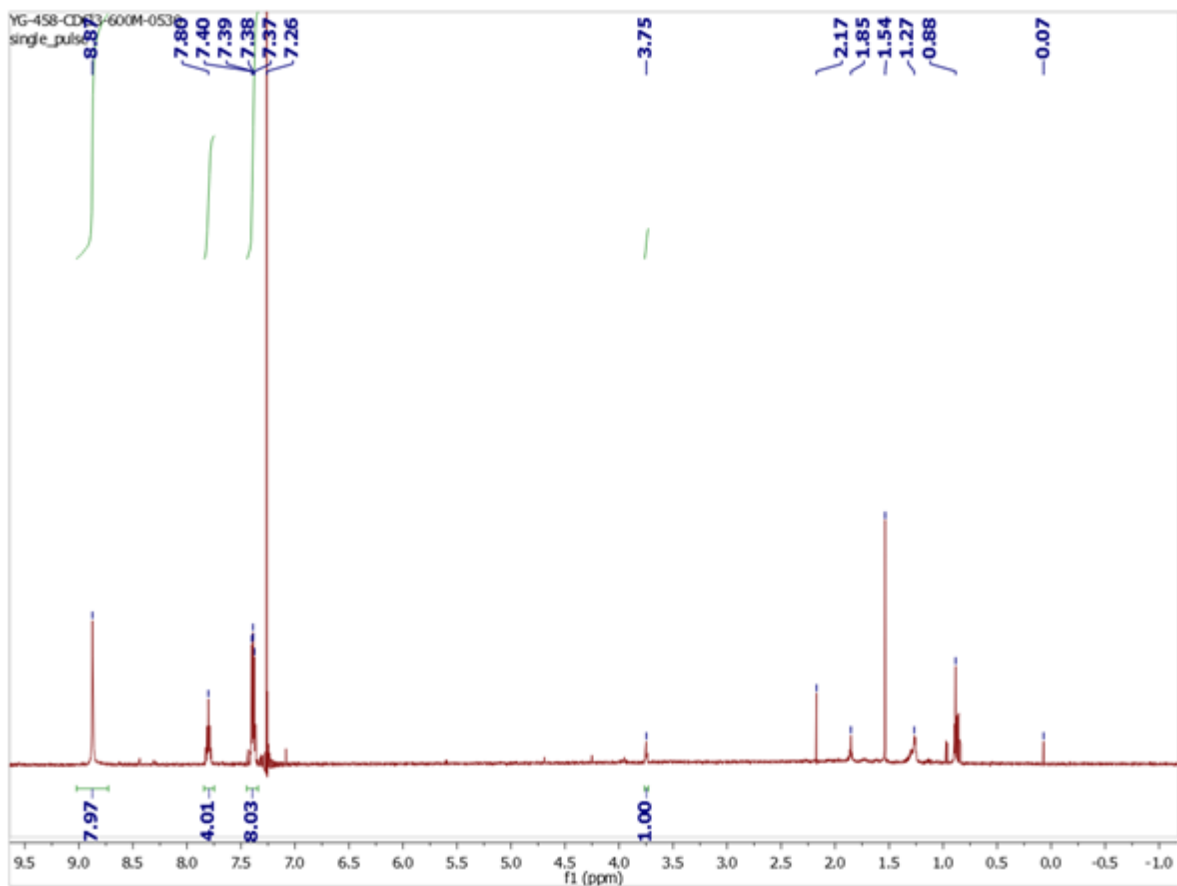


Figure 10. ¹H NMR spectrum of 2,6-fluorophenyl porphyrin(4)

Chapter 3*

Free-base porphyrin polymer for bifunctional electrochemical water splitting

3.1 INTRODUCTION

Porphyrins are organic macrocycles that have conjugated aromatic rings and characteristic intense colors.⁴⁴ Porphyrin-based catalysts for water splitting have been exclusively focused on metallated complexes.^{45–54} The generation of high-valent metal-oxo intermediates is the key step to form molecular oxygen, where the porphyrin scaffold serves only as a molecular frame to facilitate the multi-electron transfer process, and a metal center is responsible for the catalytic activity.^{49,55,56} Similar mechanisms are invoked in HER which have metal-hydride intermediates as proton transfer carriers.^{47,48,57} However, it has been shown that the catalytic activity of porphyrin complexes towards hydrogen generation does not necessarily require a metal center.^{43,58} The N–H groups and N-lone pairs in the core of free-base porphyrins can also act as active sites for hydrogen generation under acidic conditions.⁵⁹ Electronic tuning at the meso-position by electron donating or withdrawing groups can yield porphyrin complexes with varied basicity that lead to distinct redox reactivity.^{60,61} Our previous work shows that a metal-free porphyrin with perfluorinated meso-substituted groups can electrocatalyze hydrogen generation in acid with a potential of -1.31 V (vs. Fc/Fc^+) and 90% faradaic efficiency.⁴³ However, molecular level electrocatalysts suffer from stability issues, low current densities, high cost, and non-recyclability for industrial utilization.⁶² Therefore, developing low-cost heterogeneous electrocatalysts that possess high reactivity and stability towards water splitting could be a promising strategy for hydrogen and oxygen production.

Poly(p-phenylene terephthalamide) (PPTA) fibers are a type of ultra-strong synthetic polymer with a high tensile strength-to-weight ratio. The amide linkages from hydrogen bonds between the polymer chains which act like “hydrogen bond locks”, making it a material for bullet-proof body armors. Incorporating units of free-base porphyrins into PPTA networks can result in two-dimensional (2D) porphyrin-based polymers with ordered columnar π -arrays. Porphyrin

* *This project is already published, see:*

Journal: **Yulu Ge**, Zhenhua Lyu, Mariana Marcos-Hernandez, Dino Villagran, Porphyrin-based metal free polymer as a bifunctional electrocatalyst for water splitting, *Chemical Science*, **2022**, 13 (29), 8597-8604.

Patent: Dino Villagran*, **Yulu Ge**, Metal-free porphyrin-based electrocatalyst, **2022**, US Patent App. 17/183,109

moieties can enhance aromatic stacking interactions and add charge transport properties, used in electrocatalytic applications. However, the use of metal-free porphyrin-based polymer as bifunctional electrocatalyst directly for both HER and OER is still underexplored.

In this chapter, we present the synthesis of a metal-free porphyrin based crystalline 2D organic polymer, Porphvlar, obtained from the condensation of terephthaloyl chloride and 5,10,15,20-tetrakis(4-aminophenyl) porphyrin, namely H₂TAPP, which is an effective bifunctional electrocatalyst for the OER and the HER in pH dependent and pH neutral solutions. The electrochemical response of this materials is explored under oxidation and reduction conditions in order to study its catalytic activity, charge transfer, and stability.

3.2 MATERIALS AND METHODS

4-Nitrobenzaldehyde (99%), tin (II) chloride dihydride (SnCl₂·2H₂O, 98+%) were purchased from Acros Organics, terephthaloyl chloride (99%) and Nafion solution (5% w/w in H₂O and 1-propanol) were obtained in Alfa Aesar, pyrrole (98%), pyridine (99%), sulfuric acid (H₂SO₄), potassium hydroxide (KOH) and 1.0 M PBS buffer (pH=7) were purchased from Fisher Scientific and used without further purification. All the glassware and cells were decontaminated by soaking in aqua regia solution (conc. HCl/ conc. Nitric acid= 3:1). The glass apparatus was washed with deionized water and oven dried. Carbon paper substrate was purchased from FuelCell Store (AvCarb P75T - 40 × 40cm), which is carbon particle-filled, polyacrylonitrile (PAN) based carbon fiber paper with hydrophobic Teflon wet-proof (13% wt treatment) coating (nominal Thickness of 0.255 mm (@ 1psi / 0.7 N/cm²).

All electrochemical measurements were performed in a three-compartment electrochemical glass cell using a CHI760D potentiostat. A graphite rod (2 mm, radius; 40 mm, length; 515 mm² surface area) was used as the counter electrode, and a saturated calomel electrode (SCE) was employed as the reference electrode. Aqueous 1.0 M KOH, 0.5 M H₂SO₄ and 1.0 M PBS buffer were used as electrolytes and purged with nitrogen gas to remove the dissolved oxygen before each measurement. To minimize the double layer charging, a low scan rate of 5 mV/s was used to perform linear sweep voltammetry (LSV). Electrochemical impedance spectroscopy (EIS) was obtained at an overpotential, η , of 250 mV from 100 kHz to 0.1 Hz with an AC voltage of 5 mV. Bulk electrolysis and chronoamperometric measurements were tested at the voltage with current density at around 10 mA, 5 mA, and 1 mA for 60 hours in ambient atmosphere. All

potentials referenced to saturated calomel electrode (SCE) were calibrated with respect to reversible hydrogen electrode (RHE) using the equation: $E = E_0 + 0.245 + 0.059 \times \text{pH}$. All the experimental potential data were calibrated at a pH of 14 for basic conditions and pH of 7 for neutral conditions and were performed at ambient temperature. All the current densities obtained were normalized by dividing the obtained current response by the geometric area of the working electrode (0.25 cm^2).

Porphylar samples were characterized by scanning electron microscopy (SEM), energy dispersive x-ray spectroscopy (EDX), and powder X-ray diffraction (pXRD). SEM and EDX studies were performed on an SEM Hitachi S-4800 instrument. Powder x-ray diffraction pXRD patterns were obtained on a Panalytical Empyrean X-ray Diffractometer. The structural characterizations were further elucidated by infrared spectroscopy (IR) through an Agilent Cary 630 FT-IR spectrometer and UV-vis spectra data were obtained with an ALS SEC2020 spectrometer system. Elemental analyses measurements were performed with a PerkinElmer 4300 DV Inductively-Coupled Plasma Optical-Emission Spectrometer (ICP-OES). Porphylar samples were digested using aqua regia at $115 \text{ }^\circ\text{C}$ for 45 min before measurement.

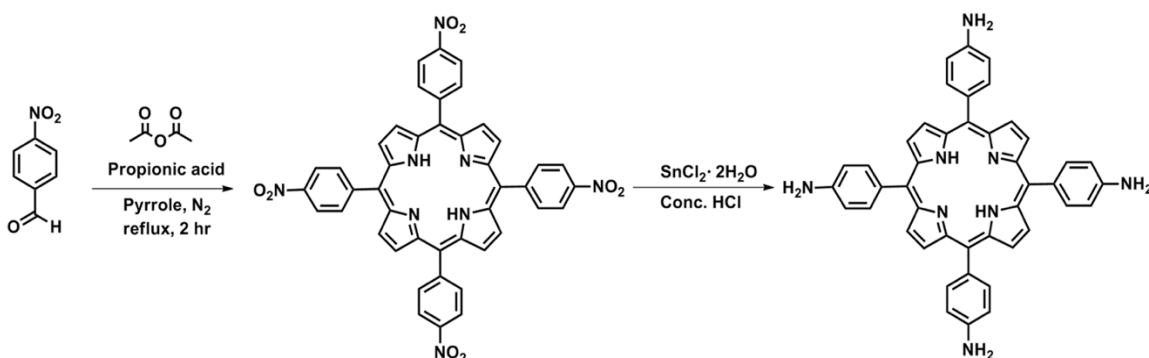
A catalyst ink was prepared by mixing catalyst powder (5.0 mg), carbon black (0.25 mg), 2-isopropanol (1.00 mL) and a Nafion solution (4.08 μL). The mixture was ultrasonicated for 30 mins to generate a homogenous dispersion. Carbon paper was cut into $0.5 \text{ cm} \times 2 \text{ cm}$ strips and dried at 30°C for 12 hours in air before use. $10\mu\text{L}$ of the as-prepared catalyst ink was drop-casted on the carbon paper and was allowed to dry in ambient atmosphere for 10 minutes before each measurement. Electrodes using the molecular H_2TAPP catalyst were prepared using an identical method.

Bulk electrolysis was performed in an H-type divided cell (120 ml) with a frit separating the two half reactions. A graphite rod electrode (2 mm, radius; 40 mm, length; 515 mm^2 surface area) was as the counter electrode. The electrochemistry cell was purged with high purity argon gas before electrolysis. Quantitative gaseous products were measured online by a gas chromatography instrument (SHIMADZU GC-8A) equipped with a Zebron ZB-1column (30m (length), 0.53mm (I.D), 5 μm (film thickness)) and high-purity argon (99.999%) was used as the carrier gas. Faradaic efficiency (FE) is calculated as follows: $FE = \alpha n F I t \times 100\%$ where $\alpha=2$ for the number of electrons transferred to generate hydrogen and $\alpha=4$ for the number of electrons transferred to generated oxygen; F is the Faradaic constant ($96\,485 \text{ C/mol}$); n is the amount of gas

generated in mols (7.69 μmol for OER in 1.0 M KOH; 2.311 μmol for OER in 1.0 M PBS buffer; 1.8 μmol for HER in 0.5 M H_2SO_4 ; 1.37 μmol for HER in 1.0 M PBS buffer); I (A) is the current and t (s) is the time duration for the bulk electrolysis.

3.3 SYNTHESSES

3.3.1 Synthesis of 5,10,15,20-tetrakis(4-aminophenyl) porphyrin (H_2TAPP)

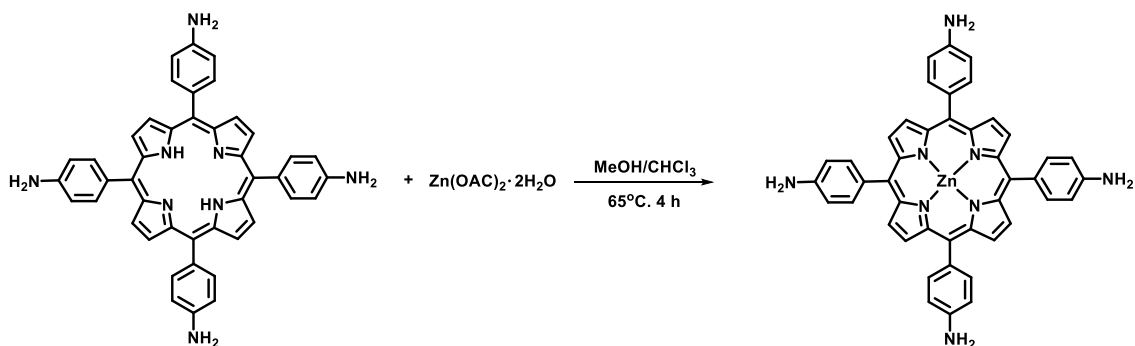


Scheme 5. Synthesis procedure of H_2TAPP .

5,10,15,20-tetrakis(4-aminophenyl) porphyrin (H_2TAPP) was synthesized by a modification of a previously reported procedure, depicted in Scheme 5. A solution of 4-nitrobenzaldehyde (3.0 g, 20 mmol) and acetic anhydride (3.6 mL, 34.8 mmol) in 100 mL propionic acid was heated to 120°C . The mixture of freshly distilled pyrrole (1.4 mL, 20 mmol) was added slowly under N_2 and the reaction was stirred at 140°C for 2 h. Upon cooling, the mixture was refrigerated overnight, and then the resulting precipitate was collected by filtration and washed with MeOH and DI water. The obtained dark solid was dissolved in pyridine (20 mL) and refluxed for 1 h. After cooling down, the system was refrigerated overnight. The nitrated product 5,10,15,20-Tetrakis(4-nitrophenyl) porphyrin, H_2TNPP , was obtained by filtering. It was then washed with a 1:1 mixture of MeOH/acetone and dried under the vacuum yielding 3.7938g (4.76 mmol) of a purple solid. Without any further purification H_2TNPP was dissolved in 480 mL of concentrated hydrochloric acid. A solution of 27 g (130 mmol) $\text{SnCl}_2 \cdot 2\text{H}_2\text{O}$ in 120 mL concentrated hydrochloric acid was added to the porphyrin solution within 20 mins and was vigorously stirred for 3 h. Then the reaction mixture was placed in a hot water bath for 1.5 h. After this, the reaction was cooled down to room temperature, then put in an ice bath. The greenish solid obtained was dispersed in 1000 mL DI water. Concentrated ammonia was added dropwise in order to neutralize the excess acid until the pH of the solution was approximately 7. The purplish solid was washed twice with water, dried under vacuum at room temperature, and then Soxhlet-extracted with

acetone for 24 h. The solvent was removed under reduced pressure to give isolated H₂TAPP as a purple crystal with a yield of 34.3% (1.1105g). UV-vis (λ_{max} nm in THF at 298 K): 429, 521, 570, 663. ¹H NMR (600 MHz, CDCl₃, 25°C): δ -2.72 (s, 2H, pyrrole -NH), 4.03 (s, 8H, amine -NH₂), 8.90 (s, 8H, β -pyrrole), 7.98 (d, 8H, J = 8.1 Hz, 2,6-(4-aminophenyl)), 7.07 (d, 8H, J = 8.1 Hz, 3,5-(4-aminophenyl)).

3.3.2 Synthesis of Zinc(II) 5,10,15,20-tetrakis-(4-aminophenyl) porphyrin Zinc(II) (ZnTAPP)



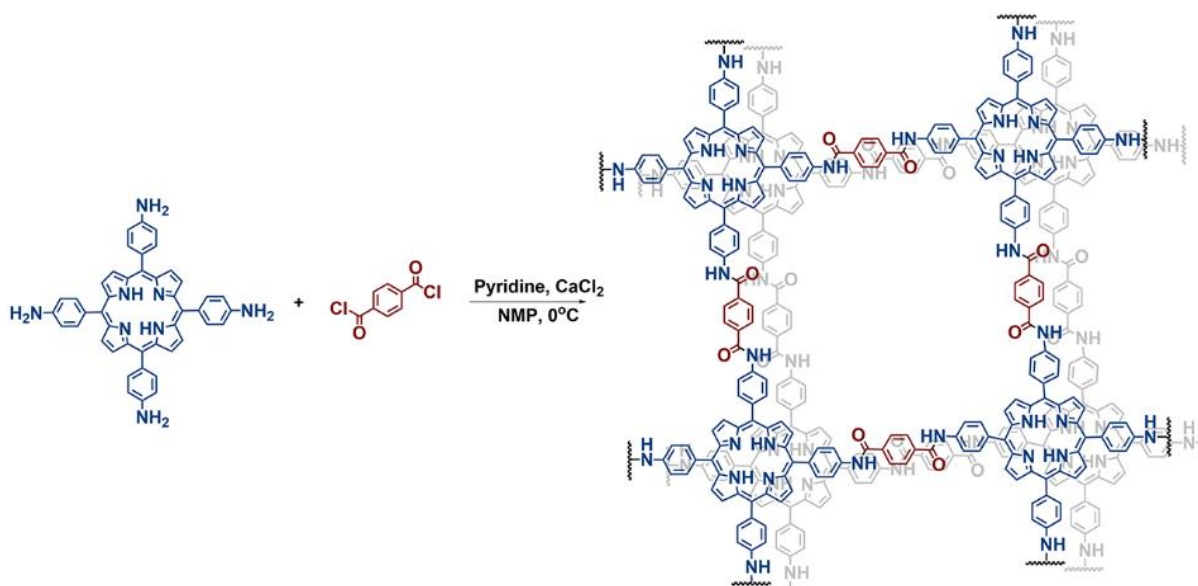
Scheme 6. Synthesis procedure of ZnTAPP.

H₂TAPP (1.0 mmol, 1.86 mg) and Zn(OAc)₂·2H₂O (4.0 mmol, 130 mg) were dissolved in a mixture solvent of methanol and chloroform under N₂ atmosphere. The mixture was refluxed for 4 hours at 65°C. After completion of reaction, the solvent was removed under reduced pressure and desired product was obtained by washing with DI water, followed by recrystallization in ethanol with a yield of 85.4%. UV-vis (λ_{max} nm in THF at 298 K): 438, 561, 606. FT-IR (solid): 3349, 3222, 3227, 2316, 2109, 1591, 1505, 1401, 1276cm⁻¹

3.3.3 Synthesis of Porphvlar

Porphvlar was synthesized through the polymerization of H₂TAPP and terephthaloyl chloride as modified from the synthesise method of the commercial PPTA threads, and is shown in Scheme 7. Initially, N-methyl-2-pyrrolidone (NMP) 0.5 mL was added into 100 mL round bottom flask, and then bubbled N₂ to remove oxygen. When the temperature of the solvent reached 78°C, finely ground dry CaCl₂ was added and dissolved. H₂TAPP (72 mg, 0.106 mmol) and pyridine (0.025 mL) was added to the system with stirring. When H₂TAPP was completely dissolved, the temperature was lowered with an ice-bath. The polymerization was started by adding terephthaloyl chloride (88 mg, 0.425 mmol). After 1 h, DI water was added into the reaction and the resulting mixture was quickly filtered with a Buchner funnel and hydrophilic disks. The residue

was washed with ethanol and water. The powder material was ground and kept immersed in ethanol overnight. The suspension was filtered again and dried under vacuum to yield a greenish powder (yield: 48.7 mg, 37.7%). UV-vis (λ_{max} nm in THF at 298 K): 425, 518, 556, 654. FT-IR (solid): 3000, 2960, 2378, 2126, 1681, 1587 cm^{-1} .



Scheme 7. Synthesis procedure of Porphvlar

3.3.4 Synthesis of Zn-Porphvlar

Zn-Porphvlar was synthesized through the polymerization of ZnTAPP and terephthaloyl chloride with same method used in the Porphvlar synthesis. UV-vis (λ_{max} nm in THF at 298 K): 422, 514, 544, 601. FT-IR (solid): 2985, 2825, 2670, 2560, 2109, 2077, 1986, 1679, 1430, 1273 cm^{-1}

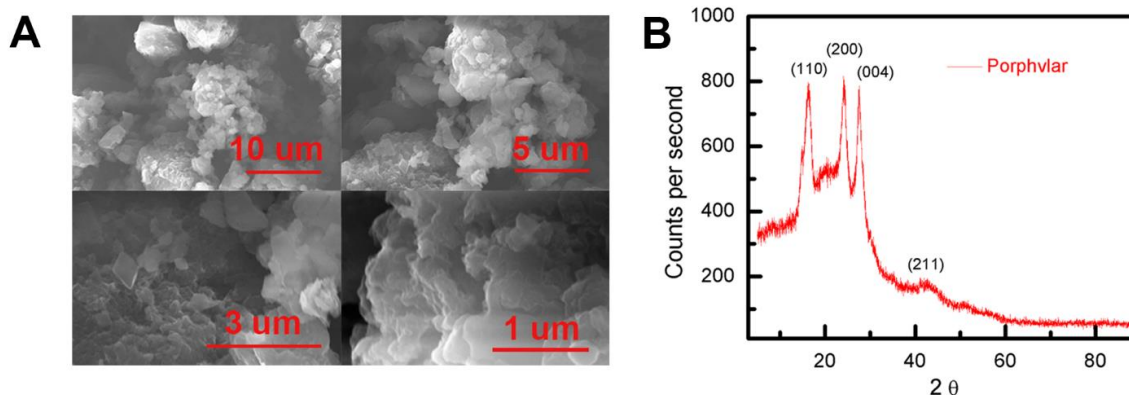


Figure 11. Scanning electron microscopy (SEM) of Porphvlar in various scales and the *p*-XRD peaks.

3.4 CHARACTERIZATIONS

Scanning electron microscopy (SEM) images were obtained to evaluate the morphology of the synthesized Porphvlar polymer in different magnifications. Figure 11 shows that the Porphvlar powder exhibits a flake-like morphology. The flakes are stacked in layers of a couple of nanometers in thickness. This is in contrast to the rod-like topology of PPTA threads.⁶³ Both Energy-dispersive X-ray spectroscopy (EDX) (Figure 12) and high-resolution XPS spectra (Figure 13) show that only C, N, and O elements exist throughout the Porphvlar structure without the presence of any metal atoms that could have been incorporated through the synthetic processes. Inductively coupled plasma - optical emission spectrometry (ICP-OES) was performed to more exhaustively study the elemental composition of the samples. A trace amount of Sn can be detected

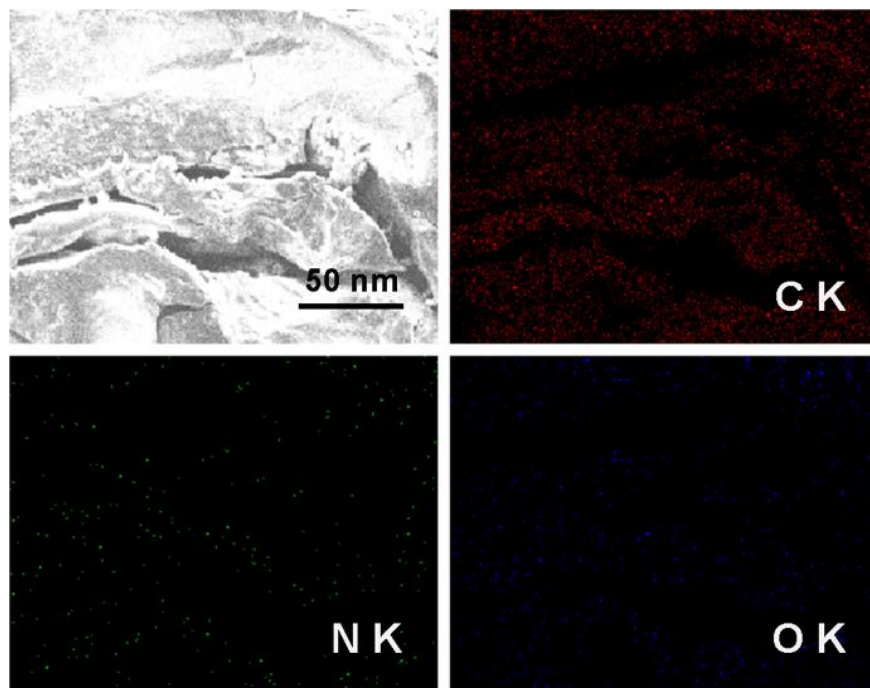


Figure 12. Energy-dispersive X-ray spectroscopy (EDX) mapping of Porphvlar.

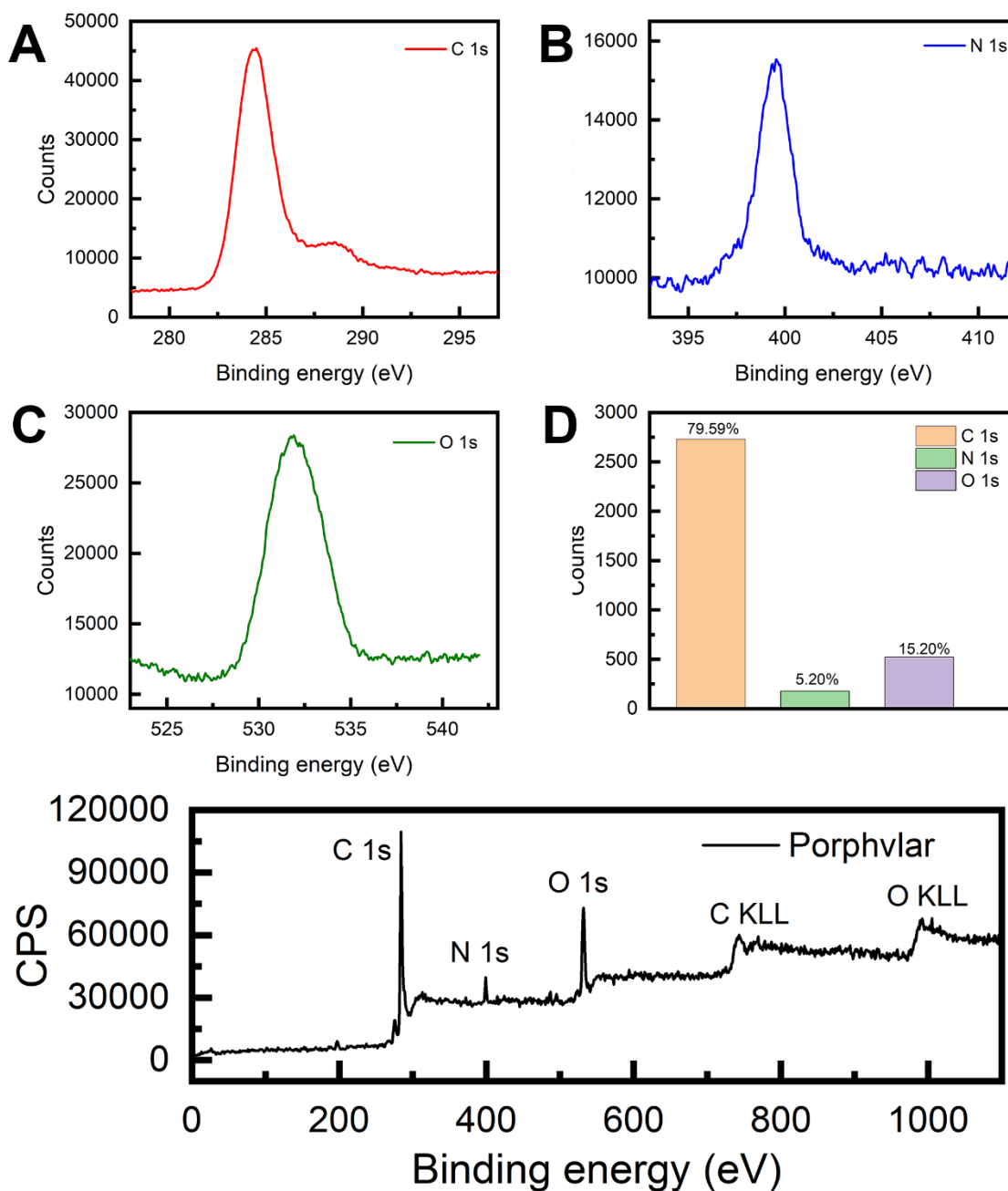


Figure 13. High resolution XPS spectra of Porphvlar sample (A-C); (D). Atomic ratio of C, N, and O of the Porphvlar sample; (E) Full XPS survey.

at the parts per million level (328 ppm) in Porphvlar samples. SnO is presumed to be the contaminant that is likely generated during the syntheses of the Porphvlar precursor, H₂TAPP.

The powder X-ray diffraction (*p*-XRD) pattern in Figure 12 B shows that the sample is microcrystalline. The *p*-XRD pattern of Porphvlar closely resembles the crystalline pattern of commercial PPTA. The diffraction peaks observed at $2\theta = 24.1^\circ$, 27.5° , 28.4° and 42.4° correspond

to the (1 1 0), (2 0 0), (0 0 4) and (2 1 1) planes, respectively, which are also present in PPTA fibers.⁶⁴ The broad peak centered at around $2\theta = 20^\circ$ is attributed to π - π stacking between the 2D layers, where the porphyrin units form an AA type eclipsed stacking.⁶⁵

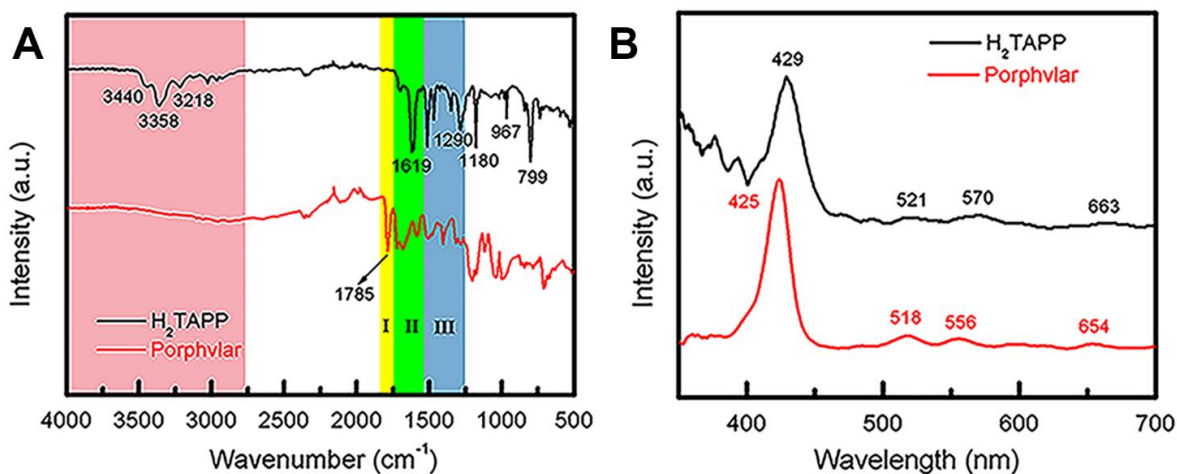


Figure 14. Spectroscopic characterization of Porphvlar. (A) FT-IR spectra of Porphvlar and molecular porphyrin (H_2TAPP). (B) Comparison UV-vis spectra of Porphvlar and H_2TAPP .

The FT-IR and UV-vis spectra of Porphvlar were compared to those obtained from the molecular porphyrin unit, H_2TAPP . Figure 14 A shows the FT-IR spectra for both the porphyrin unit (top) and Porphvlar (bottom) materials. Porphvlar exhibits a band at 1785 cm^{-1} assigned to the amide I (carbonyl stretch, yellow region), the amide II band (N–H bend) appears around 1500 – 1700 cm^{-1} (green region), and the amide III band is observed in the blue region. These bands indicate the formation of the amide group in the Porphvlar structure and are missing in the H_2TAPP spectrum. In addition, the γ -(N–H) pyrrole out-of-plane stretch is observed at 799 cm^{-1} in H_2TAPP and shifts to $\sim 1000\text{ cm}^{-1}$ in Porphvlar. Two primary amines ν -(N–H) stretching bands at 3440 and 3356 cm^{-1} and one sp^2 ν -(C–H) stretching peak (3218 cm^{-1}) are visible in H_2TAPP , and those appear as a broad band around 3000 cm^{-1} in Porphvlar (pink region) due to hydrogen bonding between the polymer layers. Figure 14 B shows the UV-vis spectra of H_2TAPP and Porphvlar. H_2TAPP has the indicative spectrum of a free-base porphyrin with a Soret band at 429 nm along with its corresponding Q-bands between 521 to 663 nm . Porphvlar shares a similar spectrum where the Soret and Q bands are blue-shifted by about 4 nm . This indicates that the porphyrin unit is incorporated into the Porphvlar network.

3.5 RESULTS AND DISCUSSION

The OER electrocatalytic activity evaluation of the resulting Porphvlar was performed in 1.0 M KOH aqueous solution and 1.0 M phosphate buffer saline solution (PBS) with carbon paper as the conductive support electrode. The carbon black/carbon paper blank electrode has a negligible current increase. In KOH solution, Porphvlar exhibits a current increase at 1.63 V ($\eta_1 = 400$ mV) where a sharp increase is observed. The molecular porphyrin, H₂TAPP, has a similar onset potential where the catalytic current is observed but with a lower current response (Fig. 2A, blue line). These onset overpotentials are lower than those from reported metallated porphyrin

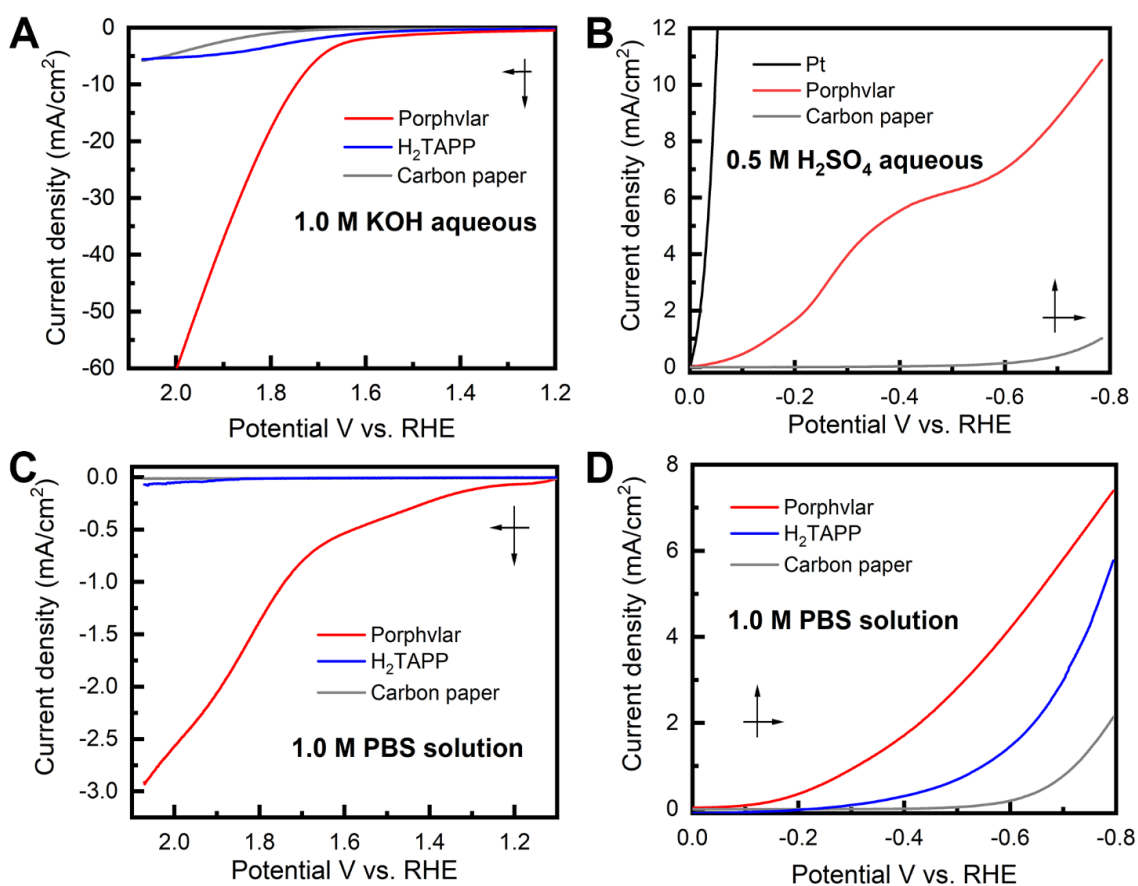


Figure 15. Polarization curves of molecular porphyrin (H₂TAPP) (blue), Porphvlar (red) and blank carbon paper electrode under different conditions. (A) Oxidation in 1.0 M KOH aqueous solution; (B) Reduction in 0.5 M H₂SO₄ aqueous solution, (C) Oxidation in 1.0 M PBS buffer solution; (D) Reduction in 1.0 M PBS buffer solution, scan rate: 5 mV/s.

composite materials (rGO/(Ni²⁺/THPP/Co²⁺/THPP)_n: 1.49 V vs RHE)⁶⁶ and other metal-based OER catalysts (FeNi LDH/GO: 1.439 V vs. RHE)⁴² and metal-free carbon/graphene-based

multifunctional electrocatalysts (2D-N, S doped graphitic sheets: 1.49 V vs. RHE)⁶⁸ in heterogeneous systems.

The current response of Porphvlar reaches a current density of 10 mA/cm² at 1.75 V (η_{10} = 520 mV) in basic electrolyte, while the molecular porphyrin plateaus at 5 mA/cm² (Figure 15 A). The electrocatalytic OER performance for Porphvlar was also investigated in neutral PBS. As depicted in Figure 15 C, the current density of Porphvlar increases slowly at 1.31 V vs. RHE until 1.63 V vs. RHE. Porphvlar requires an overpotential of 520 mV to achieve a current density of 1 mA/cm², however, the molecular H₂TAPP shows negligible current increase under the same conditions. An electrode was prepared with commercial PPTA thread and was used as a working electrode, the low current density show PPTA is inactive for both HER and OER. Therefore, the current density corresponds to catalytic electrochemical activity when porphyrin units are incorporated into PPTA networks. The generated gas obtained from the 60 h Porphvlar bulk electrolysis was collected in a gas-tight H-type cell and was confirmed to be O₂ by gas chromatography with 92.7% Faradaic efficiency in 1.0 M KOH and 84.5% Faradaic efficiency in 1.0 M PBS solution.

Figure 15 B shows the HER electrocatalytic activity of Porphvlar in a 0.5 M H₂SO₄ aqueous solution. The Pt electrode is shown as a benchmark for HER. Porphvlar has an onset potential of 36 mV vs. RHE and reaches a current density of 1 mA/cm² at 144mV. H₂TAPP does not perform HER in 0.5 M H₂SO₄ aqueous solution due to the protonation reaction in the nitrogen core. A pre-wave was observed at around -0.4 V vs. RHE, which is a phenomenon of adsorption of protons that accumulate favorably on the modified electrode surface. The competition between the adsorption stage and the cathodic reduction is significant but consecutively since the pre-wave disappears when precludes the mass transfer factor. The collected reduction product was confirmed to be hydrogen gas by gas chromatography with a Faradaic efficiency of 98% in acidic electrolyte and 99.55% in PBS buffer.

Additionally, the porphyrin unit was metallated with zinc using standard synthetic procedures. Figure 16 shows Zn-Porphvlar exhibits a considerably lower current response towards HER and OER with respect to the corresponding metal-free materials. This suggests that the catalytic center is located at the four-nitrogen core in the free-base porphyrin units. Thus, incorporating a redox inactive metal ion such as Zn can effectively shut down the activity of Porphvlar towards catalyzing water splitting electrochemically.

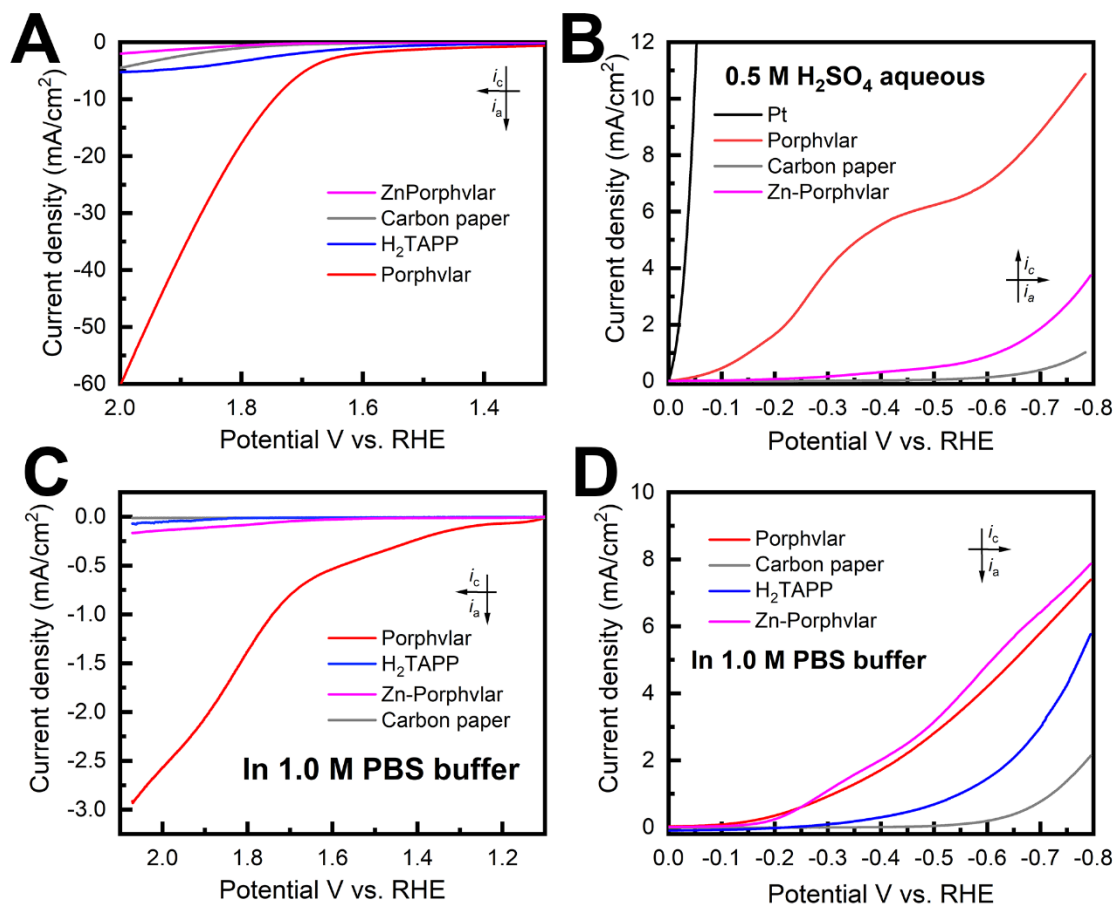


Figure 16. Comparison linear sweep voltammetry of Zn-Porphvlar with the metal-free Porphvlar in different electrolytes under the corresponding oxidation and reductions. Scan rate: 5 mV/s.

The kinetic properties of Porphvlar and H₂TAPP under oxidation and reduction conditions within different electrolytes were characterized by electrochemical impedance spectroscopy (EIS) in order to study the interface charge transport process. The Nyquist plots of Porphvlar and H₂TAPP, obtained by measuring the parametric response of the

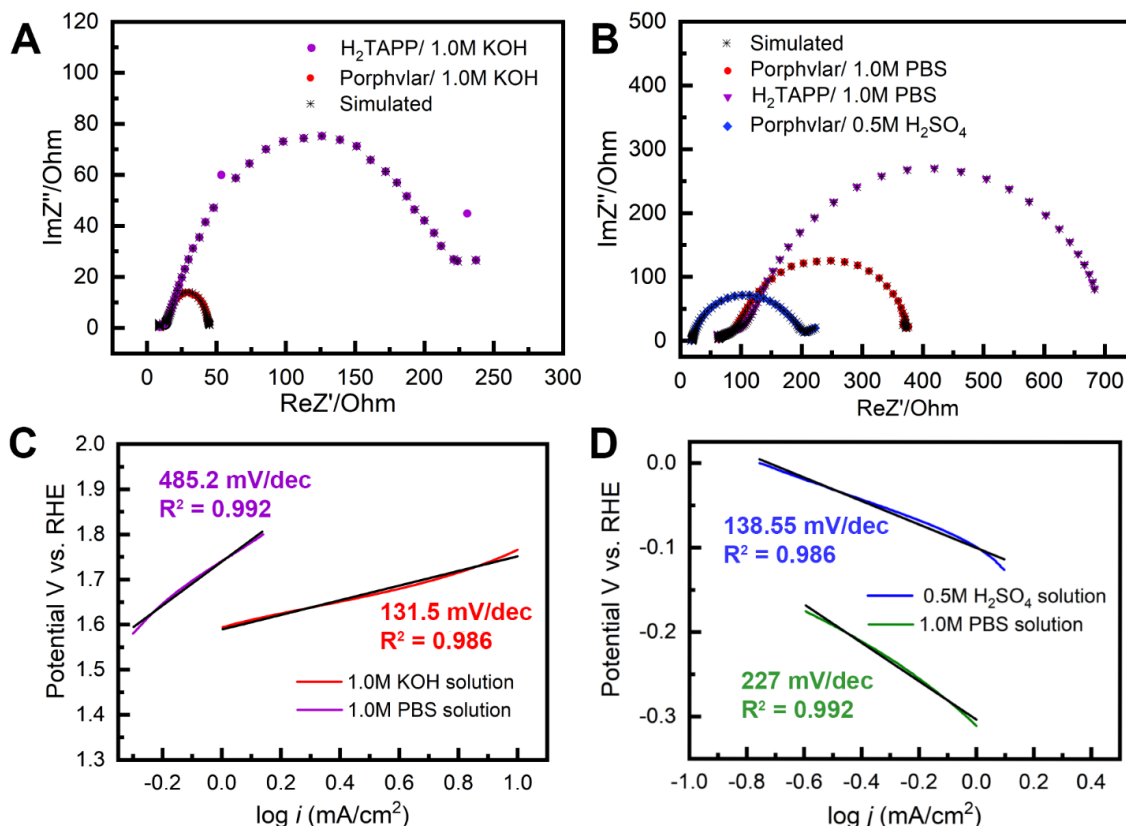


Figure 17. Electrochemical impedance spectroscopy of Porphvlar (red) and H₂TAPP (purple) operated at 250 mV overpotential: (A) in 1.0 M KOH aqueous solution (B) in 1.0 M PBS buffer solution and 0.5 M H₂SO₄ aqueous solution (blue), respectively; Tafel plots of Porphvlar constructed by polarization curves: (C) in 1.0 M KOH aqueous solution (red) and 1.0 M PBS buffer (purple); (D) 1.0 M PBS buffer solution (green) and 0.5 M H₂SO₄ aqueous solution (blue).

imaginary part vs. the real part of the impedance, are shown in Figure 17 A and B. The diameter of the semicircle relates to the electron transfer process from the electrode surface into the electrolyte solution since it arises from the parallel combination of Faradaic charge transfer resistance and non-Faradaic double-layer capacitance. Therefore, the smaller the semicircle the less the charge transfer resistance.^{69,70} It can be seen that the semicircle in the high-frequency range of the Nyquist plot of Porphvlar has a smaller diameter than that of the molecular porphyrin unit under both oxidation and reduction conditions. This suggests that the Porphvlar network favors charge transfer during water splitting. Furthermore, the increased electron transfer from the modified electrode to the electrolyte enhances the catalytic activity towards both HER and OER.

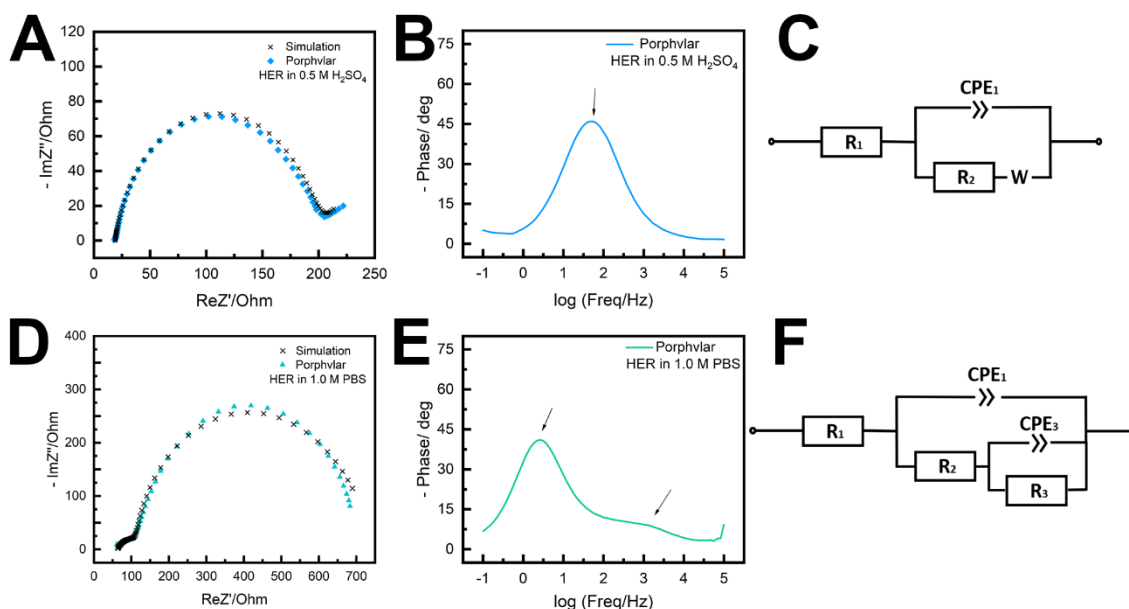


Figure 18. Electrochemical impedance spectroscopy (EIS) of hydrogen evolution reaction catalyzed by Porphvlar on carbon paper electrode: (A) Nyquist plot of HER in 0.5 M H_2SO_4 aqueous solution with simulation fit. (B) Bode plot of HER in 0.5 M H_2SO_4 aqueous solution. (C) The electrical equivalent circuit (EEC) used to simulate the impedance spectra fit in 0.5 M H_2SO_4 aqueous solution. (D) Nyquist plot of HER in 1.0 M PBS solution with simulation fit. (E) Bode plot of HER in 1.0 M PBS solution. (F) The electrical equivalent circuit (EEC) used to simulate the impedance spectra fit in 1.0 M PBS solution.

EIS analyses were performed to investigate the Porphvlar cathode/anode interphase during the water splitting reaction and modeled with the appropriate equivalent circuit (Figure 18 and 19). Experimental results fit to the Randles circuit and fitted parameters are shown in Table 1. Constant phase elements (CPEs) are used for the non-ideal capacitance from the non-homogeneous electrode surface with the ideality factor n . R_1 is the series resistance for the electrolyte and the electrode materials. The simulation shows that for HER the electrochemical processes are different when the reaction happens in acidic or neutral conditions (Figure 18C and 18F). For the HER in sulfuric acid, the parallel branch ($\text{CPE}_1/(R_2+W)$) indicates that the interphase between the electrode and the electrolyte is where electron transfer occurs, and R_2 represents the charge transfer resistance (R_{ct}). In PBS buffer, HER requires two steps: the first branch describes the contact between the electrode and Porphvlar; the second branch (CPE_3/R_3) is responsible for the double-layer impedance and the charge Porphvlar. For OER, Porphvlar has a similar two-step catalytic

process (Figure 19C and 19F) in both basic conditions and PBS buffer. An extra diffusion impedance element (Warburg diffusion) is included in the simulation in a neutral solution since the reaction is no longer controlled by kinetics due to the lack of readily available hydroxide ions. In these conditions, the reaction rate depends on the diffusion of buffering ions. As result, buffered ions penetrate the diffusion layer creating a finite thickness Warburg element.

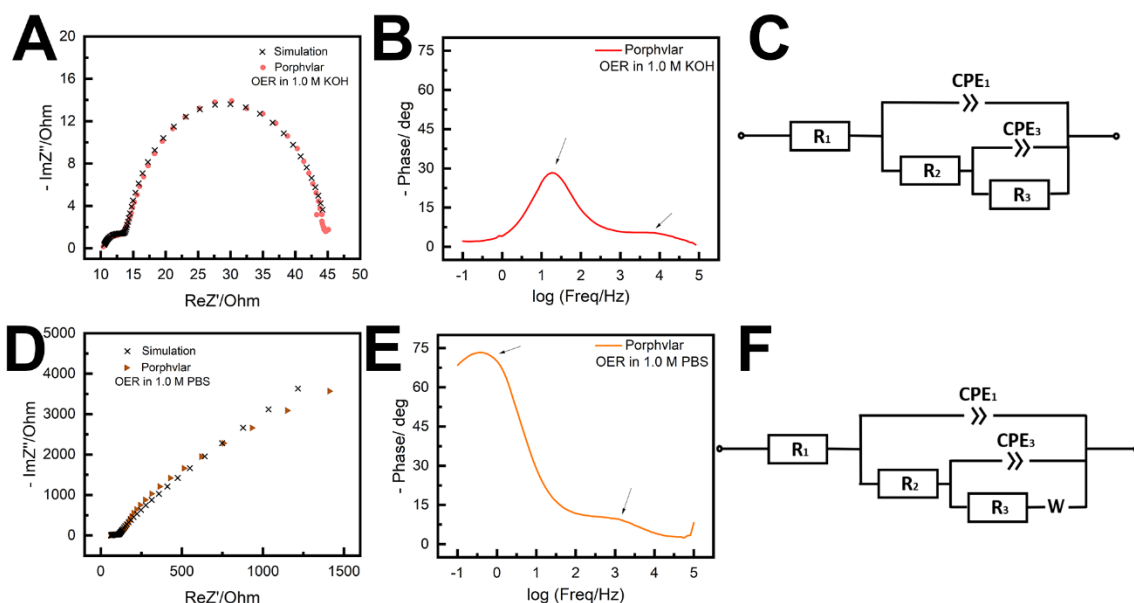


Figure 19. Electrochemical impedance spectroscopy (EIS) of oxygen evolution reaction catalyzed by Porphylar on carbon paper electrode: (A) Nyquist plot of OER in 1.0 M KOH aqueous solution with simulation fit. (B) Bode plot of OER in 1.0 M KOH aqueous solution. (C) The electrical equivalent circuit (EEC) used to simulate the impedance spectra fit in 1.0 M KOH aqueous solution. (D) Nyquist plot of OER in 1.0 M PBS solution with simulation fit. (E) Bode plot of OER in 1.0 M PBS solution. (F) The electrical equivalent circuit (EEC) used to simulate the impedance spectra fit in 1.0 M PBS solution.

TABLE 1. Parameters for Equivalent Circuits for the water splitting reaction reported in this work.

	Porphvlar				H ₂ TAPP		
	HER		OER		HER	OER	
Electrolyte	0.5 M H ₂ SO ₄	1.0 M PBS	1.0 M KOH	1.0 M PBS	1.0 M PBS	1.0 M KOH	1.0 M PBS
R1 (Ohm)	18.84	62.60	10.34	60.73	61.99	8.919	63.15
CPE1 (F.s^{a-1})	N/A	0.1611× 10 ⁻³	0.2996× 10 ⁻³	0.1549× 10 ⁻³	58.29× 10 ⁻³	0.1591× 10 ⁻³	58.33× 10 ⁻⁶
n1	N/A	0.6385	0.6902	0.6349	0.6688	0.6888	0.6845
CPE2/3 (F.s^{a-1})	0.1267× 10 ⁻³	0.203× 10 ⁻³	0.506× 10 ⁻³	0.1549× 10 ⁻³	0.2321	0.67× 10 ⁻³	0.1193× 10 ⁻³
n2/3	0.8612	0.9557	0.9495	0.9365	0.0965	0.8398	0.8583
R2 (Ohm)	180.5	67.56	4.415	69.06	1098	6.098	43.08
R3 (Ohm)	N/A	622.8	30.67	31.66	303.0	206.6	477.5
s2 (Ohm.s^{1/2})	11.99	N/A	N/A	N/A	22.64	N/A	N/A
χ²	0.03369	0.03336	9.155× 10 ⁻³	0.07571	0.0306	0.2432	0.08639
χ/√N	0.0215	0.0225	0.0124	0.0322	0.0214	0.0598	0.0243

To evaluate the kinetics during the electrolysis process, Tafel plots were constructed from polarization curves (Figure 17 C and D). The linear portions of the Tafel plots were fit to the Tafel equation: $\eta = a + b \log(j)$, where η is the overpotential, j is the current density, and b is the Tafel slope. The calculated Tafel slope for Porphvlar (131.5 mV/dec) in a 1.0 M KOH solution is comparable to that of the benchmark OER electrocatalyst IrO₂ (83 mV/dec),⁷¹ suggesting fast reaction kinetics and high OER activity. In 0.5 M H₂SO₄ solution, Porphvlar has an HER Tafel slope of 138.55 mV/dec, which also indicates efficient kinetics. The general HER mechanism in metal surfaces has been extensively

studied, and three mechanisms have been proposed for the different Tafel slopes: Volmer (120 mV/dec), Heyrovsky (40 mV/dec) and Tafel (30 mV/dec).⁷² The Porphvlar HER Tafel slopes (in neutral and acidic conditions) suggest a Volmer-Heyrovsky mechanism via water reduction ($H_2O + e^- = H_{ads} + OH^-$ and $H_2O + e^- + H_{ads} = H_2 + OH^-$).⁷³ The Tafel slopes are larger for HER and OER when using PBS as an electrolyte, these slow kinetics might be due to the low ion concentration and pH in the reaction.

The long-term stability of Porphvlar in different electrolytes under both oxidation and reduction conditions, was studied with bulk electrolysis for 60 hours. Figure 20 shows that Porphvlar exhibits constant and stable anodic and cathodic currents during OER and HER electrocatalysis, respectively, during this timeframe. Energy-dispersive X-ray spectroscopy mapping shows no metal contamination or deposition on the Porphvlar network after the electrolysis in basic and acidic conditions mentioned. The FT-IR and UV-vis spectra of the Porphvlar material/electrode and the corresponding electrolyte before and after the bulk electrolysis show unchanged characteristic peaks. The durability of Porphvlar can be attributed to the stability of the conjugated porphyrin networks and the hydrogen bonding within its layers that result in a unique catalytic material for HER and OER.

3.6 CONCLUSIONS

In summary, an efficient and stable metal-free electrocatalyst for HER and OER has been developed. This bifunctional material was constructed through the condensation of (4-

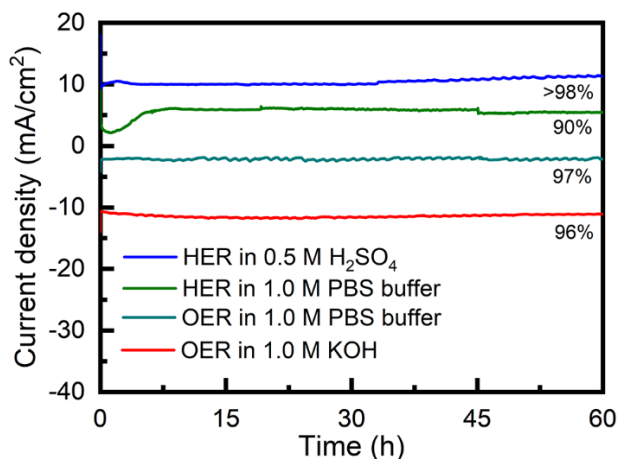


Figure 20. Time dependence of the current density for as-synthesized Porphvlar at static potential; blue: HER in 0.5 M H₂SO₄; green: in 1.0 M PBS buffer; teal: OER in 1.0 M PBS buffer; red: OER in 1.0 M KOH.

aminophenyl) porphyrin (H₂TAPP) into PPTA networks. The HER and OER catalytic performances are higher than those of other metal-free materials and comparable or better than several traditional metallic electrocatalysts. The catalytic ability of Porphvlar which occurs at the molecular porphyrin nodes is further enhanced by the 2D network arrangement of the hydrogen-bonded PPTA networks. This material provides a novel approach to the design of metal-free electrocatalysts and takes advantage of the structural interactions within a 2D network to yield high electrochemical performance, conductivity, and durability.

Chapter 4

Metalloporphyrin organic polymers as effective and stable electrocatalysts for oxygen evolution reaction and oxygen reduction reaction

4.1 INTRODUCTION

The new emerging energy conversion and storage system such as rechargeable metal-air batteries, fuel cell and water electrolyzers has been attracting considerable attention due to the emphasis on sustainable production of green and renewable energy.^{74,75} The key reaction on the electrode, namely oxygen evolution reaction (OER) is generally the major bottleneck for the development of more applicable device since OER is significant in determining the reaction rate and the efficiency of water splitting.^{76,77} Today, the state-of-the-art electrocatalysts for HER and OER are still precious metal based materials (e.g. Pt and IrO_x), the high price and scarcity hampered their feasible commercialization. This has led to more research being conducted in an effort to look for efficient alternate electrocatalysts for these two processes that are able to achieve the overpotential close to the thermodynamic limits and increase the reaction rate. Recent research has been committed to the design of active nonprecious metal based metal oxides, nitrides, carbides, and chalcogenides as electrocatalysts for generating oxygen.⁷⁸⁻⁸² Integrating redox active molecular units contain earth-abundant metals, such as cobalt, nickel, iron, and manganese, into networks has shown enhanced catalytic active and stability towards water splitting.⁸³⁻⁹¹ These efforts have improved the fundamental understanding of catalysis process and guided the rational design of efficient electrocatalysts. Despite all the progress has been made, it still remains a great challenge to achieve a balance between catalyst performance, cost, and stability before the energy conversion system can be implemented on large scale.

Porphyrin based materials, such as metal-organic frameworks (MOFs),⁹²⁻⁹⁴ covalent organic frameworks (COFs),⁹⁵⁻⁹⁷ amorphous polymers^{54,98,99} and composites,^{92,100} have been widely used in energy-related conversion processes, including oxygen reduction reaction (ORR), oxygen evolution reaction (OER) and CO₂ reduction reaction. Porphyrins are a group of nitrogen-rich organic compounds with extended 18 π -conjugated structure and can undergo multi-electron and proton transfer process.⁴⁴ Introducing different functional groups on porphyrin periphery can tune the electronic structure, therefore regulate its physical and chemical properties towards

catalyzing HER and OER.^{39,42,101,102} Lots of research focus on the substituent effect on porphyrin when is using as water splitting catalysts.¹⁰³ Our recent research revealed the superior catalytic activity of a free-base porphyrin bearing electron-withdrawing groups on the *meso*- positions for electrochemically hydrogen generation reaction.⁴³ Transition metal based metalloporphyrins inspired from hemoglobin have been frequently studied as (photo)electrocatalysts for water electrolysis.^{48,50,57,104,105} Deprotonated porphyrin units have a strong ability to coordinated high valence transition metal or metal ions by forming a rigid four-coordinated environments, which frequently find to be active for O-O cleavage and formation.^{106,107} Transition metals such as Co, Ni, Cu and Fe are constantly chosen to be active site especially in oxygen reduction/evolution reaction.^{108,109} This is mainly due to their efficient electron transfer and are able to form metal-oxo adducts that can facilitate the four electron reduction/oxidation with efficient selectivity. However, Fe porphyrins in general showed moderate electrocatalytic OER activity.¹¹⁰⁻¹¹² Considering that water oxidation is the reverse reaction of oxygen reduction, it is possible to improve the OER activity of Fe-porphyrins if the structure is properly designed. In addition, systematical heterogenization of metalloporphyrin moieties in polymer/framework will help facilitated their recyclability, and more importantly, address the issues such as low mass transport efficiency, poor stability and low density of catalytic active sites.^{54,100,113} In addition to it, linker units with different electronegativity could affect the electron transfer efficiency when combine with various metal center within porphyrin units, as a result, the OER efficiency can be largely enhanced by tuning the electronic structure.¹¹⁴

In this work, we report the synthesis and characterizations of an easily synthesized porphyrin organic polymer from one-step polymerization, and their metallated versions as efficient electrocatalysts for OER. The introduction of Co and Fe in the porphyrin unit can serve as active sites, which resulting in fast reaction rate and significantly improved electrocatalytic performance. Furthermore, the fluorinated linkage in metallated porphyrin polymers gave rise to an enhanced OER overpotential and kinetics. All materials were characterized using standard spectroscopic and microscopic techniques. We also report herein the evaluation of the electrocatalytic OER performances of all polymer materials through electrochemical studies.

4.2 MATERIALS AND METHODS

All chemicals used were purchased from commercially available sources. Pyrrole (C₄H₅N), terephthalaldehyde (C₈H₆O₂), FeCl₂·4H₂O and Nafion[®] 117 (5% w/w in H₂O and 1-propanol) were purchased from Sigma Aldrich. Co(OAC)₂·4H₂O was purchased from TCI chemicals. Carbon black (Vulcan XC-72) was obtained from FuelCell Store. All solvents used and potassium hydroxide (KOH) pellets (>85%) were from Fisher Scientific. Pyrrole was freshly distilled prior to use while all other chemicals were used as received.

Fourier-transform infrared (FT-IR) spectra were recorded using an Agilent Cary 630 FT-IR spectrometer equipped with an attenuated total reflectance (ATR) accessory. X-ray power diffraction (*p*-XRD) patterns were obtained using a Bruker D8 Discovery X-ray diffractometer. Scanning electron microscope (SEM) measurements along with elemental mapping and energy dispersive X-ray analysis (EDX) were recorded on a Hitachi S-4800 instrument equipped with an EDX microanalysis system. X-ray photoelectron spectroscopy (XPS) spectra were obtained by a Physical Electronics PHI 5000 VersaProbe with an Al K α source. All spectra were calibrated to the adventitious carbon 1s peak at 284.8 eV and fitted using a Shirley background.

A catalyst ink was prepared by dispersing 2.5 mg of carbon black and 5 mg of catalyst in 1.02 mL isopropanol and 4.08 μ L Nafion[®] solution. The resulting solution was sonicated for 30 minutes for form a homogeneous ink. A glassy carbon disk was cleaned and polished to a mirror finish and was mounted on a rotating disk electrode (RDE) apparatus. The working electrode consisted of 10 μ L of the prepared catalyst ink dropcasted on a glassy carbon disk which was rotated at 600 rpm for 5 minutes until the ink was dry. The glassy carbon disk electrode (0.196 cm²) had a final catalyst loading of 0.25 mg/cm².

Electrochemical measurements were conducted in a three-electrode RDE configuration using an Ag/AgCl reference electrode, a graphite rod counter electrode, and the modified glassy carbon disk as the working electrode. All studies were performed in a 0.1 M KOH aqueous solution saturated with ultra-high pure O₂ with the working electrode constantly rotated at 1600 rpm at a scan rate of 10 mV/s. Ohmic correction was performed after each electrochemical measurement and the resistance of the electrolyte solution in the cell was determined at 100 kHz. The RHE (reversible hydrogen electrode) potential was determined by measuring the open circuit potential of a clean Pt electrode in the electrolyte solution after testing the electrodes. Faradaic efficiency was determined by quantitative oxygen gas determination from oxygen bubbles evolved from the

working electrode that were captured in an inverted graduated cylinder containing 0.1 M KOH electrolyte.

4.3 CHARACTERIZATIONS

FT-IR spectra and X-ray powder (*p*-XRD) diffractograms of (Por)OP, Co(Por)OP, and Fe(Por)OP are in agreement with previous studies.¹¹⁵ Notably, all FT-IR spectra do not show the characteristic C=O vibration band of the aldehyde between 1720 and 1740 cm^{-1} , which is expected to diminish after successful polymerization; therefore, indicating that all samples are polymeric systems. The band observed at around 1001 cm^{-1} for Co(Por)OP, and Fe(Por)OP is assigned to the characteristic metal-nitrogen vibration suggesting successful metallation. The peaks observed at around 1298 cm^{-1} in the fluorinated samples are attributed to the C–F stretch (Figure 21). In addition, all *p*-XRD diffractograms of the samples show no strong diffraction peaks, which reveal the amorphous nature of all the synthesized materials (Figure 22).

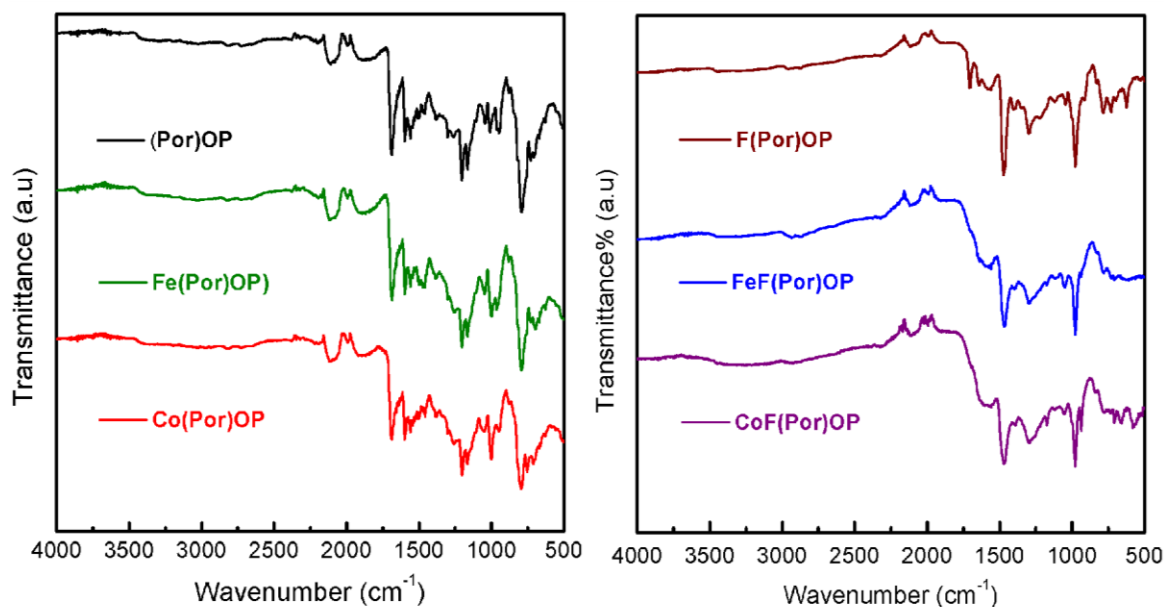


Figure 21. FT-IR spectra of (Por)OP, F(Por)OP, Co(Por)OP, CoF(Por)OP, Fe(Por)OP and FeF(Por)OP.

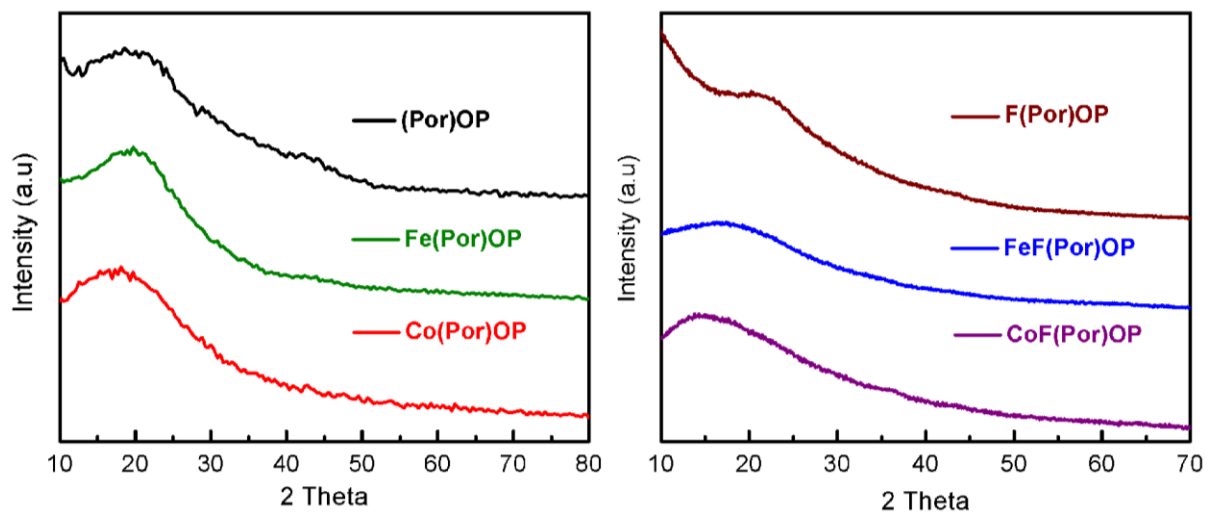


Figure 22. *p*-XRD of (Por)OP, F(Por)OP, Co(Por)OP, CoF(Por)OP, Fe(Por)OP and FeF(Por)OP.

SEM micrographs (Figure 23) show that all the synthesized materials present morphologies of uniform spherical particles with dimensions at the micrometer scale. After metalation, the morphologies of the polymers retained the spherical shape. The metal content was determined by inductively coupled plasma mass spectrometry (ICP-MS). As a result, Co(Por)OP and CoF(Por)OP contains 17.13% and 54.12% cobalt, respectively, while Fe(Por)OP and FeF(Por)OP respectively show iron content of 4.19% and 34.64%. In addition, XPS survey (Figure 24), EDX

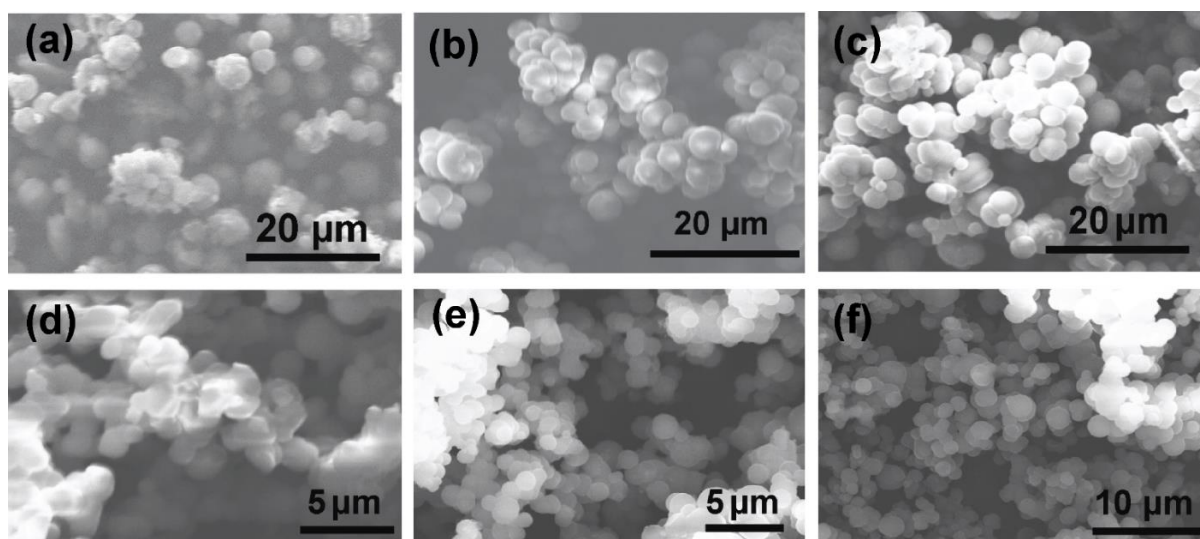


Figure 23. SEM images of (a) (Por)OP, (b) Co(Por)OP, (c) Fe(Por)OP, (d) F(Por)OP, (e) CoF(Por)OP and (f) FeF(Por)OP.

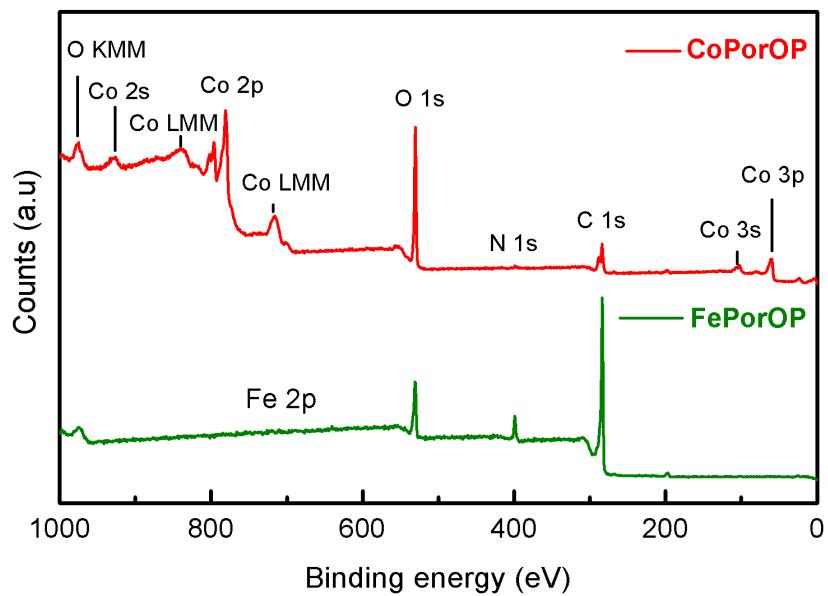


Figure 24. representative XPS survey (**CoPorOP** and **FePorOP**).

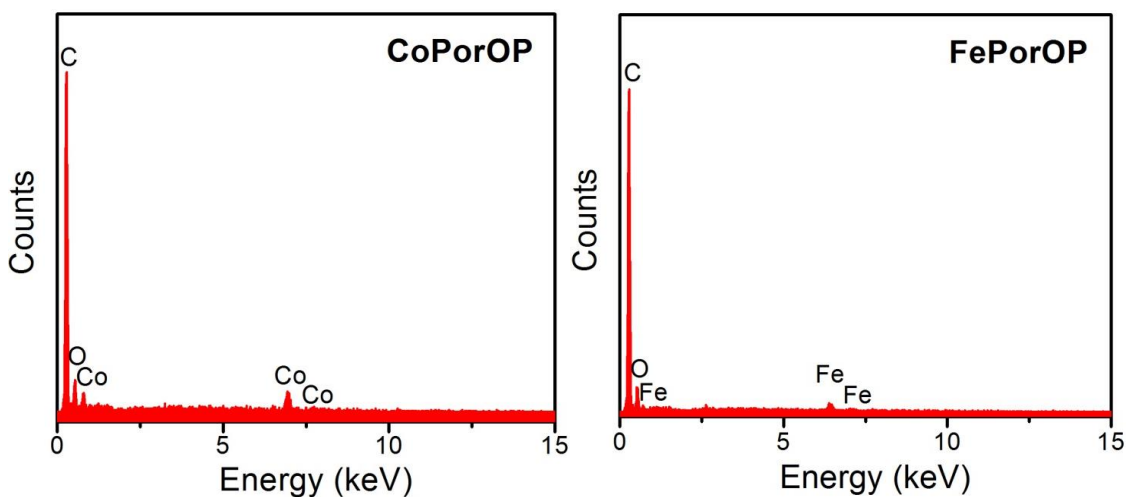


Figure 25. representative EDX spectrum of synthesized porphyrin organic polymers: **CoPorOP** and **FePorOP**

analysis (Figure 25), elemental mapping (Figure 26) and UV-vis spectra (Figure 27) all showed the success metalation of Co and Fe metal inside the porphyrin core of the porphyrin organic polymers.

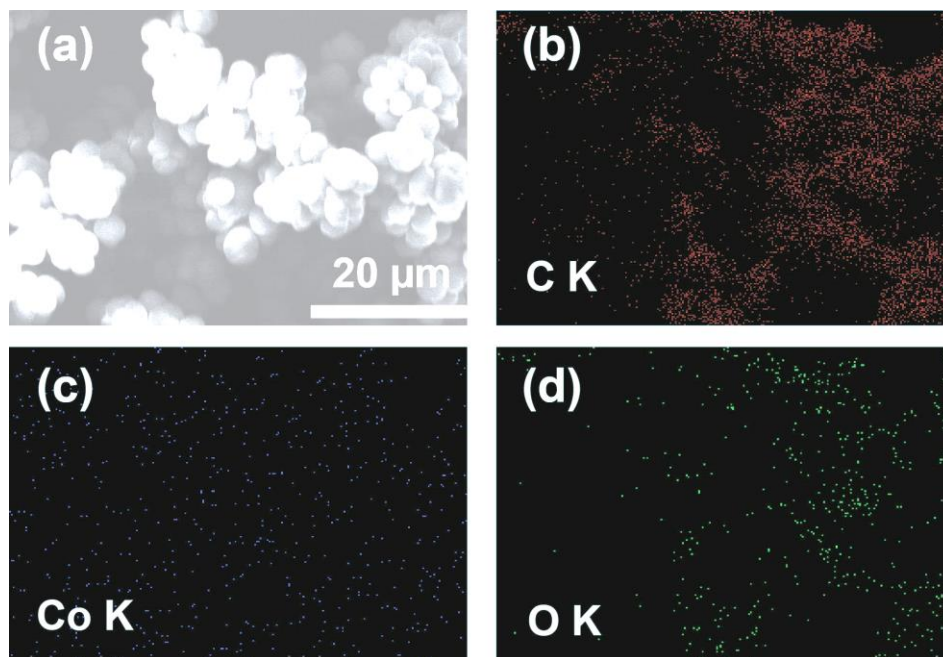
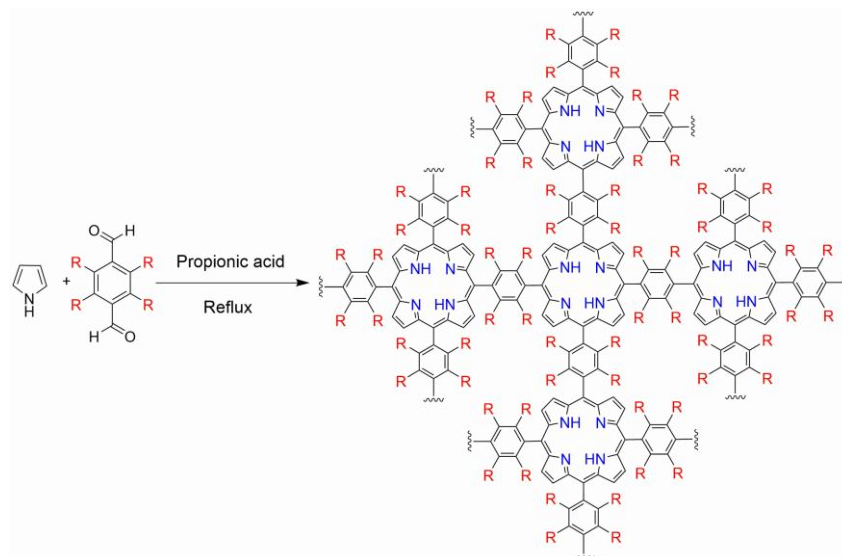


Figure 26. representative elemental mapping spectrum of synthesized porphyrin organic polymers (**CoPorOP**)

4.4 Syntheses

4.4.1 Synthesis of porphyrin organic polymer [(Por)OP and F(Por)P]:⁵⁴



Scheme 8. Synthetic scheme of porphyrin organic polymers.(R = H or F)

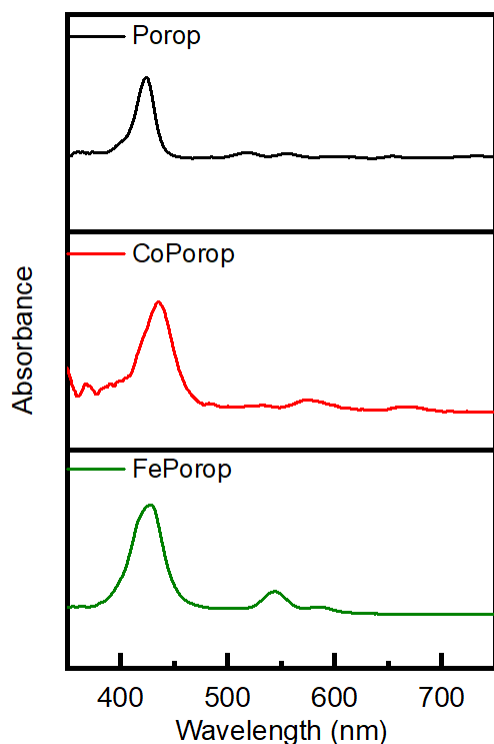


Figure 27. representative UV-vis spectra of synthesized porphyrin organic polymers (**CoPorOP** and **FePorOP**)

The general synthetic scheme is shown in Scheme 7. Terephthalaldehyde (0.500 g, 3.73 mmol) or 2,3,5,6-tetrafluoroterephthalaldehyde (0.768 g, 3.73 mmol) was dissolved in propionic acid (400 mL) while freshly distilled pyrrole (0.250 g, 3.73 mmol) was dissolved in propionic acid (40 mL). The pyrrole solution was slowly added to the terephthalaldehyde solution with constant stirring. The reaction mixture was allowed to react under reflux conditions for 12 h. The resultant product was cooled down and filtered using a medium coarse filter frit and was washed thoroughly with (1) deionized water, (2) methanol, (3) tetrahydrofuran and finally (4) dichloromethane. The filtered and washed product was vacuum dried at 80°C to remove any residual solvents to obtain the final products as black powder. [Yield: F(Por)OP: 0.705 g, 79.40%; (Por)OP: 0.459 g, 74.10%]

4.4.2 Synthesis of cobalt porphyrin organic polymer [(Co(Por)OP) and CoF(Por)OP] and iron porphyrin organic polymer [(Fe(Por)OP) and FeF(Por)OP]:⁵⁴

The general synthetic scheme is shown in Scheme 2. In separate syntheses, (Por)OP or F(Por)OP (0.325 g) and the corresponding metal salts [Co(OAc)₂·4H₂O and FeCl₂·4H₂O] (1.10 g)

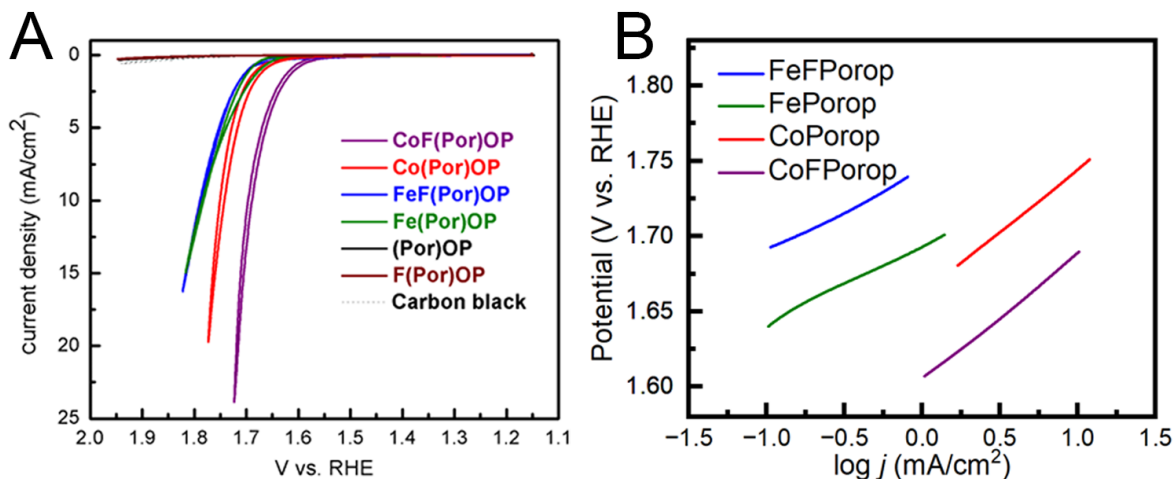


Figure 28. Cyclic Voltammograms of (Por)OP, F(Por)OP, Co(Por)OP, CoF(Por)OP, Fe(Por)OP, FeF(Por)OP and carbon black with iR compensation in the presence of 0.1 M KOH electrolyte solutions saturated with oxygen gas; Scan rate: 10 mV/s.

were dissolved in a mixture solvent of propionic acid and DMF (400 mL, v/v = 2:1). The reaction mixtures were heated under reflux with constant stirring for 3 days. The solutions were subsequently cooled down and filtered using a medium coarse filter frit. The black filter cake was washed with deionized water, methanol and dimethylformamide and vacuum dried at 80°C to remove any residual solvents.

4.5 RESULTS AND DISCUSSION

The OER and ORR activity of the newly prepared porphyrin polymers were investigated by CV in O₂-saturated and N₂-saturated 0.1 M NaOH aqueous solution on glassy carbon electrodes. In order to increase the electrical conductivity, Vulcan XC-72 was also loaded onto the glassy carbon electrode.

Figure 28 A shows the polarization curves of all the synthesized polymers, as well as of pure carbon black, which was used in the deposition of catalysts on the working electrodes to enhance the conductivity. All of the metallated species show to be electrocatalytic active with modest overpotentials (η) for oxygen production. At the chosen current density (j) of 10 mA/cm², η is 0.38 and 0.43 V vs. RHE for CoF(Por)OP and Co(Por)OP, respectively, while η is 0.46 V for both Fe(Por)OP and FeF(Por)OP. These electrochemical results are comparable to other reported porphyrin polymeric OER electrocatalysts.^{54,94} On the contrary, both of the metal-free polymers (Por)OP and F(Por)OP show no significant catalytic current increase, implying that the metal centers are the essential catalytic active sites. Additionally, the carbon black also shows no

electrocatalytic activity. The high catalytic behaviour of Co(Por)OP compared to Fe(Por)OP can be attributed to the higher metal loading and the more redox active nature of cobalt. Notably, the metal-free polymer (Por)OP shows no significant catalytic current increase, implying that the metal centers are the essential catalytic active sites.

To further study the OER kinetics, Tafel analysis for CoF(Por)OP, Co(Por)OP, FeF(Por)OP and Fe(Por)OP were obtained. Figure 28 B shows the Tafel plots fitted to the Tafel equation ($\eta = b \log j + a$, where b is the Tafel slope and a is a constant) to obtain the Tafel slope. The Tafel slopes of CoF(Por)OP, Co(Por)OP, FeF(Por)OP and Fe(Por)OP are determined to be 84.2, 72.8, 89.8 and 91.7 mV/dec respectively, which are comparable to or better than previous reported similar porphyrin polymer-based catalytic systems.^{54,94} These results further indicate that both metalloporphyrin polymeric materials are efficient and promising OER electrocatalysts. EIS measurements were conducted to gain further insight into the charge transfer kinetics of as-synthesized porphyrin polymer towards OER. Figure 29 describes the obtained Nyquist plots of CoF(Por)OP, Co(Por)OP, FeF(Por)OP and Fe(Por)OP and the corresponding simulation fit by equivalent circuit. The simulation curves are in good agreement with the experimental impedance data, thus validating the proposed equivalent circuit for all the synthesized materials. It is worth to mention that Co metalated Porop have different interfacial electron transfer pathway as the Porop

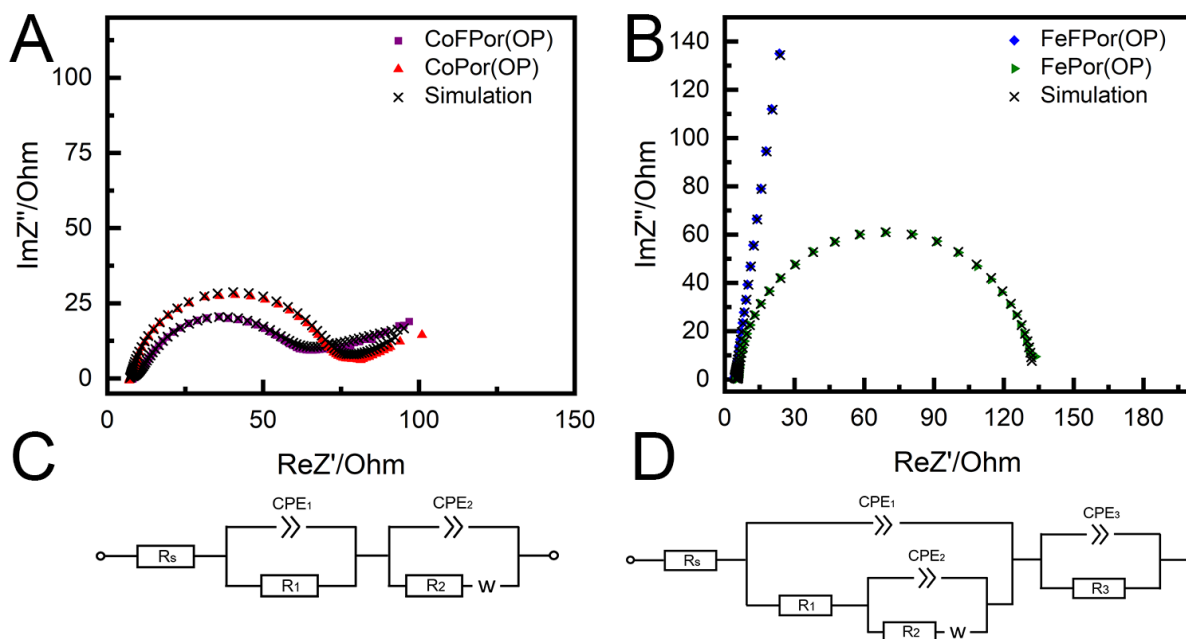


Figure 29. Electrochemical impedance spectroscopy and the corresponding equivalent electric circuits.

with Fe metalation. These evidence also consistent with LSV data since a more complicate circuit is corresponding to less kinetic favor processes in the case of FePorOP/FeFPorOP.

The durability of Co(Por)OP and Fe(Por)OP was evaluated using chronoamperometry at $j = 10 \text{ mA/cm}^2$. Figure 30 shows the current density response as a function of time. While Fe(Por)OP shows almost no changes in current density over a period of 16 hours of continuous electrolysis, Co(Por)OP exhibits ca. 0.7 mA/cm^2 loss of current density. This observation indicates both materials are stable for OER.

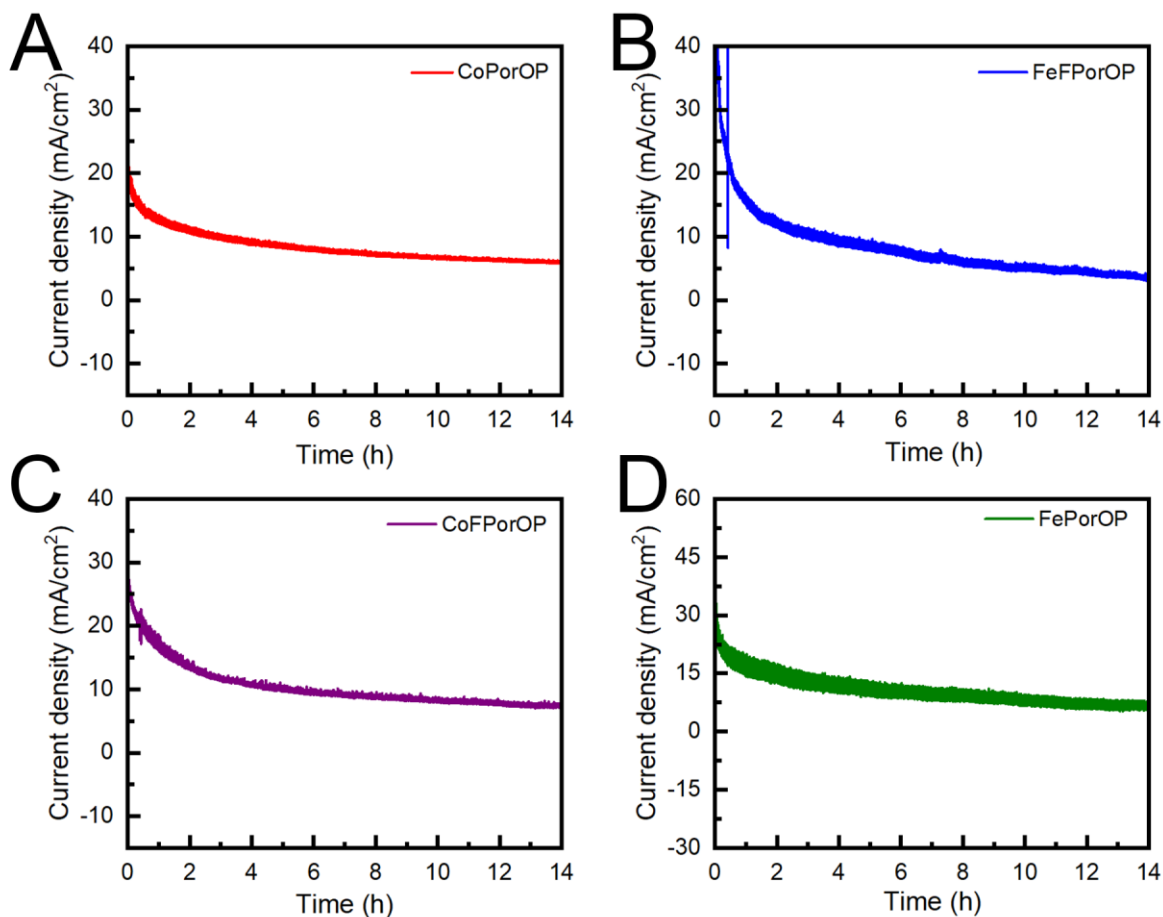


Figure 30. Chronoamperometry of the synthesized porphyrin organic polymers with current maintained at 10 mA/cm^2 for 14 hours.

4.6 CONCLUSIONS

In conclusion, we have successfully synthesized and characterized two metalloporphyrin-based polymers with cobalt and iron and their fluorinated version, which were obtained from a facile one-step condensation reaction of pyrrole and the respective aldehyde in the presence of

propionic acid. Both polymers were implemented as substrates for direct metalation using cobalt and iron to prepare four different metalloporphyrin organic polymers. These materials were used as oxygen evolution from alkaline aqueous media through electrochemical means. All of the metallated porphyrin polymers exhibit to be efficient and durable OER electrocatalysts by requiring moderate overpotentials while the metal-free polymers are catalytically inert under the same conditions.

Chapter 5*

Amine and Carbon-pretreated nickel molybdenum disulfide as bifunctional electrocatalysts for hydrogen and oxygen gas evolution

5.1 INTRODUCTION

Transition metal dichalcogenides (TMDs) where chalcogens are sulfur, selenium, or tellurium, are traditionally used as catalysts for the hydrodesulfurization process to lower the sulfur content in natural gas and crude oil^{116–118}. Among these materials, molybdenum disulfide (MoS₂) has recently obtained substantial interest as a promising electrocatalyst for HER^{119–122} and OER.¹²³ Density functional theory (DFT) calculations indicate that MoS₂ possesses similar free energy when binding with atomic hydrogen to those of Pt metal, which endows MoS₂-based materials in an alternative category for noble metal-free catalysts towards HER.¹²⁴ Previous research shows that doping with transition metal enhances the oxygen/hydrogen generation efficiency during electrocatalysis.^{125–130} MoS₂ doped with earth-abundant transition metal (Fe, Co, Ni, etc.)^{123,131–133} also exhibits highly efficient HER and OER catalytic activity. The constructed interfaces between MoS₂ and the transition metals are fundamental to facilitate the absorption of H* and OH, and therefore enhance OER kinetics.¹³³ However, few of the reported MoS₂-based electrocatalysts are capable of catalyzing both HER and OER.

Experimental and computational studies have shown that the basal planes of bulk 2H MoS₂ are catalytically inert for water splitting, whereas the under-coordinated Mo-S sites along the edges or defects are the actual active sites for the electrocatalytic response.¹³⁴ Therefore, activating the basal plane and increasing more exposed active sites are efficient ways to overcome the inherent limitation of 2H MoS₂.¹³⁵ Introducing organic amines and carbon sources in the precursors during the hydrothermal synthetic process has proved to be an effective strategy to increase the mass-specific activity of MoS₂ based materials.^{136,137} The carbon skeleton will decompose to the corresponding gaseous byproducts under high pressure and temperature resulting in porous defects within the MoS₂ structure and enhanced surface area resulting in an enhancement to the water-

* *This project is already published, see:*

Yulu Ge, Yanyu Wu, Lei Ma, Brenda Torres, Dino Villagran, Amine and Carbon Pretreated Nickel-Molybdenum Disulfide as Bifunctional Electrocatalysts for Hydrogen and Oxygen Gas Evolution, International Journal of Hydrogen Energy, 2022, 47, 27839

splitting efficiency (HER and OER).¹³⁸ Our previous work¹³⁹ indicates that amine-pretreatment (where the amine sources were 1-dodecylamine, diethylenetriamine, tetradecyltrimethylammonium bromide, and cetyltrimethylammonium) of the molybdate precursors can yield porous CoMoS₂ materials with enhanced surface area up to 69 m²/g comparing to CoMoS₂ prepared without any amine-pretreatments (surface area of 35 m²/g). Doping MoS₂ with Co lowers the hydrogen adsorption energy and accelerates electron transfer resulting in efficient HER catalytic behavior and higher conductivity compared to pristine MoS₂.¹³⁹ Furthermore, the increased exposed active sites due to enhanced surface area and porous structure lead to a more accessible reaction substrate into the internal structure of MoS₂ and further promoting the catalytic process. In this work, we extend the study using Ni-promoted MoS₂ (NiMoS₂) and ATM precursors that are modified with other amines and a carbon source and evaluate their effects on electrocatalytic HER. We further expand these studies to OER and find that these materials have bifunctional activity. Herein, we present a series of Ni-doped 2H phase MoS₂ as heterogeneous electrocatalysts towards HER in acidic solution and OER in alkaline solution. The porous structure originates from the decomposition during the hydrothermal synthesis of pre-treated ATMs with diethylenetriamine (DETA), ethylenediamine (EDA), or carbon nanotubes (CNT) which possess carbon skeletons. Electrochemical studies including linear scanning voltammetry, electrochemical impedance spectroscopy, scan rate dependent cyclic voltammetry, and bulk electrolysis show that the pretreated NiMoS₂ catalysts exhibit enhanced catalytic efficiency and faster reaction kinetics toward both HER and OER when compared with the pristine NiMoS₂.

5.2 MATERIALS AND METHODS

5.2.1 Materials

Ni(NO₃)₂·6H₂O, ethylenediamine (EDA), and diethylenetriamine (DETA) were purchased from Aldrich Chemical Company. Sulfuric acid (H₂SO₄) and potassium hydroxide (KOH) were purchased from Fisher Scientific. Nafion® 117 solution (5% w/w in H₂O and 1-propanol) was purchased from AlfaAesar. Carbon black (Vulcan XC-72) was purchased from FuelCell Store. All chemicals were used without further purification. All the glassware and cells were decontaminated by soaking in aqua regia solution (conc. HCl/conc. Nitric acid = 3:1). The glass apparatus was washed with deionized water and oven dried.

5.2.2 Physical measurements

All the NiMoS₂ samples were characterized by scanning electron microscopy (SEM), energy-dispersive X-ray spectroscopy (EDX), and powder X-ray diffraction (pXRD) analyses. SEM and EDX studies were performed on an SEM Hitachi S-4800 instrument. XRD data were obtained on a Panalytical Empyrean X-ray Diffractometer.

5.2.3 Electrochemical methods

All electrochemical measurements were performed in a three-compartment electrochemical glass cell using a CHI760D potentiostat. A graphite rod (5 mm) was used as the counter electrode, and a saturated calomel electrode (SCE) was employed as the reference electrode. Aqueous H₂SO₄ and KOH solutions were used as the electrolytes and purged with nitrogen gas to remove the dissolved oxygen before each measurement. To minimize the double layer charging, a low scan rate of 0.005 V/s was used to perform linear sweep voltammetry (LSV). Electrochemical impedance spectroscopy (EIS) was obtained at a potential of 250 mV vs. RHE from 100 kHz to 0.1 Hz with an AC voltage of 5 mV. Bulk electrolysis and chronoamperometric measurements were tested at the voltage with a current density of 1 mA for 7000 s at ambient atmosphere. All potentials referenced to the saturated calomel electrode (SCE) were calibrated with respect to the reversible hydrogen electrode (RHE). Using the equation: $E = E_0 + 0.245 + 0.059 \times \text{pH}$, all the experimental potential data were calibrated with the pH = 0 for the HER and pH = 14 for the OER studies. A 2 mm diameter platinum working electrode was also used as a reference in linear sweep voltammetry in 0.5 M H₂SO₄ solution with a scan rate of 0.1 V/s, the obtained potentials using SCE as reference electrodes were added by + 0.279 V to be referred to RHE. All the current densities obtained were normalized by dividing the obtained current response by the geometric area of the working electrode

5.2.4 Preparation of NiMoS₂ modified carbon paper electrode

Catalysts NiMoS₂-CNT, (1); NiMoS₂-DETA, (2); NiMoS₂-EDA, (3); NiMoS₂-Pristine, (4) were coated on carbon paper stripe substrates and utilized as working electrodes for electrochemical studies. A catalyst ink was prepared by mixing NiMoS₂ powder (5.00 mg), carbon black (2.5 mg), 2-propanol (1.00 mL) and Nafion solution (4.08 μL). The mixture was ultrasonicated for 30 mins to generate a homogenous suspension. Carbon paper was cut into 0.5cm × 2cm stripe and dried at 30 °C for 12 hours in the air to remove moisture prior to use. 10.00 μL of

the as-prepared catalysts ink was dropcasted on the carbon paper and was allowed to dry in ambient atmosphere for 10 min before each measurement.

5.3 SYNTHESSES

5.3.1 Synthesis of NiMoS₂ using alkyl-containing thiomolybdate precursors (1-3)

The unsupported Mo-based sulfide materials were produced by thermal decomposition. Ammonium tetrathiomolybdate (ATM) was synthesized by dissolving ammonium heptamolybdate (25.0 g, 0.0215 mol) in 120 mL of deionized water (DIW) followed by the addition of (NH₄)₂S (200 mL, 1.170 mol). The mixture was stirred at 55 °C for 30 min and then refrigerated in the original solution to crystallize the final product. A solution of 2 equivalents (0.0384 mol) carbon nanotube or alkyl containing amines in 5 mL DIW was prepared to react with the as-synthesized ATM (5.0 g, 0.0192 mol) in 50 mL DIW to form highly dispersed MoS₂ particles. Afterward, a solution of Ni(NO₃)₂·6H₂O (4.93 g, 0.0270 mol) in 10 mL DIW was added to the reaction mixture. The precipitate was filtered and placed into the Parr reactor vessel (Model 4560) under 300 °C and 8.96 MPa for 2 h. Once the reaction was finished, the reactor was cooled down below 70 °C, and the resulting products were washed with isopropanol and DIW and then dried in air overnight.

5.3.2 Synthesis of NiMoS₂ using ammonium tetrathiomolybdate (ATM) precursors (4)

The synthesis of the pristine NiMoS₂ followed the same procedure of 1-3 without the pretreatment of ATM with carbon nanotube or amines.

5.3.3 Synthesis of carbon nanotubes

Carbon nanotubes were synthesized by vapor pyrolysis: a syringe pump is used to feed 20 mL of precursor solution (0.75 g of ferrocene in 25 mL of toluene) at a rate of 1 mL /min into a preheater, where the solution is vaporized at 180 C. As the vapor forms, the precursors are carried by 1 L/min of Ar into a quartz tube that is placed inside a tube furnace at 800 C, where the hydrocarbon and the ferrocene are pyrolyzed and precipitated on the quartz tube wall as carbon nanotubes. After synthesis, the furnace and the preheater are allowed to cool to room temperature under Ar flow. Finally, the CNTs formed are scraped off the wall of the quartz tube and collected for later use.

5.4 CHARACTERIZATIONS

*p*XRD (powder X-ray diffraction) patterns were obtained to investigate the crystallinity of the synthesized materials and are displayed in Figure 27. All the NiMoS₂ materials possess different diffraction patterns due to the Ni atom doping and the resulting structural changes due to doping and amine pre-treatment when compared with MoS₂. The pristine NiMoS₂ (**4**) shows diffraction peaks at 2θ values of 14.3°, 29.0°, 32.6°, 35.8°, and 55.9° corresponding to the (0 0 2), (0 0 4), (0 1 0), (0 1 2), and (0 1 6) crystal facets, respectively, are attributed to hexagonal (2H phase) MoS₂ (ICDD# 98-064-4259).¹⁴⁰ For the NiMoS₂ pretreated with amines and carbon nanotubes (**1-3**), the diffraction patterns have a lower intensity when compared to the pristine NiMoS₂. The diffraction peaks also slightly shifted to lower 2θ values which indicate the increase in unit cell parameters and unit cell volume. Specifically, the peak at $2\theta = 14.3^\circ$ which is assigned to be the basal plane (0 0 2) of MoS₂ is shifted in **2** and **3** and disappeared in **1**. This indicates the inner structure layer arrangement of MoS₂ in **1-3** is different from the pristine NiMoS₂, which can be induced by the decomposition of amines and carbon nanotube during the syntheses.

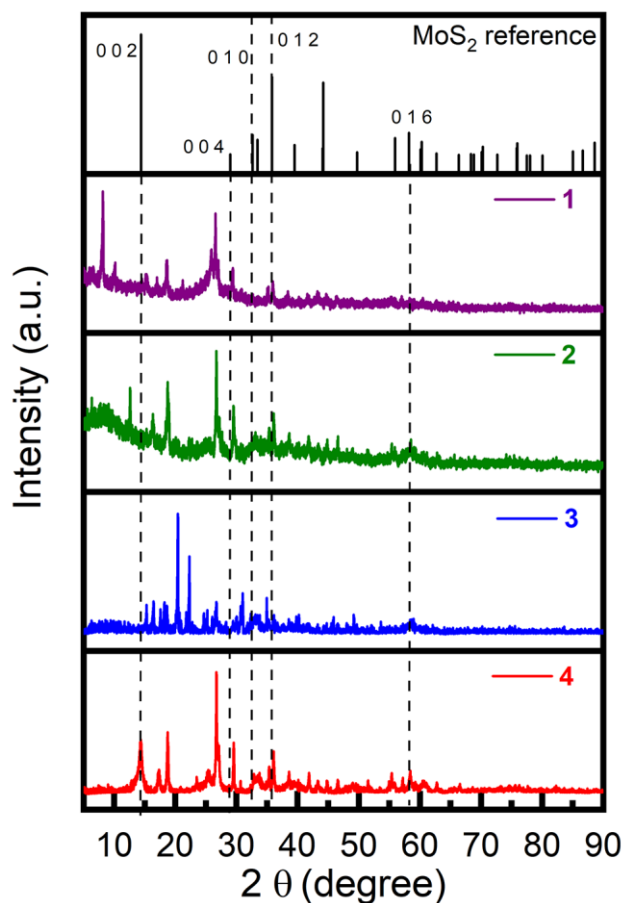


Figure 31. *p*-XRD patterns of **1-4**.

Representative SEM images of as-synthesized materials are shown in Figure 32. It is found that the morphology of all the samples have a lamellar architecture. Due to the hydrothermal decomposition of amines and carbon nanotube during the syntheses, porous tunnels are observed in the surface morphology of **1-3**. By comparison, the pristine NiMoS₂ shows smaller pores and a smoother surface morphology. The elemental composition of all the samples reported in this work was analysed by EDX elemental mapping, which is depicted in Figures 33 and 34. The elemental graphs of **1-4** corroborate the that these materials are composed of Ni, Mo and S, in addition to traces of oxygen. The presence of oxygen can be attributed to exposure to air, a result which has been observed by others.¹⁴¹

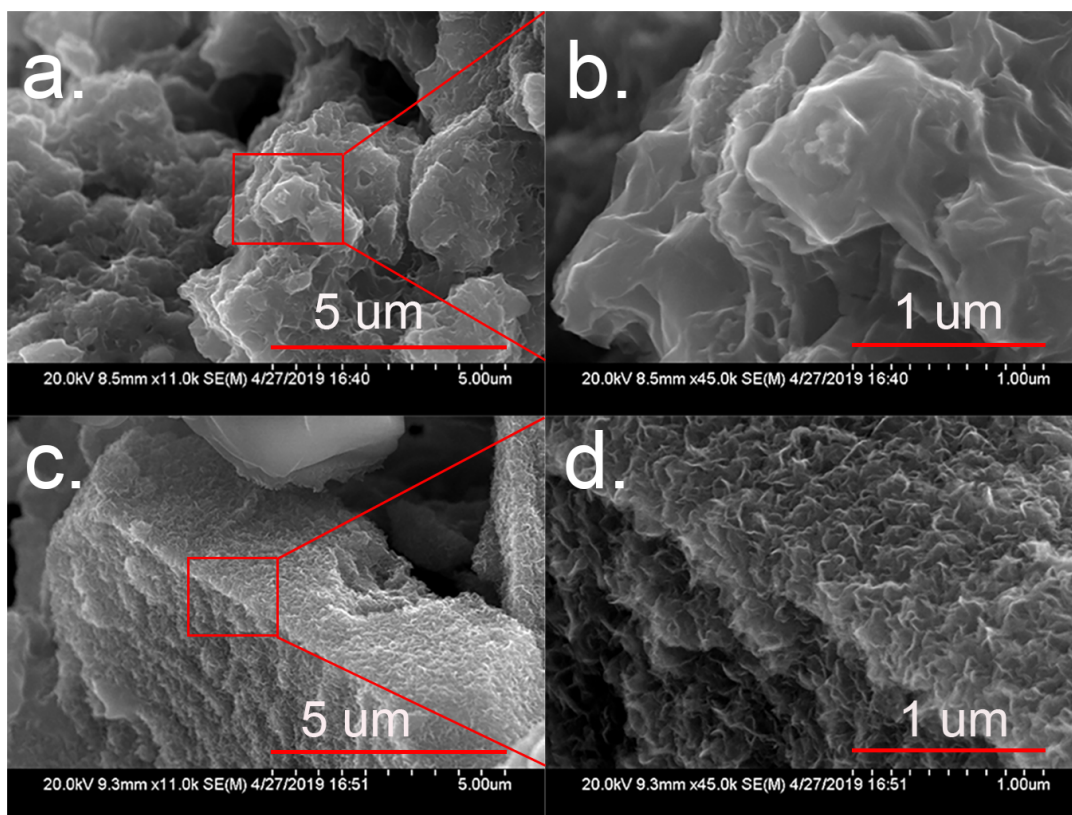


Figure 32. SEM images showing the morphologies of (a-b) sample **4** and (c-d) representative pre-treated NiMoS₂ (sample **2**) at two different scales.

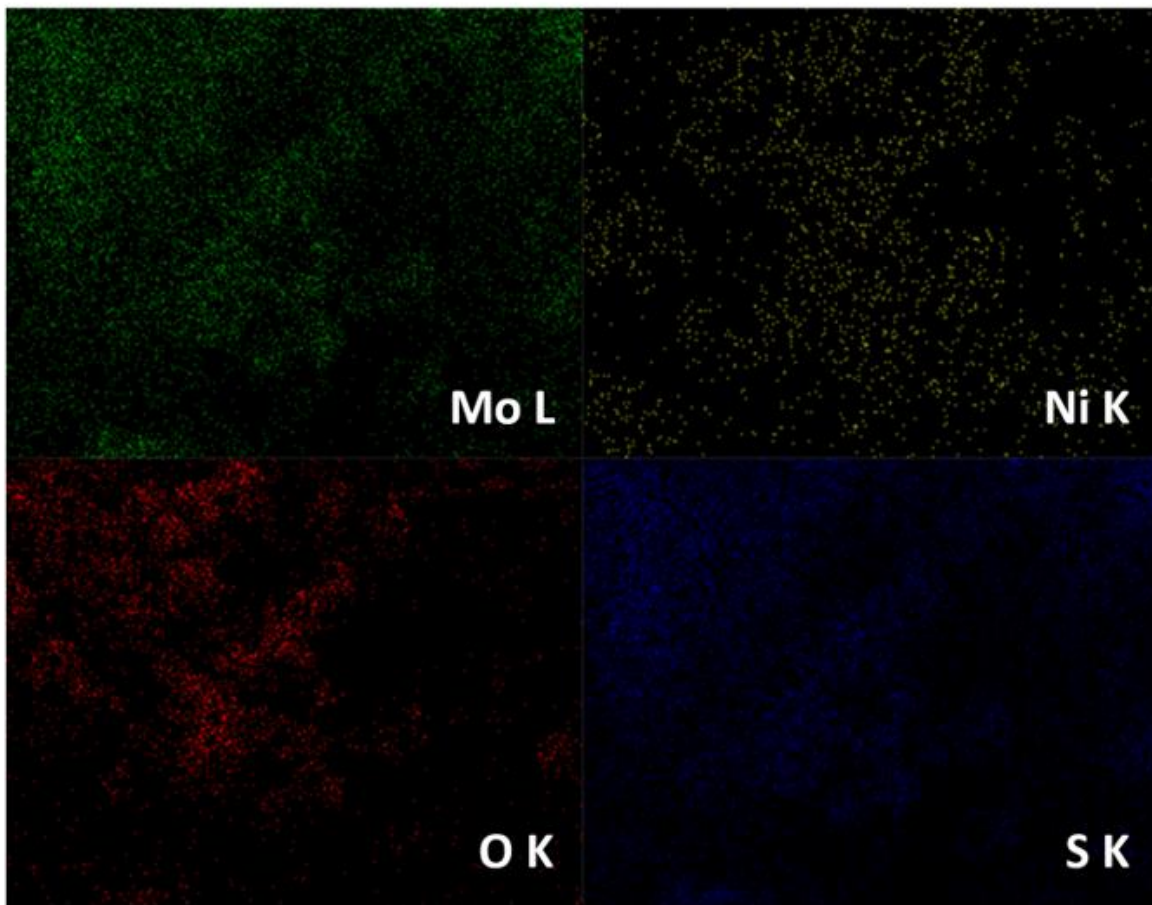


Figure 33. Representative elemental mapping images (NiMoS₂-CNT).

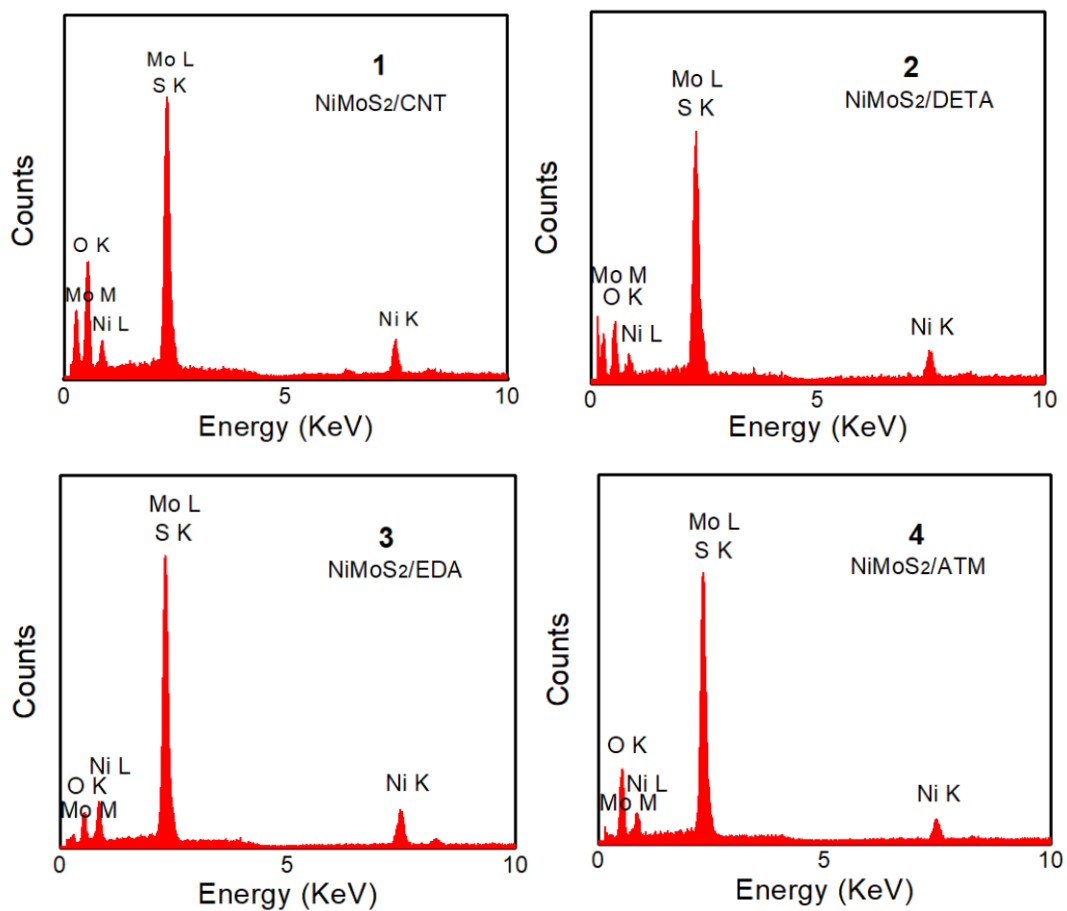


Figure 34. EDX spectra of samples 1-4.

5.5 Results and discussion

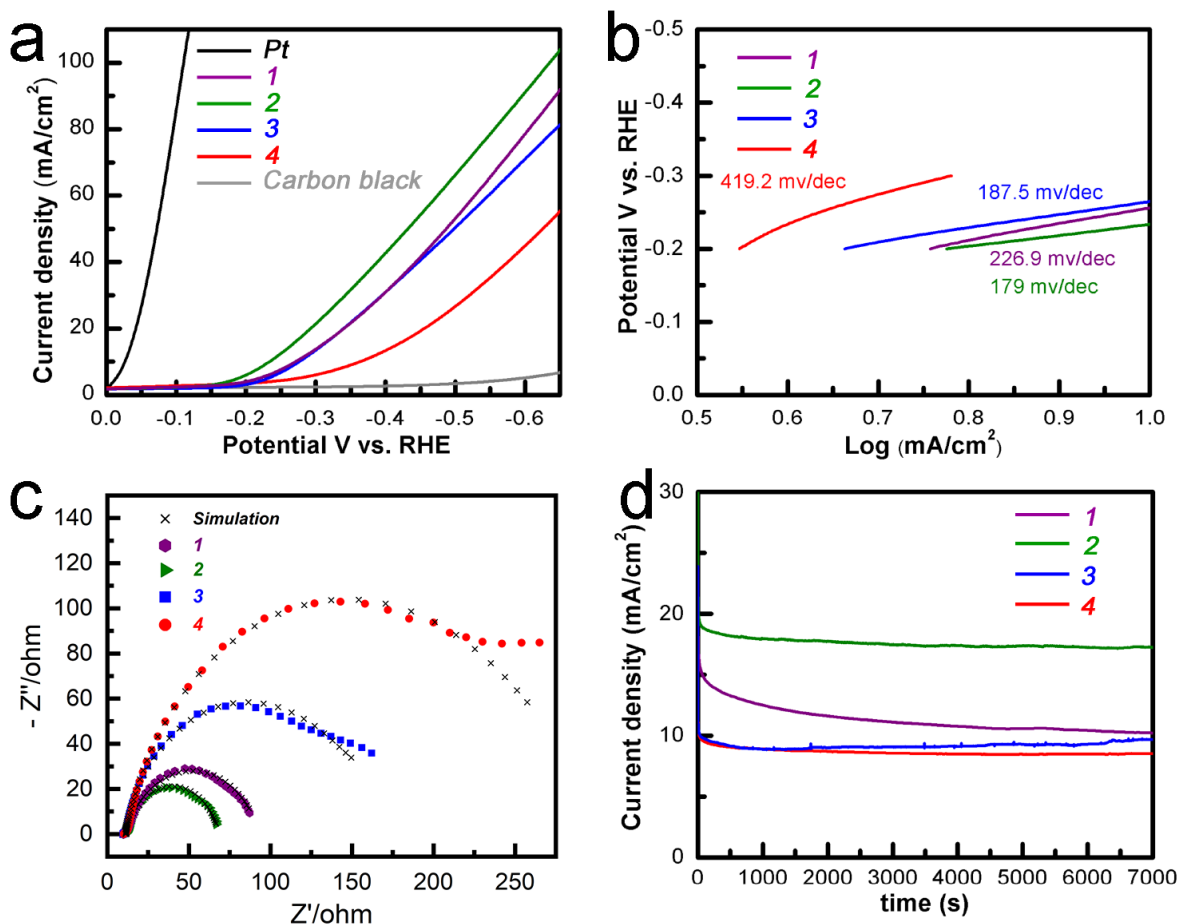


Figure 35. (a) HER Polarization curves in a cathodic potential window for the as-synthesized catalysts: (1) NiMoS₂-CNT (purple); (2) NiMoS₂-DETA (green); (3) NiMoS₂-EDA (blue); (4) NiMoS₂-Pristine (red) and Pt (black) and blank carbon paper doped with carbon black (grey) in 0.5 M H₂SO₄ aqueous solution. Scan rate: 5 mV/s; (b) Tafel plots of 1-4 derived from the HER polarization curves. (c) Nyquist plots of 1-4 in acidic condition. (d) Chronoamperometric studies of the as-synthesized NiMoS₂ (1-4) in 0.5 M H₂SO₄ at $\eta = 0.250$ V.

The HER electrocatalytic activities of all the prepared NiMoS₂ samples supported on carbon paper electrodes were measured in 0.5 M H₂SO₄ aqueous solution. Polarization curves with a cathodic potential window from 0.00 V to –0.65 V vs. RHE are shown in Figure 35 a. Current densities are normalized to the geometric area of the working electrodes for all samples. Platinum metal and carbon paper electrode modified with only carbon black were also studied under the same condition for comparison. Platinum metal generates catalytic current increase immediately at 0 V vs. RHE corresponding to the hydrogen evolution reaction. Negligible current increase was

observed for carbon paper electrode with carbon black within the tested potential range, indicating that the electrode doped with carbon black is catalytically inert. All the samples reported in this study shown considerable catalytic current with current density surpass 50 mA/cm^2 at the displayed potential. The pristine NiMoS₂ (4) exhibits an overpotential η_l of 0.263 V (η_l is the overpotential at $j = 1 \text{ mA/cm}^2$), and η_{10} of 0.366 V vs. RHE (η_{10} is the overpotential an $j = 10 \text{ mA/cm}^2$). In contrast, samples **1**, **2** and **3** show substantially improved electrocatalytic activity with lower onset potentials of 0.189 V, 0.151 V and 0.195 V and η at 10 mA/cm^2 of 0.272 V, 0.238 V and 0.277 V, respectively. The anodic potential shift of the pretreated catalysts compared with the pristine NiMoS₂ demonstrate their superior catalytic property towards HER.

Figure 35 b shows the Tafel plots derived from the cathodic polarization curves of all the studied catalysts. The linear regions of the Tafel plots were fitted to the Tafel equation: $\eta = a + b \log(j)$, where η is the overpotential, b is the Tafel slope and j is the current density.⁷³ Low Tafel slope values indicate faster reaction kinetics. Platinum metal is well known to follow the Volmer-Tafel mechanism with a Tafel slope of around 30 mV/dec for hydrogen generation.⁷² The corresponding Tafel slopes of the pretreated NiMoS₂ samples span from 179 to 226.9 mV/dec,

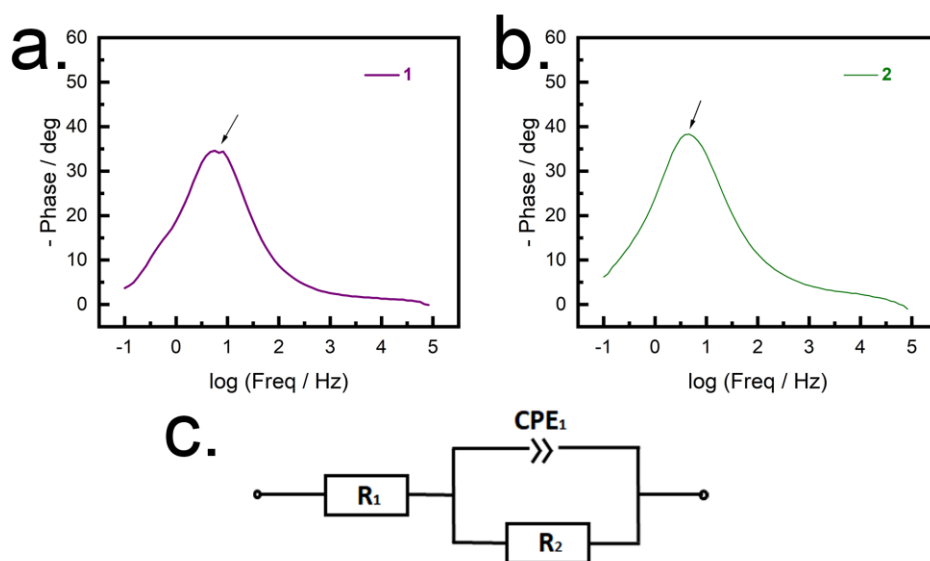


Figure 36. (a) and (b): Bode plot of HER using **1** and **2** as electrocatalysts under 250 mV overpotential with 5 mV AC voltage applied; (c) the simulated equivalent electric circuit of the corresponding electrochemical processes.

whereas pristine NiMoS₂ shows a significantly larger value of 419.2 mV/dec. The differences in Tafel slopes among the samples show that the HER kinetics of pretreated NiMoS₂ are enhanced

compared to the non-pretreated one. Therefore, the overall catalytic reaction process is consistent with a Heyrovsky dominated Volmer mechanism.

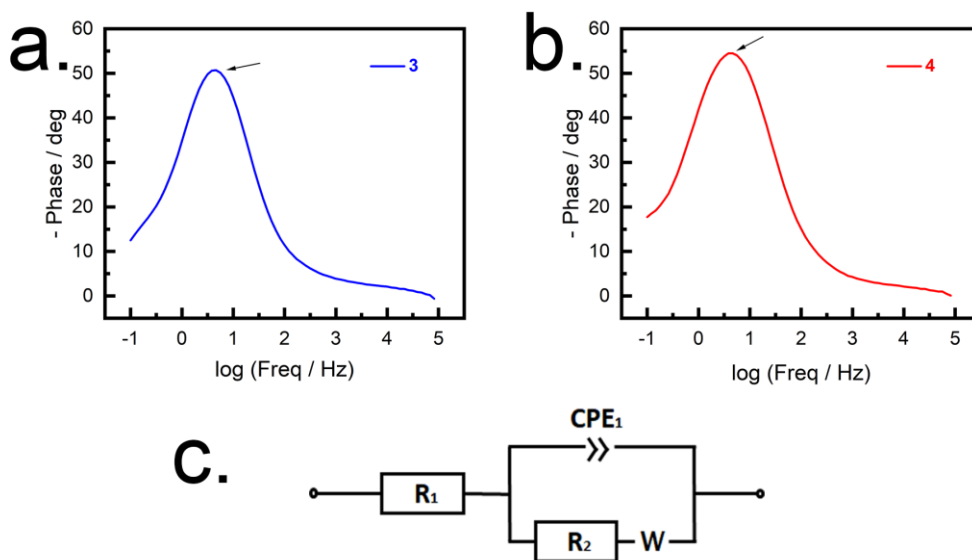


Figure 37. (a) and (b): Bode plot of HER using **3** and **4** as electrocatalysts under 250 mV overpotential with 5 mV AC voltage applied; (c) the simulated equivalent electric circuit of the corresponding electrochemical processes.

TABLE 2. Electrochemical impedance parameters obtained from fitting Nyquist plot data with the equivalent circuit for HER (to three significant digits).

HER	R1 (Ω , ohm)	CPE2 $F \cdot s^{(a-1)}$	a2	R2 (Ω , ohm)	s2
1	11.7	2.32×10^{-3}	0.815	82.6	N/A
2	10.7	2.55×10^{-3}	0.758	56.7	N/A
3	10.4	1.56×10^{-3}	0.852	142.	9.26
4	11.2	1.14×10^{-3}	0.843	254.	21.0

Electrochemical impedance spectroscopy (EIS) analyses were also performed for further insight into the HER catalytic activity. Nyquist plots of **1-4** of the EIS responses are shown in Figure 35 c. All the experimental data are in good agreement with the simulation parameter and fit in Randles circuit models (Figures 36 and 37). Samples **1-3** doped electrodes exhibit relatively smaller semicircles at the chosen overpotential of 250 mV, which indicate a smaller charge-transfer resistance (R_{ct}) kinetics from NiMoS₂ active site to the electrode and faster electron transfer when compared to **4**. Sample **2** shows the best conductivity with the smallest R_{ct} of 56.69 Ω , which explains why it shows the best efficiency for HER (Table 2).

To assess the electrocatalytic stability of the materials, chronoamperometric measurements were conducted at a constant potential of 0.25 V vs. RHE in 0.5 M H₂SO₄ using the prepared NiMoS₂ doped carbon paper electrodes as working electrodes, which are shown in Figure 35d. A higher current density is obtained by **2** compared to the other three samples, and 90% of the original current density is retained after 7000 s of continuous operation. This indicates all these catalysts

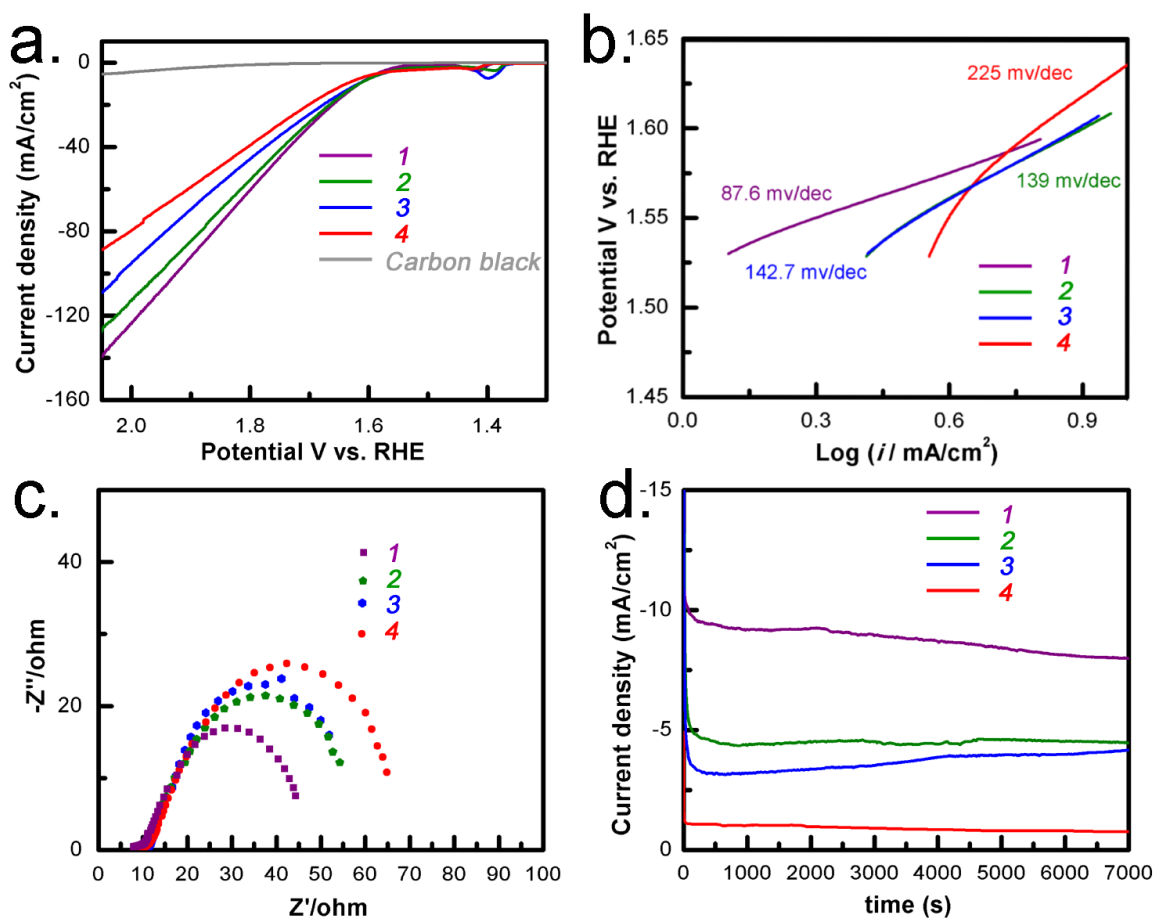


Figure 38. (a) Polarization curves of **1-4** and carbon black as control electrode in 1.0 M KOH as electrolyte. Scan rate: 5 mV/s. (b) Tafel plots of the corresponding NiMoS₂ electrocatalysts (**1-4**) derived from the OER polarization curves. (c) Nyquist plots of **1-4** at an overpotential of 250 mV in 1.0 M KOH aqueous solution. (d) Chronoamperometric studies of **1-4** in 1.0 M KOH at $\eta = 0.250$ V.

are stable under acidic conditions. All the samples show a minimal cathodic current density decrease (less than 10%) after 500 cyclic cathodic sweeps compared to the initial scan.

All the synthesized NiMoS₂ materials were also studied as OER electrocatalysts. Figure 38 shows the anodic polarization curves of catalysts **1-4** in 1.0 M KOH aqueous solution with carbon paper as substrate. It is found that **1** has the best OER activity with the lowest onset potential of 0.310 V and a 0.389 V at current density of 10 mA/cm² (η_{10}). Sample **2** exhibits a similar overpotential value ($\eta_1 = 0.308$ V) to **1**, but has slower OER kinetics and current density. In comparison, the pristine NiMoS₂ has the lowest activity for oxygen generation ($\eta_{10} = 0.408$ V), which is consistent with the HER catalytic measurements shown (*vide supra*). The polarization curve obtained from the carbon black control electrode shows negligible OER activity, which suggests that the catalytic activities originate from the NiMoS₂ catalysts. The OER activity of the pretreated NiMoS₂ catalysts is comparable to those recently reported high-performance MoS₂-based OER electrocatalysts, for instance, the interfaced MoS₂/Ni₃S₂ heterostructures¹³³ ($\eta_{10} = 0.218$ V), the cobalt covalently doped MoS₂¹³¹ ($\eta_{10} = 0.260$ V), MoS₂ quantum dots¹⁴² ($\eta_{10} = 0.370$ V) and the exfoliated 1T MoS₂¹⁴³ ($\eta_{10} = 0.420$ V). Cyclic voltammograms of **1-4** consistently show a reversible oxidation event at around 0.150 V vs. RHE which is assigned to the formal Ni²⁺/Ni³⁺ redox couple,¹⁴⁴ meaning that the redox properties of all the catalysts are similar and that the increase in catalytic efficiency is mainly due to their enhanced porous structure observed in **1-3** with respect to **4**.

The OER kinetics of NiMoS₂ samples were analyzed by Tafel slopes. Figure 38 b presents the Tafel plots of η as a function of $\log j$. As is shown in the plots, **1** exhibits a lowest slope value of 87.6 mV/dec, among all the synthesized catalysts and it is lower than the reported benchmark OER catalyst RuO₂ (135 mV/dec)¹²³, signifying its excellent OER kinetics. Moreover, compared with the pristine NiMoS₂ (Tafel slope = 225 mV/dec), catalysts **2** and **3** both possess significantly lower Tafel slope, indicating that the pretreated NiMoS₂ catalysts demonstrate faster OER kinetics than their pristine counterpart.

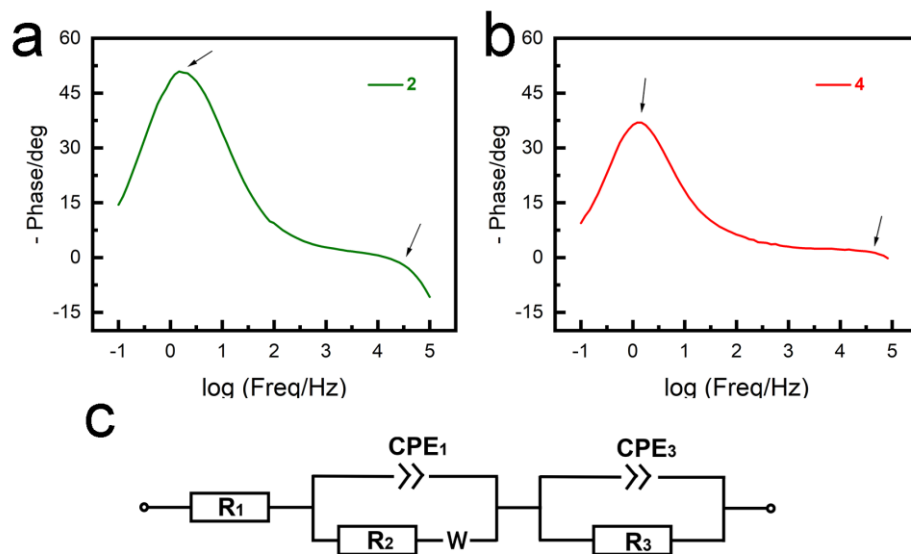


Figure 39. (a) and (b): Bode plot of OER using **2** and **4** as electrocatalysts under 250 mV overpotential with 5 mV AC voltage applied; (c) the simulated equivalent electric circuit of the corresponding electrochemical processes.

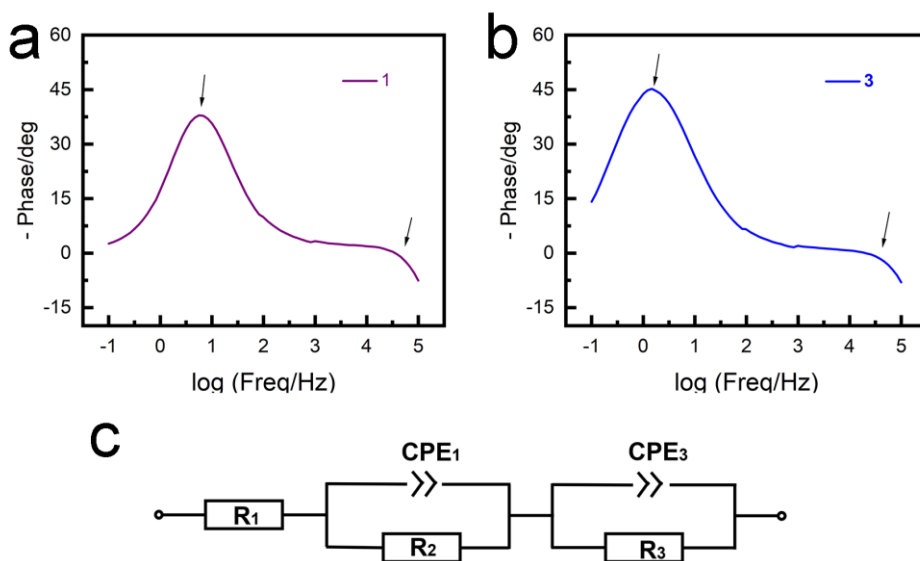


Figure 40. (a) and (b): Bode plot of OER using **1** and **3** as electrocatalysts under 250 mV overpotential with 5 mV AC voltage applied; (c) the simulated equivalent electric circuit of the corresponding electrochemical processes.

Electrochemical impedance spectroscopy (EIS) was carried out on all the samples in 1.0 M KOH solution at a chosen overpotential of 250 mV. Compared to the EIS measurements performed in acidic media, a considerable decreased charge transfer resistance (R_{ct}) for all measured samples is observed in basic condition suggesting faster electron transfer in basic

TABLE 3. Electrochemical impedance parameters obtained from fitting Nyquist plot data with the equivalent circuit for OER (to three significant digits).

OER	R1 (Ω , ohm)	CPE2 $F \cdot s^{(a-1)}$	a2	R2 (Ω , ohm)	CPE3 $F \cdot s^{(a-1)}$	a3	R3 (Ω , ohm)	s2
1	6.00	2.53×10^{-3}	0.914	31.9	3.73×10^{-3}	0.603	1.26	N/A
2	5.56	4.78×10^{-3}	0.857	96.8	1.27×10^{-2}	0.616	1.17	0.304×10^{-3}
3	6.07	1.09×10^{-2}	0.608	0.720	6.88×10^{-3}	0.833	69.5	N/A
4	9.24	6.13×10^{-2}	0.235	13.1	5.71×10^{-3}	0.916	51.0	5.89

environment Figure 38 c shows that the pretreated NiMoS₂ samples exhibit substantially lower R_{ct} with smaller semicircles in their Nyquist plots compared with the pristine NiMoS₂. These decreases R_{ct} s suggest enhanced conductance of NiMoS₂ samples which accelerate OER kinetics by making electrons transfer easier. In addition, the EIS analysis with equivalent model (Figures 35 and 36) to investigate the NiMoS₂ electrode during the OER reaction. The experimental data are fitted with the parameters with respect to the Randles circuit model (Table 3). The equivalent electric circuit consists of two parallel branches connected in series. R_1 is the equivalent series resistance for the electrolyte and constant phase elements (CPEs) are non-ideal capacitance. The first parallel branch account for the interface contacts between NiMoS₂ interlayers and the second branch describe the contact between NiMoS₂ and carbon paper electrode. All the data fit with the simulation parameter.

The stability of the NiMoS₂ modified carbon paper electrodes in the OER experimental conditions were also tested by long-term electrolysis (Figure 38 d) and cyclic voltammetry after 500 constant cyclic scans. All the NiMoS₂ catalysts show a relatively decent stability in alkaline solution, however, a marginal current drop is observed for catalyst **1** and **2** after 500 scans. It is suggested that the oxidation of MoS₂ to its high valent oxides during the multiple cyclic scans is responsible for the current decay. The aggregation of MoO₃ may cover the electrode surface and the formation of nickel hydroxide species may render a slightly decrease of current density¹⁴⁵.

The electrocatalytic activity of the NiMoS₂ catalysts is attributed to both surface area effects and their intrinsic catalytic nature. In order to compare this intrinsic activity of the NiMoS₂ samples reported in this work, their electrochemically active surface area (ECSA) is determined.¹⁴⁶ The ECSA of a material with similar composition is proportional to its electrochemical double-layer capacitance (C_{dl}), which was measured by voltammetric curves in the mere double-layer region with multiple scan rates (0.02 V/s, 0.04 V/s, 0.06 V/s, 0.08 V/s, 0.10 V/s, 0.12 V/s, 0.14 V/s, 0.16 V/s). In this region, only double-layer charging process is occurring and there is no faradaic contributions to the current flowing. The current traces of all the NiMoS₂ materials obtained from non-faradaic potential yield a rectangle shaped CV, which indicate their capacitor behavior (Figure 42 and 43). The C_{dl} is estimated by plotting the current $\Delta j = (j_a - j_c)$ in the middle of the potential window as a function of the scan rate (Figure 37). This plot yields a straight line with a slope equal to C_{dl} , according to the equation:^{119,147}

$$i = dQ/dt = (dQ/dE) \cdot (dE/dt) = C_{dl} \cdot v$$

This capacity value obtained by the above procedure only contains contribution from double layer charging, other contributions such as the pseudocapacity of the process due to electrolyte ion adsorption and intercalation or chemical capacitance from the population of electron trap states are not considered. The EASA of a catalyst can be calculated by referring the obtained specific

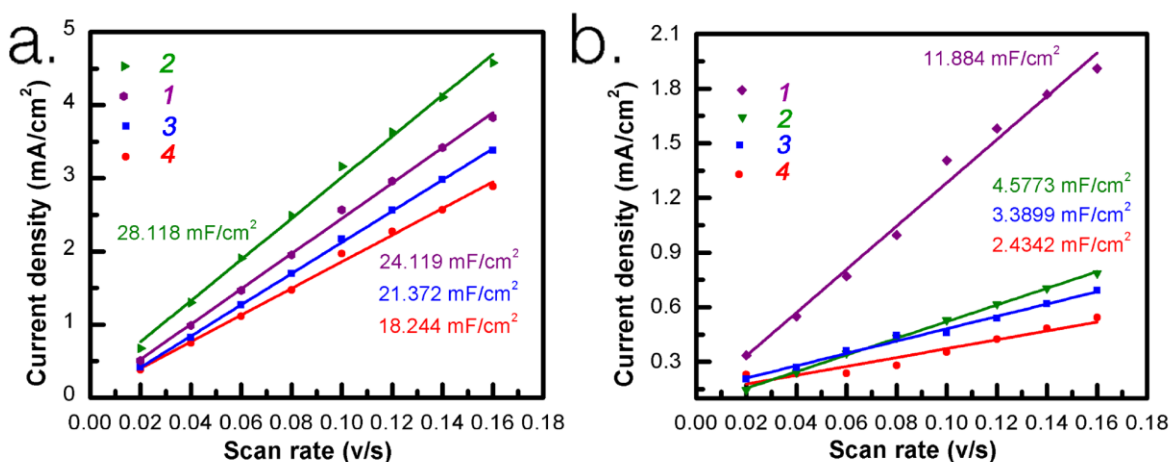


Figure 41. Linear fit plots of scan rates as a function of double layer charging current for the NiMoS₂ (1-4) report in this study. (a) Performed in 0.5 M H₂SO₄ aqueous solution; (b) Performed in 1.0 M KOH aqueous solution. Scan rate: 0.02 v/s, 0.04 v/s, 0.06 v/s, 0.08 v/s, 0.1 v/s, 0.12 v/s, 0.14 v/s, 0.16 v/s.

capacitance (C_s) of the sample or the capacitance of an atomically smooth planar surface of the material per unit area under identical electrolyte conditions following the equation:¹⁴⁷

$$ECSA = \frac{Cdl}{C_s}$$

The specific capacitance values for a variety of metal electrodes in acidic or alkaline solutions have been reported with a range between 0.015-0.110 mF/cm² in H₂SO₄¹⁴⁸ and 0.022-0.130 mF/cm² in NaOH¹⁴⁹ and KOH¹⁵⁰ aqueous solutions. For the determination of ECSA in our electrocatalytical system, we accept $C_s = 0.035$ mF/cm² in 0.5 M H₂SO₄ and $C_s = 0.040$ mF/cm² in 1.0 M KOH solution based on the reported value for the evaluation of catalysts performing HER and OER. With these, the CV measurements were carried out in 0.5 M H₂SO₄ and 1.0 M KOH solution to obtain C_{dl} in both HER and OER. For the HER, catalyst **2** has the largest C_{dl} of 28.118

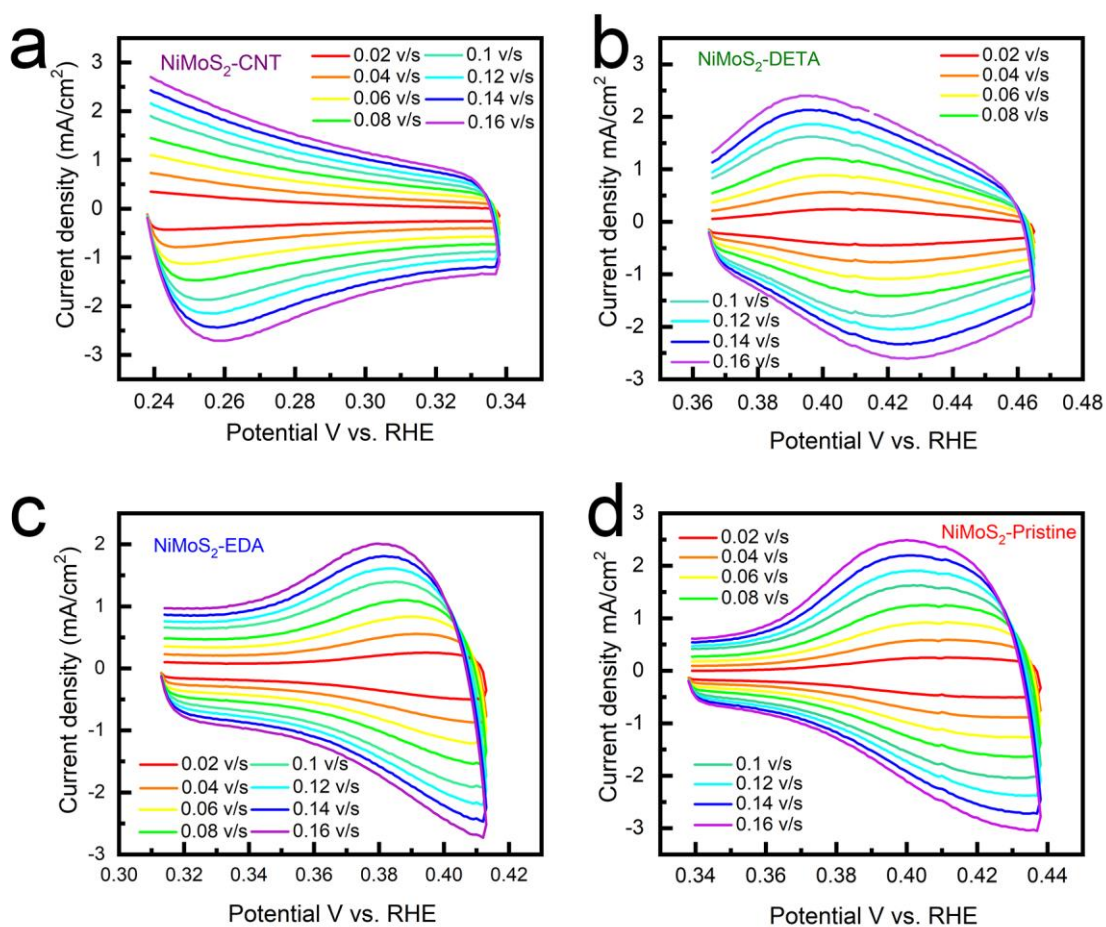


Figure 42. Cyclic voltammograms of NiMoS₂ catalysts **1-4** at different scan rates in the 0.1 V potential window with no faradaic process in 0.5 M H₂SO₄ solution.

mF/cm², while the C_{dl} values of sample **4**, **1** and **3** are 18.244 mF/cm², 24.119 mF/cm² and 21.372 mF/cm², respectively. As a result, the calculated ECSA values derived from the abovementioned equation is 689.11 cm² (**1**), 803.37 cm² (**2**), 610.63 cm² (**3**) and 521.26 cm² (**4**). As for the OER, catalyst **1** shows the highest C_{dl} value of 11.884 mF/cm² among all the studied catalysts, which results in the largest active surface area with ECSA of 297.1 cm² (Figure 41 b). These results show that the improved electrochemical active surface areas for HER and OER of the pretreated NiMoS₂, which result from the enhanced surface areas due to the decomposition of amines and CNT, are the main reason of promoted catalytic performance.

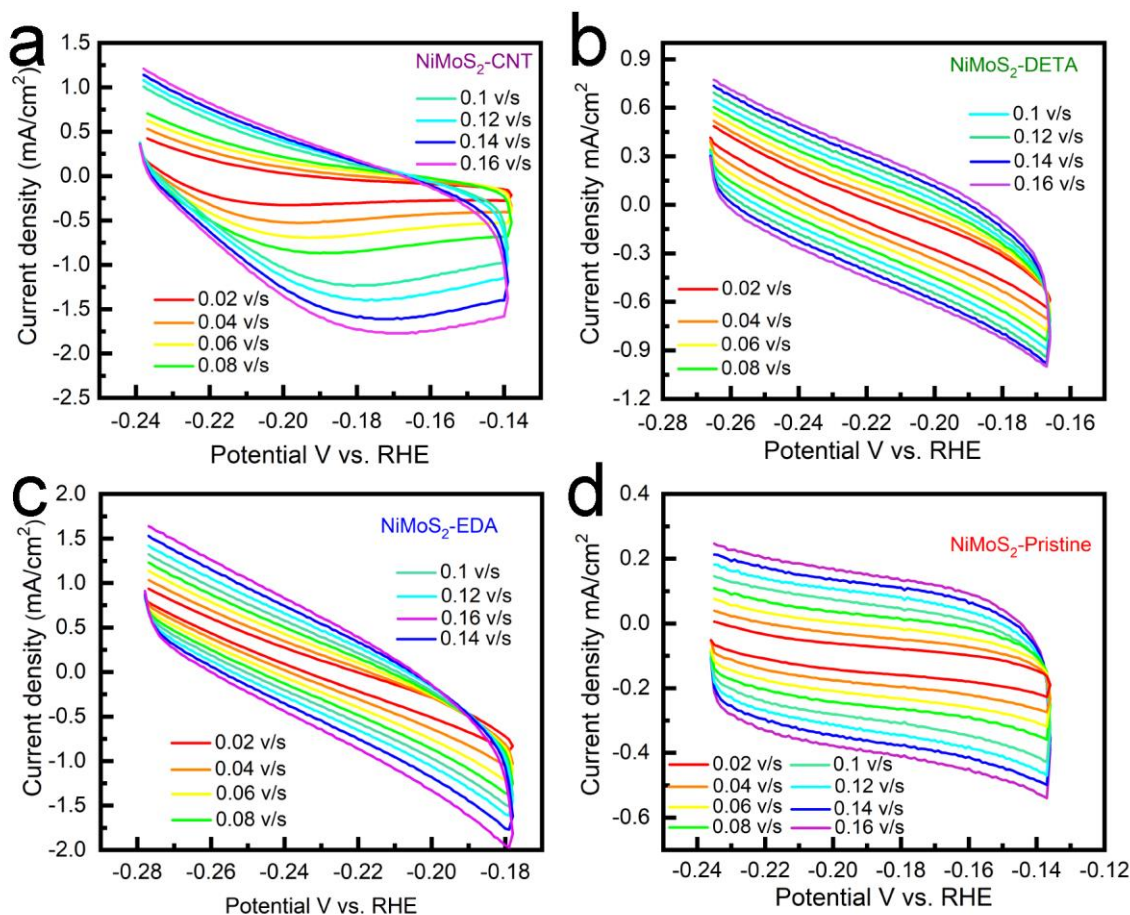


Figure 43. Cyclic voltammograms of NiMoS₂ catalysts **1-4** at different scan rates in the 0.1 V potential window with no faradaic process in 1.0 M KOH solution.

5.6 CONCLUSIONS

In conclusion, we show that the pretreatment of the ammonium thiomolybdate precursor with carbon source (carbon nanotube) and amines (diethylenetriamine and ethylene diamine) is an efficient method to improve the catalytic activity for the overall water splitting reaction including both the HER and OER for NiMoS₂ catalysts. These catalysts exhibit poorer crystalline with porous tunnel structures that potentially increase their catalytical active sites when comparing to NiMoS₂ prepared directly from ATM precursor. Electrochemical studies show that these pretreated NiMoS₂ are efficient bifunctional electrocatalysts and exhibit promising catalytic efficiency, stability and fast reaction kinetics towards electrochemical water splitting. The enhancement of the catalytic activity of the pretreated NiMoS₂ is attributed to the faster charge transfer and larger electrocatalytic active sites of the catalysts, as are evidenced by electrochemical impedance spectroscopy and electrochemical active surface area analysis.

Chapter 6 Conclusion and Future Work

The unrestricted exploitation of fossil fuels will continue to greatly influence the planet; thus, it is imperative that great effort continues to be put forth in order to eliminate this objective detriment. Through this work, steps were made toward the cost-effective generation of hydrogen gas as an energy source to replace fossil fuels. Water is the most abundant resource on earth. To harness this resource, we have conducted water electrolysis to generate hydrogen gas. Through rational catalyst design, we have come closer to achieving this effort. Several catalysts were made to increase the energy efficiency of water splitting. In chapter 2, we explored the mechanism of hydrogen generation by regulating the electron negativity associated with molecular porphyrins. To do this, we synthesized four metal free porphyrins with different functional groups: tetrakis meso phenyl F, F₂, F₃, and Br porphyrin. This allowed the four-nitrogen core to have altered electrochemical activity that could be studied to reach a greater understanding of the means in which these macromolecules can generate hydrogen gas. Depending on the electronegativity assigned to each porphyrin, the basicity of the nitrogen core is affected. Although the core's ability to be protonated can be made more or less facile, each porphyrin is still capable of hydrogen generation, albeit with vastly different mechanisms: the Br and F porphyrins are easily protonated, allowing them to readily generate hydrogen gas without the need for first experiencing electron transfer. The F₂ and F₃ porphyrins still generate hydrogen at low overpotentials, however, the mechanism first requires reduction. To continue this work, it will be necessary to pair the findings with an understanding of their associated DFT calculations to determine the absolute energy required to catalyze this reaction. Then, new porphyrins with appropriate functionality must be synthesized that take full advantage of these present and future findings. In chapter 3, we conceived a more stable and applicable heterogenous metal free porphyrin framework as a bifunctional catalyst for water splitting: Porphyrin Kevlar (Porphvlar). In pH dependent conditions, Porphvlar can generate oxygen at $\eta=400$ mV and hydrogen at $\eta=36$ mV, which is comparable to most metal-based catalysts. In neutral solution, Porphvlar is able to catalyze water splitting. Bulk electrolysis shows that Porphvlar is considerably stable under sustained electrolysis condition, up to 60 hours, owing to Kevlar's exceptionally sturdy structure. Future work must include metalating Porphvlar with early transition metals in order to explore the energy related small molecule activation. In chapter 4, we discovered that by changing the linker of the porphyrin organic polymer, the water splitting efficiency changed. Additionally, Co and Fe metalation results in different OER

overpotentials: by metalating the framework, better catalytical performance was observed. Alternating the heterogenization strategy can facilitate electron and proton transfer on metal centers to different extents. Future work including changing the metal centers into other transition metals and corresponding mechanism studies must be addressed to increase the efficiency and stability of porphyrin catalyzed water splitting. In chapter 5, Nickel doped molybdenum disulfide was synthesized. By pretreatment with carbon nanotubes and DETA and EDA, the surface area of the material is enlarged, thus, the electrochemical activity is greatly benefited. When catalyzing the water splitting reaction, these materials can facilitate both HER and OER. DETA pretreatment is optimal for HER, conversely, carbon nanotube pretreatment is best for OER. Detailed mechanism studies are required for the continuation of this work. Also, these materials with the proper pretreatment can be essential to nitrate reduction in natural waters, thus furthering the extent of necessity in mechanism study.

This being said, the world energy crisis can be averted by developing cheap materials to replace precious metals as catalysts for the hydrogen generation reaction.

References

- (1) Lewis, N. S.; Nocera, D. G. Powering the Planet: Chemical Challenges in Solar Energy Utilization. *Proc. Natl. Acad. Sci.* **2006**, *103* (43), 15729–15735. <https://doi.org/10.1073/pnas.0603395103>.
- (2) Winsche, W. E.; Hoffman, K. C.; Salzano, F. J. Hydrogen: Its Future Role in the Nation's Energy Economy. *Science* **1973**, *180* (4093), 1325–1332. <https://doi.org/10.1126/science.180.4093.1325>.
- (3) Gholipour, M. R.; Dinh, C.-T.; Béland, F.; Do, T.-O. Nanocomposite Heterojunctions as Sunlight-Driven Photocatalysts for Hydrogen Production from Water Splitting. *Nanoscale* **2015**, *7* (18), 8187–8208. <https://doi.org/10.1039/C4NR07224C>.
- (4) Bockris, J. O. The Origin of Ideas on a Hydrogen Economy and Its Solution to the Decay of the Environment. *Int. J. Hydrog. Energy* **2002**, *27* (7), 731–740. [https://doi.org/10.1016/S0360-3199\(01\)00154-9](https://doi.org/10.1016/S0360-3199(01)00154-9).
- (5) *Fuels and Energy for the Future: The Role of Catalysis: Catalysis Reviews: Vol 46, No 3-4*. <https://www.tandfonline.com/doi/full/10.1081/CR-200036716> (accessed 2019-08-01).
- (6) Chhowalla, M.; Shin, H. S.; Eda, G.; Li, L.-J.; Loh, K. P.; Zhang, H. The Chemistry of Two-Dimensional Layered Transition Metal Dichalcogenide Nanosheets. *Nat. Chem.* **2013**, *5* (4), 263–275. <https://doi.org/10.1038/nchem.1589>.
- (7) *Computational high-throughput screening of electrocatalytic materials for hydrogen evolution | Materials for Sustainable Energy*. https://www.worldscientific.com/doi/abs/10.1142/9789814317665_0041 (accessed 2019-08-01).
- (8) Wang, Y.; Wang, Q.; Zhan, X.; Wang, F.; Safdar, M.; He, J. Visible Light Driven Type II Heterostructures and Their Enhanced Photocatalysis Properties: A Review. *Nanoscale* **2013**, *5* (18), 8326–8339. <https://doi.org/10.1039/C3NR01577G>.
- (9) Park, M.-S.; Kang, M. The Preparation of the Anatase and Rutile Forms of Ag–TiO₂ and Hydrogen Production from Methanol/Water Decomposition. *Mater. Lett.* **2008**, *62* (2), 183–187. <https://doi.org/10.1016/j.matlet.2007.04.105>.
- (10) Terlouw, T.; Bauer, C.; McKenna, R.; Mazzotti, M. Large-Scale Hydrogen Production via Water Electrolysis: A Techno-Economic and Environmental Assessment. *Energy Environ. Sci.* **2022**, *15* (9), 3583–3602. <https://doi.org/10.1039/D2EE01023B>.
- (11) Nguyen, T.; Abdin, Z.; Holm, T.; Mérida, W. Grid-Connected Hydrogen Production via Large-Scale Water Electrolysis. *Energy Convers. Manag.* **2019**, *200*, 112108. <https://doi.org/10.1016/j.enconman.2019.112108>.
- (12) Yan, Y.; Yu Xia, B.; Zhao, B.; Wang, X. A Review on Noble-Metal-Free Bifunctional Heterogeneous Catalysts for Overall Electrochemical Water Splitting. *J. Mater. Chem. A* **2016**, *4* (45), 17587–17603. <https://doi.org/10.1039/C6TA08075H>.
- (13) Wang, F.; Shifa, T. A.; Zhan, X.; Huang, Y.; Liu, K.; Cheng, Z.; Jiang, C.; He, J. Recent Advances in Transition-Metal Dichalcogenide Based Nanomaterials for Water Splitting. *Nanoscale* **2015**, *7* (47), 19764–19788. <https://doi.org/10.1039/C5NR06718A>.
- (14) Cobo, S.; Heidkamp, J.; Jacques, P.-A.; Fize, J.; Fourmond, V.; Guetaz, L.; Jusselme, B.; Ivanova, V.; Dau, H.; Palacin, S.; Fontecave, M.; Artero, V. A Janus Cobalt-Based Catalytic Material for Electro-Splitting of Water. *Nat. Mater.* **2012**, *11* (9), 802–807. <https://doi.org/10.1038/nmat3385>.

- (15) Steele, B. C. H.; Heinzl, A. *Materials for Fuel-Cell Technologies*. **2001**, *414*, 8.
- (16) Bockris, J. O. M.; Ammar, I. A.; Huq, A. K. M. S. The Mechanism of the Hydrogen Evolution Reaction on Platinum, Silver and Tungsten Surfaces in Acid Solutions. *J. Phys. Chem.* **1957**, *61* (7), 879–886. <https://doi.org/10.1021/j150553a008>.
- (17) Lee, Y.; Suntivich, J.; May, K. J.; Perry, E. E.; Shao-Horn, Y. Synthesis and Activities of Rutile IrO₂ and RuO₂ Nanoparticles for Oxygen Evolution in Acid and Alkaline Solutions. *J. Phys. Chem. Lett.* **2012**, *3* (3), 399–404. <https://doi.org/10.1021/jz2016507>.
- (18) Reier, T.; Oezaslan, M.; Strasser, P. Electrocatalytic Oxygen Evolution Reaction (OER) on Ru, Ir, and Pt Catalysts: A Comparative Study of Nanoparticles and Bulk Materials. *ACS Catal.* **2012**, *2* (8), 1765–1772. <https://doi.org/10.1021/cs3003098>.
- (19) Vuković, M. Oxygen Evolution Reaction on Thermally Treated Iridium Oxide Films. *J. Appl. Electrochem.* **1987**, *17* (4), 737–745. <https://doi.org/10.1007/BF01007809>.
- (20) *XPS Studies of Oxygen Evolution on Ru and RuO₂ Anodes*. <http://jes.ecsdl.org/content/130/4/825.short> (accessed 2019-08-01).
- (21) Antolini, E. Iridium As Catalyst and Cocatalyst for Oxygen Evolution/Reduction in Acidic Polymer Electrolyte Membrane Electrolyzers and Fuel Cells. *ACS Catal.* **2014**, *4* (5), 1426–1440. <https://doi.org/10.1021/cs4011875>.
- (22) *Anodic Iridium Oxide Films*. <http://jes.ecsdl.org/content/131/1/72.short> (accessed 2019-08-01).
- (23) Savéant, J. M.; Su, K. B. Homogeneous Redox Catalysis of Electrochemical Reaction: Part VI. Zone Diagram Representation of the Kinetic Regimes. *J. Electroanal. Chem. Interfacial Electrochem.* **1984**, *171* (1), 341–349. [https://doi.org/10.1016/0022-0728\(84\)80125-4](https://doi.org/10.1016/0022-0728(84)80125-4).
- (24) Weinstock, I. A.; Debye-smoluchowski, A.; Equation, B. M. *II. Outer-Sphere Electron-Transfer Reactions*; 1997.
- (25) Nocera, D. G. Chemistry of Personalized Solar Energy. *Inorg. Chem.* **2009**, *48* (21), 10001–10017. <https://doi.org/10.1021/ic901328v>.
- (26) Liu, F.; Concepcion, J. J.; Jurss, J. W.; Cardolaccia, T.; Templeton, J. L.; Meyer, T. J. Mechanisms of Water Oxidation from the Blue Dimer to Photosystem II. *Inorg. Chem.* **2008**, *47* (6), 1727–1752. <https://doi.org/10.1021/ic701249s>.
- (27) Costentin, C.; Robert, M.; Savéant, J.-M. Catalysis of the Electrochemical Reduction of Carbon Dioxide. *Chem. Soc. Rev.* **2013**, *42* (6), 2423–2436. <https://doi.org/10.1039/C2CS35360A>.
- (28) Li, C. W.; Ciston, J.; Kanan, M. W. Electroreduction of Carbon Monoxide to Liquid Fuel on Oxide-Derived Nanocrystalline Copper. *Nature* **2014**, *508* (7497), 504–507. <https://doi.org/10.1038/nature13249>.
- (29) Cukier, R. I.; Nocera, D. G. Proton-Coupled Electron Transfer. *Annu. Rev. Phys. Chem.* **1998**, *49* (1), 337–369. <https://doi.org/10.1146/annurev.physchem.49.1.337>.
- (30) Huynh, M. H. V.; Meyer, T. J. Proton-Coupled Electron Transfer. *Chem. Rev.* **2007**, *107* (11), 5004–5064. <https://doi.org/10.1021/cr0500030>.
- (31) Mayer, J. M. PROTON-COUPLED ELECTRON TRANSFER: A Reaction Chemist's View. *Annu. Rev. Phys. Chem.* **2004**, *55* (1), 363–390. <https://doi.org/10.1146/annurev.physchem.55.091602.094446>.
- (32) Hammarström Leif; Styring Stenbjörn. Coupled Electron Transfers in Artificial Photosynthesis. *Philos. Trans. R. Soc. B Biol. Sci.* **2008**, *363* (1494), 1283–1291. <https://doi.org/10.1098/rstb.2007.2225>.

- (33) Hammes-Schiffer, S.; Stuchebrukhov, A. A. Theory of Coupled Electron and Proton Transfer Reactions. *Chem. Rev.* **2010**, *110* (12), 6939–6960. <https://doi.org/10.1021/cr1001436>.
- (34) Dempsey, J. L.; Brunschwig, B. S.; Winkler, J. R.; Gray, H. B. Hydrogen Evolution Catalyzed by Cobaloximes. *Acc. Chem. Res.* **2009**, *42* (12), 1995–2004. <https://doi.org/10.1021/ar900253e>.
- (35) Tard, C.; Pickett, C. J. Structural and Functional Analogues of the Active Sites of the [Fe]-, [NiFe]-, and [FeFe]-Hydrogenases. *Chem. Rev.* **2009**, *109* (6), 2245–2274. <https://doi.org/10.1021/cr800542q>.
- (36) Le Goff, A.; Artero, V.; Jusselme, B.; Tran, P. D.; Guillet, N.; Métafé, R.; Fihri, A.; Palacin, S.; Fontecave, M. From Hydrogenases to Noble Metal-Free Catalytic Nanomaterials for H₂ Production and Uptake. *Science* **2009**, *326* (5958), 1384–1387. <https://doi.org/10.1126/science.1179773>.
- (37) Rakowski DuBois, M.; DuBois, D. L. The Roles of the First and Second Coordination Spheres in the Design of Molecular Catalysts for H₂ Production and Oxidation. *Chem Soc Rev* **2009**, *38* (1), 62–72. <https://doi.org/10.1039/B801197B>.
- (38) Rana, A.; Mondal, B.; Sen, P.; Dey, S.; Dey, A. Activating Fe(I) Porphyrins for the Hydrogen Evolution Reaction Using Second-Sphere Proton Transfer Residues. *Inorg. Chem.* **2017**, *56* (4), 1783–1793. <https://doi.org/10.1021/acs.inorgchem.6b01707>.
- (39) Castro-Cruz, H. M.; Macías-Ruvalcaba, N. A. Porphyrin-Catalyzed Electrochemical Hydrogen Evolution Reaction. Metal-Centered and Ligand-Centered Mechanisms. *Coord. Chem. Rev.* **2022**, *458*, 214430. <https://doi.org/10.1016/j.ccr.2022.214430>.
- (40) Wu, Z.-Y.; Wang, T.; Meng, Y.-S.; Rao, Y.; Wang, B.-W.; Zheng, J.; Gao, S.; Zhang, J.-L. Enhancing the Reactivity of Nickel(II) in Hydrogen Evolution Reactions (HERs) by β -Hydrogenation of Porphyrinoid Ligands. *Chem. Sci.* **2017**, *8* (9), 5953–5961. <https://doi.org/10.1039/C7SC02073B>.
- (41) Han, Y.; Fang, H.; Jing, H.; Sun, H.; Lei, H.; Lai, W.; Cao, R. Singly versus Doubly Reduced Nickel Porphyrins for Proton Reduction: Experimental and Theoretical Evidence for a Homolytic Hydrogen-Evolution Reaction. *Angew. Chem. Int. Ed.* **2016**, *55* (18), 5457–5462. <https://doi.org/10.1002/anie.201510001>.
- (42) Manton, J. C.; Hidalgo, D.; Frayne, L.; Brandon, M. P.; Vos, J. G.; Pryce, M. T. Electrocatalytic Hydrogen Evolution Using Metal-Free Porphyrins. *Int. J. Hydrog. Energy* **2018**, *43* (41), 18843–18849. <https://doi.org/10.1016/j.ijhydene.2018.08.017>.
- (43) Wu, Y.; Rodríguez-López, N.; Villagrán, D. Hydrogen Gas Generation Using a Metal-Free Fluorinated Porphyrin. *Chem. Sci.* **2018**, *9* (20), 4689–4695. <https://doi.org/10.1039/C8SC00093J>.
- (44) Anderson, H. L. Conjugated Porphyrin Ladders. *Inorg. Chem.* **1994**, *33* (5), 972–981. <https://doi.org/10.1021/ic00083a022>.
- (45) Abe, T.; Taguchi, F.; Imai, H.; Zhao, F.; Zhang, J.; Kaneko, M. Highly Active Electrocatalysis by Cobalt Tetraphenylporphyrin Incorporated in a Nafion Membrane for Proton Reduction. *Polym. Adv. Technol.* **1998**, *9* (9), 559–562. [https://doi.org/10.1002/\(SICI\)1099-1581\(199809\)9:9<559::AID-PAT818>3.0.CO;2-1](https://doi.org/10.1002/(SICI)1099-1581(199809)9:9<559::AID-PAT818>3.0.CO;2-1).
- (46) Bhugun, I.; Lexa, D.; Savéant, J.-M. Homogeneous Catalysis of Electrochemical Hydrogen Evolution by Iron(0) Porphyrins. *J. Am. Chem. Soc.* **1996**, *118* (16), 3982–3983. <https://doi.org/10.1021/ja954326x>.

- (47) Grass, V.; Lexa, D.; Savéant, J.-M. Electrochemical Generation of Rhodium Porphyrin Hydrides. Catalysis of Hydrogen Evolution. *J. Am. Chem. Soc.* **1997**, *119* (32), 7526–7532. <https://doi.org/10.1021/ja964100+>.
- (48) Lee, C. H.; Dogutan, D. K.; Nocera, D. G. Hydrogen Generation by Hangman Metalloporphyrins. *J. Am. Chem. Soc.* **2011**, *133* (23), 8775–8777. <https://doi.org/10.1021/ja202136y>.
- (49) Zhang, W.; Lai, W.; Cao, R. Energy-Related Small Molecule Activation Reactions: Oxygen Reduction and Hydrogen and Oxygen Evolution Reactions Catalyzed by Porphyrin- and Corrole-Based Systems. *Chem. Rev.* **2017**, *117* (4), 3717–3797. <https://doi.org/10.1021/acs.chemrev.6b00299>.
- (50) Bediako, D. K.; Solis, B. H.; Dogutan, D. K.; Roubelakis, M. M.; Maher, A. G.; Lee, C. H.; Chambers, M. B.; Hammes-Schiffer, S.; Nocera, D. G. Role of Pendant Proton Relays and Proton-Coupled Electron Transfer on the Hydrogen Evolution Reaction by Nickel Hangman Porphyrins. *Proc. Natl. Acad. Sci.* **2014**, *111* (42), 15001–15006. <https://doi.org/10.1073/pnas.1414908111>.
- (51) Zhang, Y.-Q.; Liao, R.-Z. Reaction Mechanism of Hydrogen Evolution Catalysed by Co and Fe Complexes Containing a Tetra-Dentate Phosphine Ligand – a DFT Study. *Phys. Chem. Chem. Phys.* **2017**, *19* (48), 32589–32596. <https://doi.org/10.1039/C7CP06222B>.
- (52) Wurster, B.; Grumelli, D.; Hötger, D.; Gutzler, R.; Kern, K. Driving the Oxygen Evolution Reaction by Nonlinear Cooperativity in Bimetallic Coordination Catalysts. *J. Am. Chem. Soc.* **2016**, *138* (11), 3623–3626. <https://doi.org/10.1021/jacs.5b10484>.
- (53) Naruta, Y.; Sasayama, M.; Sasaki, T. Oxygen Evolution by Oxidation of Water with Manganese Porphyrin Dimers. *Angew. Chem. Int. Ed. Engl.* **1994**, *33* (18), 1839–1841. <https://doi.org/10.1002/anie.199418391>.
- (54) Cui, S.; Qian, M.; Liu, X.; Sun, Z.; Du, P. A Copper Porphyrin-Based Conjugated Mesoporous Polymer-Derived Bifunctional Electrocatalyst for Hydrogen and Oxygen Evolution. *ChemSusChem* **2016**, *9* (17), 2365–2373. <https://doi.org/10.1002/cssc.201600452>.
- (55) Holm, R. H. Metal-Centered Oxygen Atom Transfer Reactions. *Chem. Rev.* **1987**, *87* (6), 1401–1449. <https://doi.org/10.1021/cr00082a005>.
- (56) Cheng, M.-J.; Head-Gordon, M.; Bell, A. T. How to Chemically Tailor Metal-Porphyrin-Like Active Sites on Carbon Nanotubes and Graphene for Minimal Overpotential in the Electrochemical Oxygen Evolution and Oxygen Reduction Reactions. *J. Phys. Chem. C* **2014**, *118* (51), 29482–29491. <https://doi.org/10.1021/jp507638v>.
- (57) Bhugun, I.; Lexa, D.; Savéant, J.-M. Catalysis of the Electrochemical Reduction of Carbon Dioxide by Iron(0) Porphyrins: Synergistic Effect of Weak Brønsted Acids. *J. Am. Chem. Soc.* **1996**, *118* (7), 1769–1776. <https://doi.org/10.1021/ja9534462>.
- (58) Patra, B. C.; Khilari, S.; Manna, R. N.; Mondal, S.; Pradhan, D.; Pradhan, A.; Bhaumik, A. A Metal-Free Covalent Organic Polymer for Electrocatalytic Hydrogen Evolution. *ACS Catal.* **2017**, *7* (9), 6120–6127. <https://doi.org/10.1021/acscatal.7b01067>.
- (59) Swierk, J. R.; Méndez-Hernández, D. D.; McCool, N. S.; Liddell, P.; Terazono, Y.; Pahk, I.; Tomlin, J. J.; Oster, N. V.; Moore, T. A.; Moore, A. L.; Gust, D.; Mallouk, T. E. Metal-Free Organic Sensitizers for Use in Water-Splitting Dye-Sensitized Photoelectrochemical Cells. *Proc. Natl. Acad. Sci.* **2015**, *112* (6), 1681–1686. <https://doi.org/10.1073/pnas.1414901112>.

- (60) Medforth, C. J.; Senge, M. O.; Smith, K. M.; Sparks, L. D.; Shelnut, J. A. Nonplanar Distortion Modes for Highly Substituted Porphyrins. *J. Am. Chem. Soc.* **1992**, *114* (25), 9859–9869. <https://doi.org/10.1021/ja00051a019>.
- (61) Ito, A.; Konishi, K.; Aida, T. Free Bases of Chiral N-Substituted Porphyrins as Catalysts for Asymmetric Reaction. *Tetrahedron Lett.* **1996**, *37* (15), 2585–2588. [https://doi.org/10.1016/0040-4039\(96\)00376-0](https://doi.org/10.1016/0040-4039(96)00376-0).
- (62) Feng, D.-M.; Zhu, Y.-P.; Chen, P.; Ma, T.-Y. Recent Advances in Transition-Metal-Mediated Electrocatalytic CO₂ Reduction: From Homogeneous to Heterogeneous Systems. *Catalysts* **2017**, *7* (12), 373. <https://doi.org/10.3390/catal7120373>.
- (63) Bala Murali Krishna, M.; Venkatramaiah, N.; Venkatesan, R.; Narayana Rao, D. Synthesis and Structural, Spectroscopic and Nonlinear Optical Measurements of Graphene Oxide and Its Composites with Metal and Metal Free Porphyrins. *J. Mater. Chem.* **2012**, *22* (7), 3059. <https://doi.org/10.1039/c1jm14822b>.
- (64) Yeager, M. P.; Hoffman, C. M.; Xia, Z.; Trexler, M. M. Method for the Synthesis of *Para*-Aramid Nanofibers. *J. Appl. Polym. Sci.* **2016**, *133* (42). <https://doi.org/10.1002/app.44082>.
- (65) Bhunia, S.; Das, S. K.; Jana, R.; Peter, S. C.; Bhattacharya, S.; Addicoat, M.; Bhaumik, A.; Pradhan, A. Electrochemical Stimuli-Driven Facile Metal-Free Hydrogen Evolution from Pyrene-Porphyrin-Based Crystalline Covalent Organic Framework. *ACS Appl. Mater. Interfaces* **2017**, *9* (28), 23843–23851. <https://doi.org/10.1021/acsami.7b06968>.
- (66) Sun, J.; Yin, H.; Liu, P.; Wang, Y.; Yao, X.; Tang, Z.; Zhao, H. Molecular Engineering of Ni/Co-Porphyrin Multilayers on Reduced Graphene Oxide Sheets as Bifunctional Catalysts for Oxygen Evolution and Oxygen Reduction Reactions. *Chem. Sci.* **2016**, *7* (9), 5640–5646. <https://doi.org/10.1039/C6SC02083F>.
- (67) Xiang, Q.; Li, F.; Chen, W.; Ma, Y.; Wu, Y.; Gu, X.; Qin, Y.; Tao, P.; Song, C.; Shang, W.; Zhu, H.; Deng, T.; Wu, J. In Situ Vertical Growth of Fe–Ni Layered Double-Hydroxide Arrays on Fe–Ni Alloy Foil: Interfacial Layer Enhanced Electrocatalyst with Small Overpotential for Oxygen Evolution Reaction. *ACS Energy Lett.* **2018**, *3* (10), 2357–2365. <https://doi.org/10.1021/acseenergylett.8b01466>.
- (68) Hu, C.; Dai, L. Multifunctional Carbon-Based Metal-Free Electrocatalysts for Simultaneous Oxygen Reduction, Oxygen Evolution, and Hydrogen Evolution. *Adv. Mater.* **2017**, *29* (9), 1604942. <https://doi.org/10.1002/adma.201604942>.
- (69) Chang, B.-Y.; Park, S.-M. Electrochemical Impedance Spectroscopy. *Annu. Rev. Anal. Chem.* **2010**, *3* (1), 207–229. <https://doi.org/10.1146/annurev.anchem.012809.102211>.
- (70) Lasia, A. Electrochemical Impedance Spectroscopy and Its Applications. In *Modern Aspects of Electrochemistry*; Conway, B. E., Bockris, J. O., White, R. E., Eds.; Modern Aspects of Electrochemistry; Springer US: Boston, MA, 2002; pp 143–248. https://doi.org/10.1007/0-306-46916-2_2.
- (71) Zhu, Y.; Zhou, W.; Zhong, Y.; Bu, Y.; Chen, X.; Zhong, Q.; Liu, M.; Shao, Z. A Perovskite Nanorod as Bifunctional Electrocatalyst for Overall Water Splitting. *Adv. Energy Mater.* **2017**, *7* (8), 1602122. <https://doi.org/10.1002/aenm.201602122>.
- (72) Fang, Y.-H.; Liu, Z.-P. Tafel Kinetics of Electrocatalytic Reactions: From Experiment to First-Principles. *ACS Catal.* **2014**, *4* (12), 4364–4376. <https://doi.org/10.1021/cs501312v>.
- (73) Shinagawa, T.; Garcia-Esparza, A. T.; Takanabe, K. Insight on Tafel Slopes from a Microkinetic Analysis of Aqueous Electrocatalysis for Energy Conversion. *Sci. Rep.* **2015**, *5* (1). <https://doi.org/10.1038/srep13801>.

- (74) Ding, H.; Liu, H.; Chu, W.; Wu, C.; Xie, Y. Structural Transformation of Heterogeneous Materials for Electrocatalytic Oxygen Evolution Reaction. *Chem. Rev.* **2021**, *121* (21), 13174–13212. <https://doi.org/10.1021/acs.chemrev.1c00234>.
- (75) Fang, Y.; Hou, Y.; Fu, X.; Wang, X. Semiconducting Polymers for Oxygen Evolution Reaction under Light Illumination. *Chem. Rev.* **2022**, *122* (3), 4204–4256. <https://doi.org/10.1021/acs.chemrev.1c00686>.
- (76) Kolb, M. J.; Calle-Vallejo, F.; Juurlink, L. B. F.; Koper, M. T. M. Density Functional Theory Study of Adsorption of H₂O, H, O, and OH on Stepped Platinum Surfaces. *J. Chem. Phys.* **2014**, *140* (13), 134708. <https://doi.org/10.1063/1.4869749>.
- (77) Jiang, Z.; Fang, T. DFT Study on the Synergistic Effect of Pd–Cu Bimetal on the Adsorption and Dissociation of H₂O. *J. Phys. Chem. C* **2016**, *120* (44), 25289–25295. <https://doi.org/10.1021/acs.jpcc.6b05274>.
- (78) Chen, P.; Tong, Y.; Wu, C.; Xie, Y. Surface/Interfacial Engineering of Inorganic Low-Dimensional Electrode Materials for Electrocatalysis. *Acc. Chem. Res.* **2018**, *51* (11), 2857–2866. <https://doi.org/10.1021/acs.accounts.8b00266>.
- (79) Nong, H. N.; Gan, L.; Willinger, E.; Teschner, D.; Strasser, P. IrOx Core-Shell Nanocatalysts for Cost- and Energy-Efficient Electrochemical Water Splitting. *Chem Sci* **2014**, *5* (8), 2955–2963. <https://doi.org/10.1039/C4SC01065E>.
- (80) Doyle, R. L.; Godwin, I. J.; Brandon, M. P.; Lyons, M. E. G. Redox and Electrochemical Water Splitting Catalytic Properties of Hydrated Metal Oxide Modified Electrodes. *Phys. Chem. Chem. Phys.* **2013**, *15* (33), 13737. <https://doi.org/10.1039/c3cp51213d>.
- (81) Roy, S.; Bagchi, D.; Dheer, L.; Sarma, S. Ch.; Rajaji, V.; Narayana, C.; Waghmare, U. V.; Peter, S. C. Mechanistic Insights into the Promotional Effect of Ni Substitution in Non-Noble Metal Carbides for Highly Enhanced Water Splitting. *Appl. Catal. B Environ.* **2021**, *298*, 120560. <https://doi.org/10.1016/j.apcatb.2021.120560>.
- (82) Chen, P.; Ye, J.; Wang, H.; Ouyang, L.; Zhu, M. Recent Progress of Transition Metal Carbides/Nitrides for Electrocatalytic Water Splitting. *J. Alloys Compd.* **2021**, *883*, 160833. <https://doi.org/10.1016/j.jallcom.2021.160833>.
- (83) Hunter, B. M.; Gray, H. B.; Müller, A. M. Earth-Abundant Heterogeneous Water Oxidation Catalysts. *Chem. Rev.* **2016**, *116* (22), 14120–14136. <https://doi.org/10.1021/acs.chemrev.6b00398>.
- (84) Han, A.; Wu, H.; Sun, Z.; Jia, H.; Yan, Z.; Ma, H.; Liu, X.; Du, P. Green Cobalt Oxide (CoO_x) Film with Nanoribbon Structures Electrodeposited from the BF₂-Annulated Cobaloxime Precursor for Efficient Water Oxidation. *ACS Appl. Mater. Interfaces* **2014**, *6* (14), 10929–10934. <https://doi.org/10.1021/am500830z>.
- (85) Tagore, R.; Crabtree, R. H.; Brudvig, G. W. Oxygen Evolution Catalysis by a Dimanganese Complex and Its Relation to Photosynthetic Water Oxidation. *Inorg. Chem.* **2008**, *47* (6), 1815–1823. <https://doi.org/10.1021/ic062218d>.
- (86) Dogutan, D. K.; McGuire, R.; Nocera, D. G. Electrocatalytic Water Oxidation by Cobalt(III) Hangman β -Octafluoro Corroles. *J. Am. Chem. Soc.* **2011**, *133* (24), 9178–9180. <https://doi.org/10.1021/ja202138m>.
- (87) Vij, V.; Sultan, S.; Harzandi, A. M.; Meena, A.; Tiwari, J. N.; Lee, W.-G.; Yoon, T.; Kim, K. S. Nickel-Based Electrocatalysts for Energy-Related Applications: Oxygen Reduction, Oxygen Evolution, and Hydrogen Evolution Reactions. *ACS Catal.* **2017**, *7* (10), 7196–7225. <https://doi.org/10.1021/acscatal.7b01800>.

- (88) Yu, X.; Hua, T.; Liu, X.; Yan, Z.; Xu, P.; Du, P. Nickel-Based Thin Film on Multiwalled Carbon Nanotubes as an Efficient Bifunctional Electrocatalyst for Water Splitting. *ACS Appl. Mater. Interfaces* **2014**, *6* (17), 15395–15402. <https://doi.org/10.1021/am503938c>.
- (89) Fillol, J. L.; Codolà, Z.; Garcia-Bosch, I.; Gómez, L.; Pla, J. J.; Costas, M. Efficient Water Oxidation Catalysts Based on Readily Available Iron Coordination Complexes. *Nat. Chem.* **2011**, *3* (10), 807–813. <https://doi.org/10.1038/nchem.1140>.
- (90) Codolà, Z.; Gómez, L.; Kleespies, S. T.; Que Jr, L.; Costas, M.; Lloret-Fillol, J. Evidence for an Oxygen Evolving Iron–Oxo–Cerium Intermediate in Iron-Catalysed Water Oxidation. *Nat. Commun.* **2015**, *6* (1), 5865. <https://doi.org/10.1038/ncomms6865>.
- (91) Mirzakulova, E.; Khatmullin, R.; Walpita, J.; Corrigan, T.; Vargas-Barbosa, N. M.; Vyas, S.; Oottikkal, S.; Manzer, S. F.; Hadad, C. M.; Glusac, K. D. Electrode-Assisted Catalytic Water Oxidation by a Flavin Derivative. *Nat. Chem.* **2012**, *4* (10), 794–801. <https://doi.org/10.1038/nchem.1439>.
- (92) Meng, J.; Zhou, Y.; Chi, H.; Li, K.; Wan, J.; Hu, Z. Bimetallic Porphyrin MOF Anchored onto RGO Nanosheets as a Highly Efficient 2D Electrocatalyst for Oxygen Evolution Reaction in Alkaline Conditions. *ChemistrySelect* **2019**, *4* (29), 8661–8670. <https://doi.org/10.1002/slct.201901713>.
- (93) Zhang, X.; Wasson, M. C.; Shayan, M.; Berdichevsky, E. K.; Ricardo-Noordberg, J.; Singh, Z.; Papazyan, E. K.; Castro, A. J.; Marino, P.; Ajoyan, Z.; Chen, Z.; Islamoglu, T.; Howarth, A. J.; Liu, Y.; Majewski, M. B.; Katz, M. J.; Mondloch, J. E.; Farha, O. K. A Historical Perspective on Porphyrin-Based Metal–Organic Frameworks and Their Applications. *Coord. Chem. Rev.* **2021**, *429*, 213615. <https://doi.org/10.1016/j.ccr.2020.213615>.
- (94) Jia, H.; Yao, Y.; Gao, Y.; Lu, D.; Du, P. Pyrolyzed Cobalt Porphyrin-Based Conjugated Mesoporous Polymers as Bifunctional Catalysts for Hydrogen Production and Oxygen Evolution in Water. *Chem. Commun.* **2016**, *52* (92), 13483–13486. <https://doi.org/10.1039/C6CC06972J>.
- (95) Lin, C.-Y.; Zhang, D.; Zhao, Z.; Xia, Z. Covalent Organic Framework Electrocatalysts for Clean Energy Conversion. *Adv. Mater.* **2018**, *30* (5), 1703646. <https://doi.org/10.1002/adma.201703646>.
- (96) Huang, S.; Chen, K.; Li, T.-T. Porphyrin and Phthalocyanine Based Covalent Organic Frameworks for Electrocatalysis. *Coord. Chem. Rev.* **2022**, *464*, 214563. <https://doi.org/10.1016/j.ccr.2022.214563>.
- (97) Yuan, J.; Chen, S.; Zhang, Y.; Li, R.; Zhang, J.; Peng, T. Structural Regulation of Coupled Phthalocyanine–Porphyrin Covalent Organic Frameworks to Highly Active and Selective Electrocatalytic CO₂ Reduction. *Adv. Mater.* **2022**, *34* (30), 2203139. <https://doi.org/10.1002/adma.202203139>.
- (98) Huang, Z.; Zhang, M.; Lin, H.; Ding, S.; Dong, B.; Liu, D.; Wang, H.; Dai, F.; Sun, D. Comparison of Two Water Oxidation Electrocatalysts by Copper or Zinc Supermolecule Complexes Based on Porphyrin Ligand. *RSC Adv.* **2018**, *8* (70), 40054–40059. <https://doi.org/10.1039/C8RA08338J>.
- (99) Li, B.-Q.; Zhao, C.-X.; Chen, S.; Liu, J.-N.; Chen, X.; Song, L.; Zhang, Q. Framework-Porphyrin-Derived Single-Atom Bifunctional Oxygen Electrocatalysts and Their Applications in Zn–Air Batteries. *Adv. Mater.* **2019**, *31* (19), 1900592. <https://doi.org/10.1002/adma.201900592>.

- (100) Wang, A.; Cheng, L.; Shen, X.; Chen, X.; Zhu, W.; Zhao, W.; Lv, C. Porphyrin Coordination Polymer/Co1-xS Composite Electrocatalyst for Efficient Oxygen Evolution Reaction. *Chem. Eng. J.* **2020**, *400*, 125975. <https://doi.org/10.1016/j.cej.2020.125975>.
- (101) Kuposova, E.; Liu, X.; Pendin, A.; Thiele, B.; Shumilova, G.; Ermolenko, Y.; Offenhäusser, A.; Mourzina, Y. Influence of Meso-Substitution of the Porphyrin Ring on Enhanced Hydrogen Evolution in a Photochemical System. *J. Phys. Chem. C* **2016**, *120* (26), 13873–13890. <https://doi.org/10.1021/acs.jpcc.6b01467>.
- (102) Beyene, B. B.; Mane, S. B.; Hung, C.-H. Electrochemical Hydrogen Evolution by Cobalt (II) Porphyrins: Effects of Ligand Modification on Catalytic Activity, Efficiency and Overpotential. *J. Electrochem. Soc.* **2018**, *165* (9), H481–H487. <https://doi.org/10.1149/2.0481809jes>.
- (103) Heppe, N.; Gallenkamp, C.; Paul, S.; Segura-Salas, N.; von Rhein, N.; Kaiser, B.; Jaegermann, W.; Jafari, A.; Sergeev, I.; Krewald, V.; Kramm, U. I. *Substituent Effects in Iron Porphyrin Catalysts for the Hydrogen Evolution Reaction*; preprint; Chemistry, 2022. <https://doi.org/10.26434/chemrxiv-2022-x76g3>.
- (104) Lazarides, T.; Delor, M.; V. Sazanovich, I.; M. McCormick, T.; Georgakaki, I.; Charalambidis, G.; A. Weinstein, J.; G. Coutsolelos, A. Photocatalytic Hydrogen Production from a Noble Metal Free System Based on a Water Soluble Porphyrin Derivative and a Cobaloxime Catalyst. *Chem. Commun.* **2014**, *50* (5), 521–523. <https://doi.org/10.1039/C3CC45025B>.
- (105) Han, Y.; Wu, Y.; Lai, W.; Cao, R. Electrocatalytic Water Oxidation by a Water-Soluble Nickel Porphyrin Complex at Neutral PH with Low Overpotential. *Inorg. Chem.* **2015**, *54* (11), 5604–5613. <https://doi.org/10.1021/acs.inorgchem.5b00924>.
- (106) Li, X.; Zhang, X.-P.; Guo, M.; Lv, B.; Guo, K.; Jin, X.; Zhang, W.; Lee, Y.-M.; Fukuzumi, S.; Nam, W.; Cao, R. Identifying Intermediates in Electrocatalytic Water Oxidation with a Manganese Corrole Complex. *J. Am. Chem. Soc.* **2021**, *143* (36), 14613–14621. <https://doi.org/10.1021/jacs.1c05204>.
- (107) Xie, L.; Zhang, X.-P.; Zhao, B.; Li, P.; Qi, J.; Guo, X.; Wang, B.; Lei, H.; Zhang, W.; Apfel, U.-P.; Cao, R. Enzyme-Inspired Iron Porphyrins for Improved Electrocatalytic Oxygen Reduction and Evolution Reactions. *Angew. Chem.* **2021**, *133* (14), 7654–7659. <https://doi.org/10.1002/ange.202015478>.
- (108) Zhang, R.; Warren, J. J. Controlling the Oxygen Reduction Selectivity of Asymmetric Cobalt Porphyrins by Using Local Electrostatic Interactions. *J. Am. Chem. Soc.* **2020**, *142* (31), 13426–13434. <https://doi.org/10.1021/jacs.0c03861>.
- (109) Levy, N.; Mahammed, A.; Kosa, M.; Major, D. T.; Gross, Z.; Elbaz, L. Metalloporroles as Nonprecious-Metal Catalysts for Oxygen Reduction. *Angew. Chem. Int. Ed.* **2015**, *54* (47), 14080–14084. <https://doi.org/10.1002/anie.201505236>.
- (110) Nam, W.; Lee, Y.-M.; Fukuzumi, S. Tuning Reactivity and Mechanism in Oxidation Reactions by Mononuclear Nonheme Iron(IV)-Oxo Complexes. *Acc. Chem. Res.* **2014**, *47* (4), 1146–1154. <https://doi.org/10.1021/ar400258p>.
- (111) Okamura, M.; Kondo, M.; Kuga, R.; Kurashige, Y.; Yanai, T.; Hayami, S.; Praneeth, V. K. K.; Yoshida, M.; Yoneda, K.; Kawata, S.; Masaoka, S. A Pentanuclear Iron Catalyst Designed for Water Oxidation. *Nature* **2016**, *530* (7591), 465–468. <https://doi.org/10.1038/nature16529>.

- (112) de Oliveira, F. T.; Chanda, A.; Banerjee, D.; Shan, X.; Mondal, S.; Que, L.; Bominaar, E. L.; Münck, E.; Collins, T. J. Chemical and Spectroscopic Evidence for an FeV-Oxo Complex. *Science* **2007**, *315* (5813), 835–838. <https://doi.org/10.1126/science.1133417>.
- (113) Yao, B.; He, Y.; Wang, S.; Sun, H.; Liu, X. Recent Advances in Porphyrin-Based Systems for Electrochemical Oxygen Evolution Reaction. *Int. J. Mol. Sci.* **2022**, *23* (11), 6036. <https://doi.org/10.3390/ijms23116036>.
- (114) Li, J.; Zhang, Y.; Kornienko, N. Heterogeneous Electrocatalytic Reduction of CO₂ Promoted by Secondary Coordination Sphere Effects. *New J. Chem.* **2020**, *44* (11), 4246–4252. <https://doi.org/10.1039/C9NJ05892C>.
- (115) Chen, A.; Zhang, Y.; Chen, J.; Chen, L.; Yu, Y. Metalloporphyrin-Based Organic Polymers for Carbon Dioxide Fixation to Cyclic Carbonate. *J. Mater. Chem. A* **2015**, *3* (18), 9807–9816. <https://doi.org/10.1039/C5TA00993F>.
- (116) Helveg, S.; Lauritsen, J. V.; Lægsgaard, E.; Stensgaard, I.; Nørskov, J. K.; Clausen, B. S.; Topsøe, H.; Besenbacher, F. Atomic-Scale Structure of Single-Layer $\{\mathrm{MoS}\}_2$ Nanoclusters. *Phys. Rev. Lett.* **2000**, *84* (5), 951–954. <https://doi.org/10.1103/PhysRevLett.84.951>.
- (117) Bag, S.; Gaudette, A. F.; Bussell, M. E.; Kanatzidis, M. G. Spongy Chalcogels of Non-Platinum Metals Act as Effective Hydrodesulfurization Catalysts. *Nat. Chem.* **2009**, *1* (3), 217–224. <https://doi.org/10.1038/nchem.208>.
- (118) Cheng, F. Y.; Chen, J.; Gou, X. L. MoS₂–Ni Nanocomposites as Catalysts for Hydrodesulfurization of Thiophene and Thiophene Derivatives. *Adv. Mater.* **2006**, *18* (19), 2561–2564. <https://doi.org/10.1002/adma.200600912>.
- (119) Benck, J. D.; Chen, Z.; Kuritzky, L. Y.; Forman, A. J.; Jaramillo, T. F. Amorphous Molybdenum Sulfide Catalysts for Electrochemical Hydrogen Production: Insights into the Origin of Their Catalytic Activity. *ACS Catal.* **2012**, *2* (9), 1916–1923. <https://doi.org/10.1021/cs300451q>.
- (120) Voiry, D.; Salehi, M.; Silva, R.; Fujita, T.; Chen, M.; Asefa, T.; Shenoy, V. B.; Eda, G.; Chhowalla, M. Conducting MoS₂ Nanosheets as Catalysts for Hydrogen Evolution Reaction. *Nano Lett.* **2013**, *13* (12), 6222–6227. <https://doi.org/10.1021/nl403661s>.
- (121) Xie, J.; Zhang, H.; Li, S.; Wang, R.; Sun, X.; Zhou, M.; Zhou, J.; Lou, X. W. (David); Xie, Y. Defect-Rich MoS₂ Ultrathin Nanosheets with Additional Active Edge Sites for Enhanced Electrocatalytic Hydrogen Evolution. *Adv. Mater.* **2013**, *25* (40), 5807–5813. <https://doi.org/10.1002/adma.201302685>.
- (122) Liu, Q.; Fang, Q.; Chu, W.; Wan, Y.; Li, X.; Xu, W.; Habib, M.; Tao, S.; Zhou, Y.; Liu, D.; Xiang, T.; Khalil, A.; Wu, X.; Chhowalla, M.; Ajayan, P. M.; Song, L. Electron-Doped 1T-MoS₂ via Interface Engineering for Enhanced Electrocatalytic Hydrogen Evolution. *Chem. Mater.* **2017**, *29* (11), 4738–4744. <https://doi.org/10.1021/acs.chemmater.7b00446>.
- (123) Yan, K.; Lu, Y. Direct Growth of MoS₂ Microspheres on Ni Foam as a Hybrid Nanocomposite Efficient for Oxygen Evolution Reaction. *Small* **2016**, *12* (22), 2975–2981. <https://doi.org/10.1002/sml.201600332>.
- (124) Hinnemann, B.; Moses, P. G.; Bonde, J.; Jørgensen, K. P.; Nielsen, J. H.; Horch, S.; Chorkendorff, I.; Nørskov, J. K. Biomimetic Hydrogen Evolution: MoS₂ Nanoparticles as Catalyst for Hydrogen Evolution. *J. Am. Chem. Soc.* **2005**, *127* (15), 5308–5309. <https://doi.org/10.1021/ja0504690>.
- (125) Javaid, S.; Xu, X.; Chen, W.; Chen, J.; Hsu, H.-Y.; Wang, S.; Yang, X.; Li, Y.; Shao, Z.; Jones, F.; Jia, G. Ni²⁺/Co²⁺ Doped Au-Fe₇S₈ Nanoplatelets with Exceptionally High

- Oxygen Evolution Reaction Activity. *Nano Energy* **2021**, *89*, 106463. <https://doi.org/10.1016/j.nanoen.2021.106463>.
- (126) Deng, J.; Yuan, W.; Ren, P.; Wang, Y.; Deng, D.; Zhang, Z.; Bao, X. High-Performance Hydrogen Evolution Electrocatalysis by Layer-Controlled MoS₂ Nanosheets. *RSC Adv.* **2014**, *4* (66), 34733–34738. <https://doi.org/10.1039/C4RA05614K>.
- (127) Wu, Z.; Nie, D.; Song, M.; Jiao, T.; Fu, G.; Liu, X. Facile Synthesis of Co–Fe–B–P Nanochains as an Efficient Bifunctional Electrocatalyst for Overall Water-Splitting. *Nanoscale* **2019**, *11* (15), 7506–7512. <https://doi.org/10.1039/C9NR01794A>.
- (128) Chen, Z.; Liu, D.; Gao, Y.; Zhao, Y.; Xiao, W.; Xu, G.; Ma, T.; Wu, Z.; Wang, L. Corrosive-Coordinate Engineering to Construct 2D-3D Nanostructure with Trace Pt as Efficient Bifunctional Electrocatalyst for Overall Water Splitting. *Sci. China Mater.* **2022**, *65* (5), 1217–1224. <https://doi.org/10.1007/s40843-021-1943-5>.
- (129) Xu, X.; Sun, H.; Jiang, S. P.; Shao, Z. Modulating Metal–Organic Frameworks for Catalyzing Acidic Oxygen Evolution for Proton Exchange Membrane Water Electrolysis. *SusMat* **2021**, *1* (4), 460–481. <https://doi.org/10.1002/sus2.34>.
- (130) Xu, X.; Su, C.; Shao, Z. Fundamental Understanding and Application of Ba_{0.5}Sr_{0.5}Co_{0.8}Fe_{0.2}O_{3-δ} Perovskite in Energy Storage and Conversion: Past, Present, and Future. *Energy Fuels* **2021**, *35* (17), 13585–13609. <https://doi.org/10.1021/acs.energyfuels.1c02111>.
- (131) Xiong, Q.; Wang, Y.; Liu, P.-F.; Zheng, L.-R.; Wang, G.; Yang, H.-G.; Wong, P.-K.; Zhang, H.; Zhao, H. Cobalt Covalent Doping in MoS₂ to Induce Bifunctionality of Overall Water Splitting. *Adv. Mater.* **2018**, *30* (29), 1801450. <https://doi.org/10.1002/adma.201801450>.
- (132) Wu, Y.; Li, F.; Chen, W.; Xiang, Q.; Ma, Y.; Zhu, H.; Tao, P.; Song, C.; Shang, W.; Deng, T.; Wu, J. Coupling Interface Constructions of MoS₂/Fe₅Ni₄S₈ Heterostructures for Efficient Electrochemical Water Splitting. *Adv. Mater.* **2018**, *30* (38), 1803151. <https://doi.org/10.1002/adma.201803151>.
- (133) Zhang, J.; Wang, T.; Pohl, D.; Rellinghaus, B.; Dong, R.; Liu, S.; Zhuang, X.; Feng, X. Interface Engineering of MoS₂/Ni₃S₂ Heterostructures for Highly Enhanced Electrochemical Overall-Water-Splitting Activity. *Angew. Chem. Int. Ed.* **2016**, *55* (23), 6702–6707. <https://doi.org/10.1002/anie.201602237>.
- (134) Jaramillo, T. F.; Jorgensen, K. P.; Bonde, J.; Nielsen, J. H.; Horch, S.; Chorkendorff, I. Identification of Active Edge Sites for Electrochemical H₂ Evolution from MoS₂ Nanocatalysts. *Science* **2007**, *317* (5834), 100–102. <https://doi.org/10.1126/science.1141483>.
- (135) Chang, K.; Hai, X.; Pang, H.; Zhang, H.; Shi, L.; Liu, G.; Liu, H.; Zhao, G.; Li, M.; Ye, J. Targeted Synthesis of 2H- and 1T-Phase MoS₂ Monolayers for Catalytic Hydrogen Evolution. *Adv. Mater.* **2016**, *28* (45), 10033–10041. <https://doi.org/10.1002/adma.201603765>.
- (136) Wimonrat Trakarnpruk; Seentrakoon, B.; Porntangjitlikit, S. Hydrodesulfurization of Diesel Oils by MoS₂ Catalyst Prepared by in Situ Decomposition of Ammonium Thiomolybdate. *Sci. Eng. Health Stud. FORMER NAME SILPAKORN Univ. Sci. Technol. J.* **2008**, *7*–13. <https://doi.org/10.14456/sustj.2008.1>.
- (137) Alonso, G.; Del Valle, M.; Cruz, J.; Petranovskii, V.; Licea-Claverie, A.; Fuentes, S. Preparation of MoS₂ Catalysts by in Situ Decomposition of Tetraalkylammonium

- Thiomolybdates. *Catal. Today* **1998**, *43* (1), 117–122. [https://doi.org/10.1016/S0920-5861\(98\)00140-0](https://doi.org/10.1016/S0920-5861(98)00140-0).
- (138) Yu, W.; Chen, Z.; Zhao, Y.; Gao, Y.; Xiao, W.; Dong, B.; Wu, Z.; Wang, L. An *in Situ* Generated 3D Porous Nanostructure on 2D Nanosheets to Boost the Oxygen Evolution Reaction for Water-Splitting. *Nanoscale* **2022**, *14* (12), 4566–4572. <https://doi.org/10.1039/D1NR08007E>.
- (139) Wu, Y.; Zarei-Chaleshtori, M.; Torres, B.; Akter, T.; Diaz-Moreno, C.; Saupe, G. B.; Lopez, J. A.; Chianelli, R. R.; Villagrán, D. Electrocatalytic Hydrogen Gas Generation by Cobalt Molybdenum Disulfide (CoMoS₂) Synthesized Using Alkyl-Containing Thiomolybdate Precursors. *Int. J. Hydrog. Energy* **2017**, *42* (32), 20669–20676. <https://doi.org/10.1016/j.ijhydene.2017.07.028>.
- (140) Agarwal, M. K.; Talele, L. T. Growth Conditions and Structural Characterization of Molybdenum Sulphoselenide Single Crystals: (MoS_xSe_{2-x}, 0 ≤ x ≤ 2). *Mater. Res. Bull.* **1985**, *20* (3), 329–336. [https://doi.org/10.1016/0025-5408\(85\)90191-6](https://doi.org/10.1016/0025-5408(85)90191-6).
- (141) Iranmahboob, J.; Hill, D. O.; Toghiani, H. Characterization of K₂CO₃/Co–MoS₂ Catalyst by XRD, XPS, SEM, and EDS. *Appl. Surf. Sci.* **2001**, *185* (1), 72–78. [https://doi.org/10.1016/S0169-4332\(01\)00653-5](https://doi.org/10.1016/S0169-4332(01)00653-5).
- (142) Mohanty, B.; Ghorbani-Asl, M.; Kretschmer, S.; Ghosh, A.; Guha, P.; Panda, S. K.; Jena, B.; Krasheninnikov, A. V.; Jena, B. K. MoS₂ Quantum Dots as Efficient Catalyst Materials for the Oxygen Evolution Reaction. *ACS Catal.* **2018**, *8* (3), 1683–1689. <https://doi.org/10.1021/acscatal.7b03180>.
- (143) Wu, J.; Liu, M.; Chatterjee, K.; Hackenberg, K. P.; Shen, J.; Zou, X.; Yan, Y.; Gu, J.; Yang, Y.; Lou, J.; Ajayan, P. M. Exfoliated 2D Transition Metal Disulfides for Enhanced Electrocatalysis of Oxygen Evolution Reaction in Acidic Medium. *Adv. Mater. Interfaces* **2016**, *3* (9), 1500669. <https://doi.org/10.1002/admi.201500669>.
- (144) Lu, X.; Zhao, C. Electrodeposition of Hierarchically Structured Three-Dimensional Nickel–Iron Electrodes for Efficient Oxygen Evolution at High Current Densities. *Nat. Commun.* **2015**, *6*, 6616. <https://doi.org/10.1038/ncomms7616>.
- (145) Ledendecker, M.; Clavel, G.; Antonietti, M.; Shalom, M. Highly Porous Materials as Tunable Electrocatalysts for the Hydrogen and Oxygen Evolution Reaction. *Adv. Funct. Mater.* **2015**, *25* (3), 393–399. <https://doi.org/10.1002/adfm.201402078>.
- (146) Trasatti, S.; Petrii, O. A. Real Surface Area Measurements in Electrochemistry. *Pure Appl. Chem.* **1991**, *63* (5), 711–734. <https://doi.org/10.1351/pac199163050711>.
- (147) McCrory, C. C. L.; Jung, S.; Peters, J. C.; Jaramillo, T. F. Benchmarking Heterogeneous Electrocatalysts for the Oxygen Evolution Reaction. *J. Am. Chem. Soc.* **2013**, *135* (45), 16977–16987. <https://doi.org/10.1021/ja407115p>.
- (148) Lu, Y.; Xu, H.; Wang, J.; Kong, X. Oxygen Reduction Mechanism on Copper in a 0.5M H₂SO₄. *Electrochimica Acta* **2009**, *54* (15), 3972–3978. <https://doi.org/10.1016/j.electacta.2009.02.019>.
- (149) Pickering, H. W. The Surface Roughening of a Cu–Au Alloy during Electrolytic Dissolution. *J. Electrochem. Soc.* **1968**, *115* (7), 690. <https://doi.org/10.1149/1.2411403>.
- (150) Iseki, S.; Ohashi, K.; Nagaura, S. Impedance of the Oxygen-Evolution Reaction on Noble Metal Electrodes. *Electrochimica Acta* **1972**, *17* (12), 2249–2265. [https://doi.org/10.1016/0013-4686\(72\)87016-6](https://doi.org/10.1016/0013-4686(72)87016-6).

Vita

Yulu Ge was born in Qiqihar, Heilongjiang, People's Republic of China. She received her BS in Pharmaceutical Engineering in 2012 from Heilongjiang University of Chinese Medicine and MS in Pharmaceutical Science in 2015 from Kunming University of Science and Technology. After working in Peking University as technician, she started the PhD program at the University of Texas at El Paso (UTEP) with Dr. Dino Villagran. During her PhD study, Yulu became focused on the design of electrocatalysts for sustainable hydrogen generation through water electrolysis, and soon she found the enthusiasm in physical inorganic chemistry by solving the difficulties in the research. Yulu has presented her work at multiple national and international conferences and is the author of several published research papers and book chapters. Throughout her PhD, she mentored undergraduate students who are interested in energy related chemistry for performing high quality experiments and encouraging them to pursue graduate degrees. During her last year in PhD program, she was selected to be a graduate research intern at las alamos national lab (LANL) and participated in energy related catalytical processes research for more applicable designs.

Contact Information: <yuluge377@gmail.com>